NTNU

Norwegian University of
Science and Technology

Landslide generated waves in dam reservoirs

Experimental investigation on a physical hydraulic model

Martina Gardoni

Lorenza Ponziani

Hydropower Development
Submission date: April 2017
Supervisor: Fjola Gudrun Sigtryggsdottir, IBM

Norwegian University of Science and Technology
Department of Civil and Environmental Engineering

NTNU
Norwegian University of
Science and Technology

Landslide generated impulse waves in dam reservoirs

Experimental investigation on a physical hydraulic model

Martina Gardoni

Lorenza Ponziani

Submission date: April 2017

Supervisor: Fjóla G. Sigtryggsdóttir

Co-supervisor: Francesco Ballio

Norwegian University of Science and Technology

Department of Hydraulic Environmental Engineering

NTNU
Norwegian University of
Science and Technology

Faculty of Engineering

Department of Civil and
Environmental Engineering

M.Sc. THESIS ASIGNMENT

Candidate: Martina Gardoni and Lorenza Ponziani

Title: Landslide generated impulse waves in dam reservoirs
Experimental investigation on a physical hydraulic model.

1 BACKGROUND

Landslide generated impulse waves may cause damages as they run-up shores, or against dams retaining a reservoir. Large such waves may overtop dams with hazardous consequences for the downstream area. The hazard may be intensified in the case of an embankment dam, considering that this may erode and even completely fail during such extreme loading conditions, thereby releasing more water from the reservoir. Additionally, dam overtopping due to landslide generated waves can also cause serious functional damage of concrete dams. A tragic such event occurred at the Vajont dam in Italy, where a landslide triggered a high impulse wave, resulting in a massive dam overtopping causing the destruction of the city of Langarone downstream and the death of more than 2000 people.

It was with this background that the Norwegian Water Resources and Energy Directorate (NVE) in collaboration with NTNU, initiated a study program on landslide generated waves and their effect on rockfill dams. For this purpose, an experimental work has been carried out on a physical model in the hydraulic laboratory at NTNU.

In 2014, the experimental tests were carried out for different landslide scenarios, by varying slide parameters. The physical processes and interaction between the landslide generated waves and dam overtopping was studied. A comparison was also made between, the results obtained from the experimental test, and results from a computational method recommended by Heller et al. (2009).

As a continuation of the project, an experimental study was conducted in 2015 and spring 2016, using the model in the hydraulic laboratory. The tests mainly focused on the slide volume and dam characteristics, and considered several different experimental scenarios by varying the parameters: of the slide volume, the reservoir water levels, and the upstream dam face slope and roughness.

The result from the physical model test in the spring 2016 was also compared with numerical methods developed by Norwegian Geotechnical Institute (NGI). This was to test if the

numerical tools are capable to model reasonably the experimental test from the laboratory. A numerical simulation was carried out based on an input data set from the experimental model in the lab. The result from simulation was compared with the physical model test results.

In general, the project study result have given better insight into the effect of the landslide generated waves and dam parameters. The study has also provided a better understanding on the characteristics of the slide generating waves and their impacts on dam overtopping. However, the studies have also recommended further investigations to verify results of the experimental test, as well as testing further the influence of slide velocity on rockfill dam overtopping. Additionally, it is of interest to investigate potential model effects in the current model.

2 MAIN QUESTIONS FOR THE THESIS

The thesis will be composed of a number of tasks related to assessing relevant literature and preparing and running an experimental study. The main objective is to use the scale model in the hydraulic laboratory at NTNU, in order to investigate the effect of landslide generated waves on embankment dams. This knowledge should contribute to the process of developing a method to estimate the volume of water overtopping an embankment dam as a result of landslide generated wave. Additionally, potential effects of the model setup (model effects) on the results will be investigated by moving the landslide ramp, so that the slide falls into the basin where it has a more regular form.

All experiments will be carried out using a fixed dam arrangement.

2.1 The specific tasks are detailed as follows

1. Review the current literature and find examples of previous studies on the impact of landslide generated waves on dams.

2. Study the existing model set-up and the installed instrument. Repeat the same test setup at least 10 times to get an idea of the variation in the measured results, identified by a statistical analysis of the data.

3. Carry out a model test on the existing model set-up to study the effect of the speed of the landslide on wave generation, propagation and dam overtopping. In these set-ups the wave will be generated using different slide geometry and volume. The slides will be released from different initial locations (resulting in different impact speed).

4. Modify the model set-up by relocating the ramp for the landslide. The main focus of the study will be on this new model set-up. The purpose of the relocation is to investigate potential model effects in the original model setup, as well as to investigate the effect of different landslide parameters and different freeboard. The experimental results will be compared to results from the original set-up, this includes consideration of different wave propagation. Additionally, the results from the new model set-up will be used to study the physical processes and the relationship between the different parameters, and the overtopping volume/wave height. As may apply, the impulse product parameters will be calculated aiming at identifying different relationships.

3 SUPERVISION, DATA AND INFORMATION INPUT

Associate Professor Fjóla Guðrún Sigtryggsdóttir, NTNU, is the supervisor of the thesis work. The candidates are exchange students from Politecnico, Milano, and Professor Francesco Ballio, Dipartimento di Ingegneria Civile e Ambientale, is their supervisor on behalf of the Politecnico, Milano. Additionally, Professor Jochen Aberle and Professor Leif Lia, both at NTNU, will be valuable discussion partners and advisors during the research work. Research scientist Kiflom Belete, NTNU, will provide advice on how to run the model.

Discussion with and input from colleagues and other research or engineering staff at NTNU, and Politecnico Milano are recommended. Significant inputs from others shall, however, be referenced in a convenient manner.

The research and engineering work carried out by the candidates in connection with this thesis shall remain within an educational context. The candidate and the supervisors are therefore free to introduce assumptions and limitations, which may be considered unrealistic or inappropriate in a contract research or a professional engineering context.

4 REPORT FORMAT AND REFERENCE STATEMENT

The report should be written with a text editing software, and figures, tables, photos etc. should be of good quality. The report should contain an executive summary, a table of content, a list of figures and tables, a list of references and information about other relevant sources. The report should be submitted electronically in B5-format .pdf-file in DAIM, and three paper copies should be handed in to the institute.

The executive summary should not exceed 450 words, and should be suitable for electronic reporting.

The Master's thesis should be submitted no later than **3. April 2017**

Trondheim, spring semester 2017

Fjóla G. Sigtryggsdóttir
Associate Professor

Abstract

The impulse waves generated by landslides that occur in an artificial basin may have disastrous impacts on the surrounding environment. For Alpine lakes, impulse waves are particularly significant, because of steep shores, narrow reservoirs geometry, possible large slide masses, and high impact velocities. Catastrophic events, as the well-known Vajont disaster occurred in Italy in 1963 which led to the loss of more than 2000 human lives, promoted the study of the physical process and the possible consequences of this phenomenon.

The present analysis is based on an experimental research performed on a 1:190 physical scale model in laboratory, which allows to simulate the entire phenomenon, from the landslide movement to the dam overtopping.

The main objective of this study is to gain more knowledge about the landslide generated impulse waves in reservoirs by trying to find a general modelling that, despite the phenomenon complexity, could help in the prediction of potential disaster effects. With this aim, experiments have been conducted by modifying the landslide location, the altitude of fall, its shape and volume, and by investigating two different dam freeboards. The research is initially focused on the simple observation of generated impulse waves amplitude and propagation in the basin, water height on the dam crest and total overtopping water volume. Subsequently, it proceeds with a dimensional analysis, based on the identified phenomenon governing parameters. In this way, we can demonstrate not only the influence of the slide volume and the basin water level on the total overtopping volume, but also the existing relation between the water outflow and the slide shape and velocity at the instant of impact with water.

Acknowledgments

We spent almost four months in Norway to develop this research. We would like to thank all the people who gave us the possibility to work on it, to work with them and upheld us along this beautiful, although sometimes difficult, experience.

We would like to express our deepest thanks to our Italian supervisor Prof. Francesco Ballio for giving us the opportunity to participate in this project, for taking care of us from Italy and for being so helpful when we came back. He always provided us with new incentives and ideas.

We are deeply grateful to our tutor in Norway Prof. Fjóla Gudrún Sigtryggsdóttir. The enthusiasm she conveyed on us and her persistent help were of fundamental importance in this research. We would like to express our thanks to her for giving us advices and for being our 'guide' in this adventure, suggesting great work lines. This master thesis would not have been possible without her support.

Our thanks and gratitude also goes to Prof. Jochen Aberle for letting us fulfil our desire of being students at NTNU and of taking part in such an interesting experimental work.

Special thanks to Prof. Leif Lia, to Research Scientist Kiflom Belete and to Eng. Geir Tesaker for his valuable assistance in the laboratory.

We are most grateful to our parents and families for their love and support and for having put us up for twenty-four years. The result achieved is dedicated to them.

We owe a special mention to Dino and Antonio for getting behind us, whatever the circumstances. Many thanks to all our special friends for being always by our side, even when the time devoted to them was not so much and many thanks to all the friends we will celebrate this important achievement with.

Lastly, thanks to Giorgio and Alfredo for never giving up even when we were not patient.

List of figures

List of tables

List of abbreviations

$\boldsymbol{a}$ Wave amplitude [m]
$\boldsymbol{a_M}$ Maximum wave amplitude [m]
$\boldsymbol{A}$ Flow area [m^2]
$\boldsymbol{A_m}$ Area in the scale model [m^2]
$\boldsymbol{A_p}$ Area in the prototype [m^2]
$\boldsymbol{A_r}$ Area scaling ratio [-]
$\boldsymbol{b_k}$ Dam crest width [m]
$\boldsymbol{b_S}$ Slide width [m]
$\boldsymbol{B}$ Flow cross-section top width [m]
$\boldsymbol{B_b}$ Basin width [m]
$\boldsymbol{B_i}$ Width of the i-dam top segment [m]
Ch. Channel
$\boldsymbol{d_g}$ Grain diameter [m]
$\boldsymbol{d_i}$ Instantaneous slide covered distance [m]
$\boldsymbol{D_g}$ Relative grain diameter [-]
$\boldsymbol{D_n}$ Kolmogorov-Smirnov's statistic
$\boldsymbol{E}$ Specific energy [m]
$\boldsymbol{E}$ Young's modulus [N/m^2]
$\boldsymbol{f}$ Freeboard [m]
$\boldsymbol{f_k}$ Height of the k-bar in the histogram
$\boldsymbol{F}$ Normal distribution function
$\boldsymbol{F_m}$ Force in the scale model [N]
$\boldsymbol{F_n}$ Empirical distribution function [N]
$\boldsymbol{F_p}$ Force in the prototype [N]
$\boldsymbol{F_r}$ Dynamic similarity [-]
$\boldsymbol{Fr_m}$ Froude number in the scale model [-]
$\boldsymbol{Fr_p}$ Froude number in the prototype [-]
$\boldsymbol{Fr_r}$ Froude similarity [-]
$\overline{\boldsymbol{F}}_{\mu}$ Viscous force [N]
$\overline{\boldsymbol{F}}_{\boldsymbol{e}}$ Elastic compression [N]
$\overline{\boldsymbol{F}}_{\boldsymbol{g}}$ Gravitational acceleration [N]
$\overline{\boldsymbol{F}}_{\boldsymbol{i}}$ Inertial acceleration [N]
$\overline{\boldsymbol{F}}_{\boldsymbol{pr}}$ Pressure force [N]
$\overline{\boldsymbol{F}}_{\boldsymbol{\sigma}}$ Surface tension [N]
$\boldsymbol{g}$ Gravity acceleration [m/s^2]
$\boldsymbol{g_m}$ Gravity acceleration in the scale model [m/s^2]
$\boldsymbol{g_p}$ Gravity acceleration in the prototype [m/s^2]
$\boldsymbol{h}$ Still water depth [m]
$\boldsymbol{H}$ Wave height [m]
$\boldsymbol{H_M}$ Maximum wave height [m]
$\frac{\boldsymbol{H}}{\boldsymbol{h}}$ Relative height [-]
$\frac{\boldsymbol{H}}{\boldsymbol{L}}$ Wave steepness [-]
$\boldsymbol{k}$ Critical depth [m]
$\boldsymbol{l_S}$ Slide length [m]
$\boldsymbol{L}$ Characteristic length [m]
$\boldsymbol{L}$ Wave length [m]
$\boldsymbol{L_b}$ Basin length [m]
$\boldsymbol{L_C}$ Slide chain length [m]
$\boldsymbol{L_m}$ Length in the scale model [m]
$\boldsymbol{L_p}$ Length in the prototype [m]
$\boldsymbol{L_r}$ Geometric similarity [-]
$\frac{\boldsymbol{l_S}}{\boldsymbol{b_S}}$ Slide shape ratio [-]
$\boldsymbol{m_s}$ Slide mass [kg]
$\boldsymbol{M}$ Relative slide mass [-]
$\boldsymbol{n}$ Bulk slide porosity [%]
$\boldsymbol{n_k}$ Number of measurements included in the k-class
$\boldsymbol{N}$ Sample size
$\boldsymbol{p}$ Pressure [N/m^2]
$\boldsymbol{P}$ Impulse product parameter by Heller and Hager [-]
$\boldsymbol{P}^*$ Dimensionless parameter [-]
$\boldsymbol{P_0}$ Slide starting position on the ramp [m]
$\boldsymbol{q_1}$ 25th percentiles
$\boldsymbol{q_3}$ 75th percentiles
$\boldsymbol{Q}$ Discharge for given flow area [m^3/s]
$\boldsymbol{Q_i}$ Istantaneous outgoing discharge from the i-dam top segment [m^3/s]
$\boldsymbol{Q_r}$ Discharge scaling ratio [-]

$\boldsymbol{R}$ Run-up height [m]
$\boldsymbol{s}$ Slide thickness [m]
$\boldsymbol{S}$ Relative slide thickness [-]
$\boldsymbol{t}$ Elapsed time [s]
$\boldsymbol{t_r}$ Time scaling ratio [-]
$\boldsymbol{T}$ Wave period [s]
$\boldsymbol{T_r}$ Relative time [-]
$\boldsymbol{v_i}$ Instantaneous slide velocity [m/s]
$\boldsymbol{V}$ Characteristic velocity [m/s]
$\boldsymbol{V_m}$ Velocity in the scale model [m/s]
$\boldsymbol{V_p}$ Velocity in the prototype [m/s]
$\boldsymbol{V_r}$ Kinematic similarity [-]
$\boldsymbol{V_s}$ Slide impact velocity [m/s]
$\boldsymbol{W_r}$ Volume scaling ratio [-]
$\boldsymbol{W_s}$ Bulk slide volume [m^3]
$\boldsymbol{W_w}$ Overtopping water volume [m^3]
$\boldsymbol{x}$ Distance from the point of slide impact [m]
$\boldsymbol{X}$ Relative streamwise distance [-]
$\boldsymbol{\alpha}$ Slide impact angle [°]
$\boldsymbol{\alpha}$ Significance level of the goodness-of-fit test
$\boldsymbol{\alpha_{limit}}$ Limit value of the significance level to accept the null hypothesis
$\boldsymbol{\beta}$ Run-up angle [°]
$\boldsymbol{\Delta a}$ Distance between the slide lower end and the basin water level [m]
$\boldsymbol{\Delta b}$ Distance between the slide centre of mass and the basin water level [m]
$\boldsymbol{\Delta t}$ Sample rate [s]
$\boldsymbol{\Delta x_k}$ Width of the k-bar in the histogram
μ Mean of the sample
μ Viscosity [kg/ms]
$\boldsymbol{\Pi_i}$ Dimensionless group
$\boldsymbol{\rho}$ Characteristic density [kg/m^3]
$\boldsymbol{\rho_s}$ Bulk slide density [kg/m^3]
$\boldsymbol{\rho_w}$ Water density [kg/m^3]
$\boldsymbol{\sigma}$ Compressibility [kg/ms^2]
$\boldsymbol{\sigma}$ Standard deviation of the sample
$\boldsymbol{\sigma}$ Surface tension [kg/s^2]
$\boldsymbol{\sigma_M}$ Standard error of the mean
$\boldsymbol{2D}$ Two-dimensional (in a wave channel)
$\boldsymbol{3D}$ Three-dimensional (in a wave basin)

I, II, III, IV ID codes for different slide starting positions on the ramp
1, 3, 4, 6 Slide blocks arrangements made up by one, three, four and six blocks respectively
2h, 2v Slide blocks arrangements made up by two blocks horizontally and vertically placed on the ramp respectively
A, B Subscripts indicating the model under consideration

Table of contents

1. Introduction

A landslide moving into reservoirs can generate impulse waves, which propagate in all available directions. When they reach shallow areas, shorelines or dams, their amplitudes become high having a shot at overtopping the dams. The potential damage as a result of overtopping water is more serious for embankment dams. They may be grievously damaged, eroded or they even completely fail. However, dam overtopping due to landslide generated waves can also cause detrimental damages to concrete dams impacting their functionality.

These impulse waves are particularly relevant for the Alpine environment where there is a considerable number of artificial reservoirs. There, steep valley sides, possible large slide masses and high impact velocities can generate catastrophic events.

1.1 The objectives of the research

Because governing parameters of these phenomena are not consistently predictable, passive methods are mainly available to prevent damages due to impulse waves: evacuation, water level drawdown in artificial reservoirs, freeboard control, or blasting of possible slides. For this reason, the water level of many artificial reservoirs is kept well below the maximum possible level. Consequently in more than 100 Italian artificial basins where landslide risk exists, the dam and the basin potentialities are underutilized. (*Panizzo and De Girolamo, 2005*).

Currently, methods for impulse wave characterisation and for predictions of consequential overtopping are limited due to governing parameters which are sometimes debatable in general model studies. The model data are not generally applicable and not based on independent parameter variations. Considerable scale effects usually affect the feasible hydraulic models. Further, the model tests are often insufficiently documented for numerical simulations.

With this background, the Norwegian water Resources and Energy Directorate (NVE) in collaboration with the Norwegian University of Science and Technology (NTNU, Trondheim) initiated a study program. For this purpose, since 2010 many experimental works have been carried out on a physical model in the Hydraulic laboratory at NTNU. The main objective of this research is to undertake additional investigations on the scale model in order to gain more knowledge about the impact of impulse waves, generated by subaerial landslides, on rockfill dam. Several trials (130 experiments) have been performed from October 2016 to December 2016 to study the effect of location and speed of the landslide movement on wave generation, propagation and rockfill dam overtopping. The wave has been generated using a different slide size/shape and a fixed dam arrangement; corresponding wave height, overtopping volume and overtopping height above the dam crest in the model have been monitored and studied. In the second part of the research, focused on a dimensional analysis, we tried to find a relation between slide and basin parameters and the overtopping water volume over the embankment dam. This will provide an a priori assessment of possible event properties. In detail, the influence of dam freeboard, slide volume, shape and impact velocity on the main outputs has been investigated. To support the obtained results, we performed an evaluation of uncertainties and repeatability of the gathered measurements, including the estimation of their standard errors.

1.2 Theoretical background

In order to fully understand the discussed phenomenon, it is considered important to provide some theoretical concepts about the process components. Referring to previous studies, this section focuses on characterization of wave types and landslides properties and causal factors. Some elements of dam safety are discussed with particular attention to differences between Italian and Norwegian safety regulations.

1.2.1 The landslide generated impulse waves

The generation of impulse waves caused by the impact of a landslide with water is a complex phenomenon that involves several physical aspects. The impulsive waves can travel for long distances, causing disasters far away from the generation area and

producing high wave run-up on shorelines. This can result in the case of artificial reservoirs overtopping of the dam.

The landslide generating the impulse wave can be activated in different ways. Referring to figure 2.1, three types of slides can occur: the subaerial slide, the partially submerged slide and the submerged slide. In the present study, the first case is the only investigated because it is the most hazardous case, regarding the moving mass that starts above the water level.

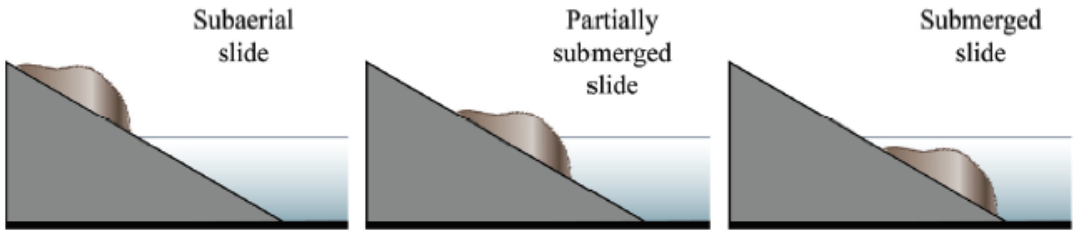

Figure 1.1: representation of the three different slide mass movements that can generate impulse waves (Heller et al., 2009).

Considering the subaerial slide, the generation of the wave and its propagation develop in distinct phases (*Panizzo and De Girolamo, 2005*). The landslide starts to move at first, achieving velocity along the slope until falling into the water, generating the wave (phase 1). After the impact with water the landslide body decelerates; the energy transfer from the slide to the water occurs mostly during the slide underwater movement (phase 2). The movement stops afterwards the landslide hits the basin bottom. Basing on what said it is possible to evaluate the elapsed time to underwater motion. Finally, water waves propagate in the reservoir in radially and longitudinally direction (phase 3) reaching shorelines or dam, where run-up phenomenon can occur (phase 4).

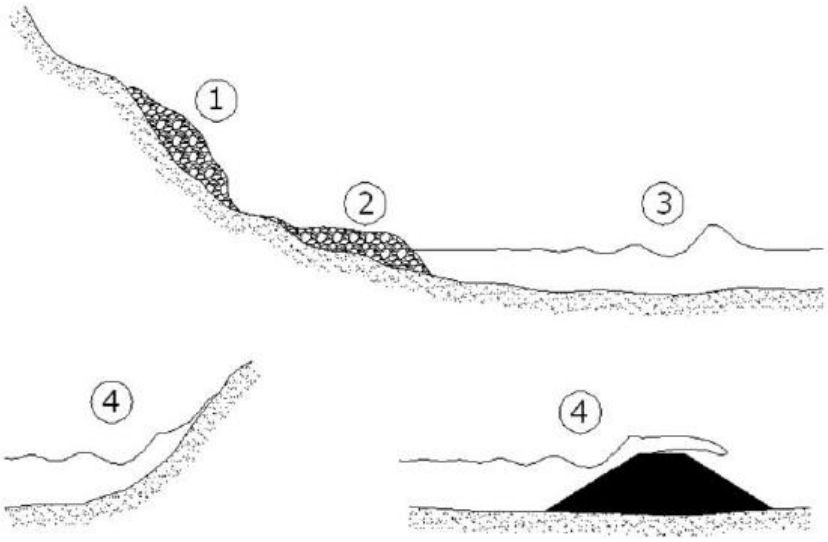

Figure 1.2: representation of the four different phases about impulse wave generation in an artificial reservoir, from the slide movement to the dam overtopping (Panizzo and De Girolamo, 2005).

From previous studies, it is known that the primary wave results from the momentum transfer between the impact of a slide mass and an initially quiescent water body. A substantial portion of the slide volume contributes to an instantaneous water displacement resulting in the generation of the leading wave crest within a fraction of the total slide impact duration (*Zweifel, 2006*). The crater phenomenon, caused by instantaneous flow separation, influences the wave propagation process due to the additional displacement of water during the slide impact. Moreover, the impact crater expansion prior to collapse depends on the period of crater formation, and thus on the slide impact duration. The crater duration is roughly proportional to the slide duration. Crater collapse generally involves mass air entrainment. The resulting three-phase mixture induces a turbulent, non-linear three-dimensional flow in the immediate area of the slide impact (*Fritz et al., 2003*).

A representation of the wave generation and the run-up phenomenon is provided in figures 1.3 and 1.4. Moreover, main parameters at stake are listed.

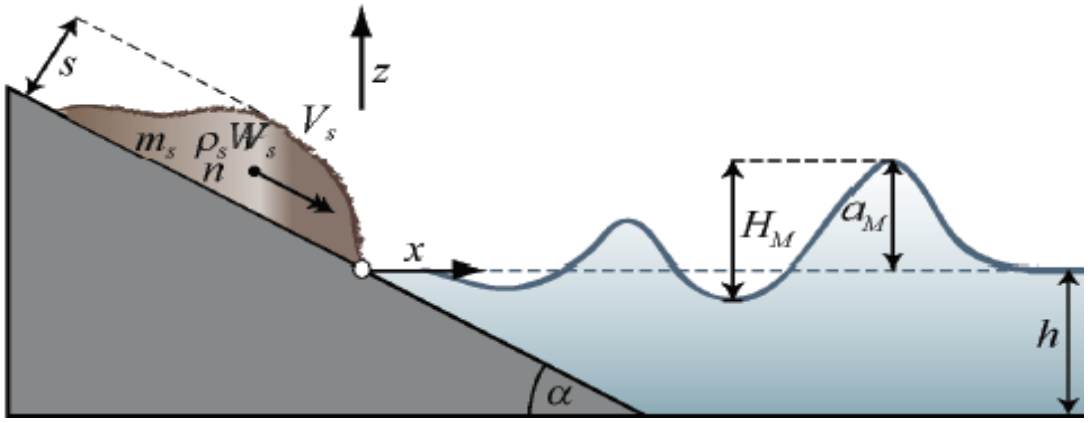

Figure 1.3: illustration of the impulse wave's generation caused by landslide (Heller et al., 2009).

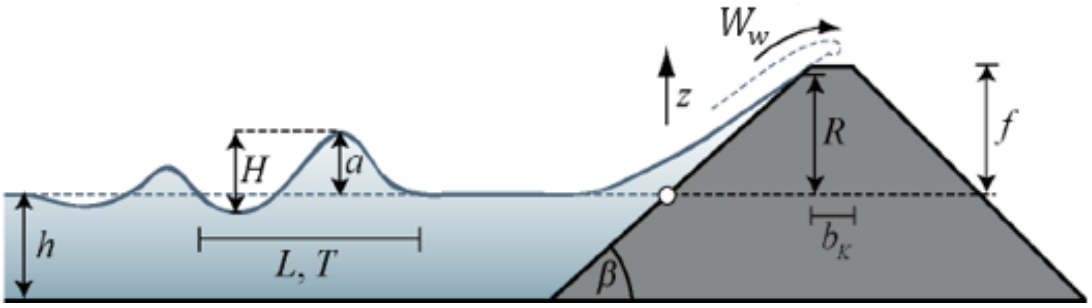

Figure 1.4: illustration of the impulse wave's propagation and run-up phenomena (Heller et al., 2009).

Slide impact velocity V_s

Bulk slide volume W_s

Slide thickness s

Bulk slide density ρ_s

Bulk slide porosity n

Slide impact angle α

Still water depth h

Slide mass $m_s = W_s \times \rho_s$

Maximum wave height H_M

Maximum wave amplitude a_M

Wave height H

Wave amplitude a

Wave length L

Wave period T

Run-up height R

Run-up angle β

Overtopping volume W_w

Freeboard f

Dam crest width b_k

The landslide generated impulse waves are included in the gravity wave category, as they are mainly influenced by gravitational force rather than capillarity. They differ from the perfect linear wave, which is consistent with the ideal sinusoidal wave characterized by a relative height (H/h) lower than 0.03 and by a wave steepness (H/L) lower than 0.006; more the wave deviates from the linear one, greater are these two

ratios (*Heller et al., 2009*). A further criterion that enables wave type description uses the ratio between amplitude and wave height (*a/H*), that is equal to 1 in case of the ideal perfect nonlinearity. Basing on that, three different nonlinearity levels are defined (*Zweifel et al., 2006*):

$$0.9 < a/H \leq 1.0 \text{ strongly nonlinearity}$$

$$0.6 < a/H \leq 0.9 \text{ moderately nonlinearity}$$

$$0.4 < a/H \leq 0.6 \text{ weakly nonlinearity}$$

Talking about impulse wave, four groups of non-linear waves can be discussed.

Stokes wave:

Stokes wave is steeper than a sine wave, and it is characterised by a trough flatter and longer than the peak. It is a deep or intermediate water wave ($L/h < 20$), therefore Stokes wave is only partly influenced by the reservoir bed: wave particles do not move in a closed orbit and, therefore, slight transport of fluid mass takes place. Usually, wind generated waves belong to this category (*Heller et al., 2009*).

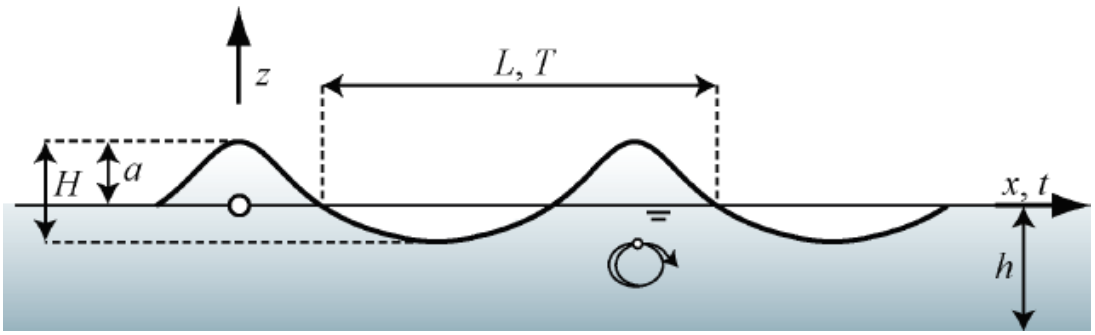

Figure 1.5: illustration of a Stokes wave, highlighting its main parameters (Heller et al., 2009).

Cnoidal wave:

The Cnoidal wave is periodic and it occurs in intermediate/shallow water ($L/h > 2$). It has mainly an oscillatory character but the orbital motion of water particle is not closed, involving fluid mass transport (*Heller et al., 2009*).

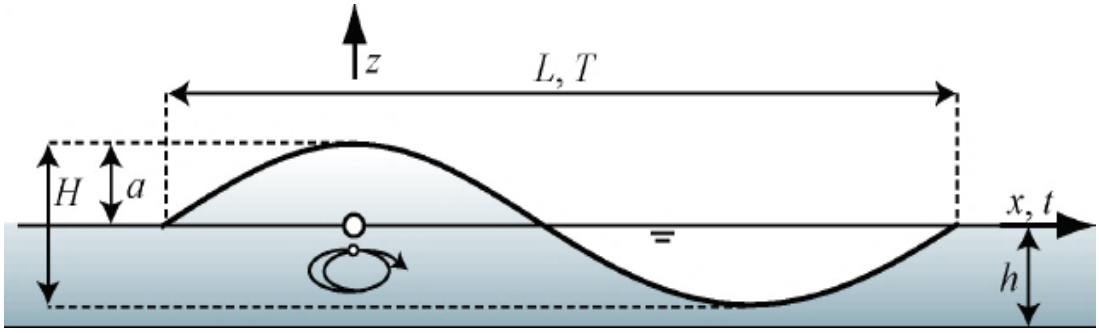

Figure 1.6: illustration of a Cnoidal wave, highlighting its main parameters (Heller et al., 2009).

Solitary wave:

Solitary wave is the most studied both by numerical simulations and by laboratory experiments. It is only characterized by a wave peak and there is no trough. Solitary waves develop in shallow water ($L/h > 20$) assuring a large horizontal fluid mass transport. This kind of wave has a wave amplitude equal to the wave height and its wave length tends to infinity. Tsunami caused by movements of tectonic plates is involved in this group (*Heller et al., 2009*).

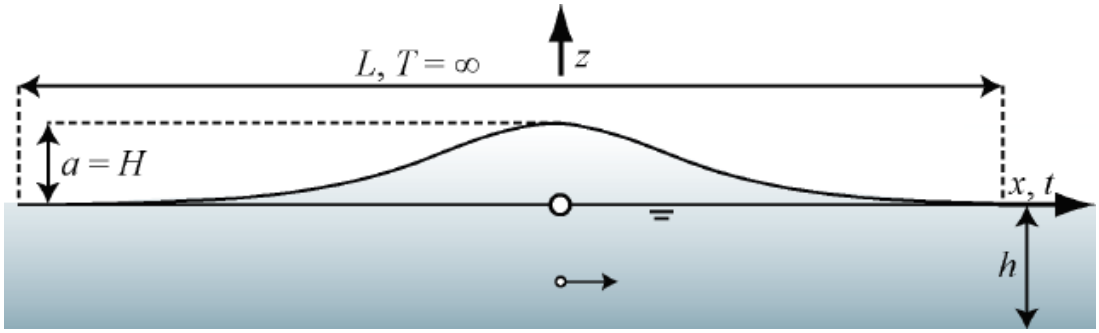

Figure 1.7: illustration of a Solitary wave, highlighting its main parameters (Heller et al., 2009).

Bore wave:

Bore wave is generated when air is entrained at the crest or when the top of the crest curls over. It is a shallow water wave ($L/h > 20$) in which particles move horizontally; Bore's profile has a steep front and a gently sloped back (*Heller et al., 2009*).

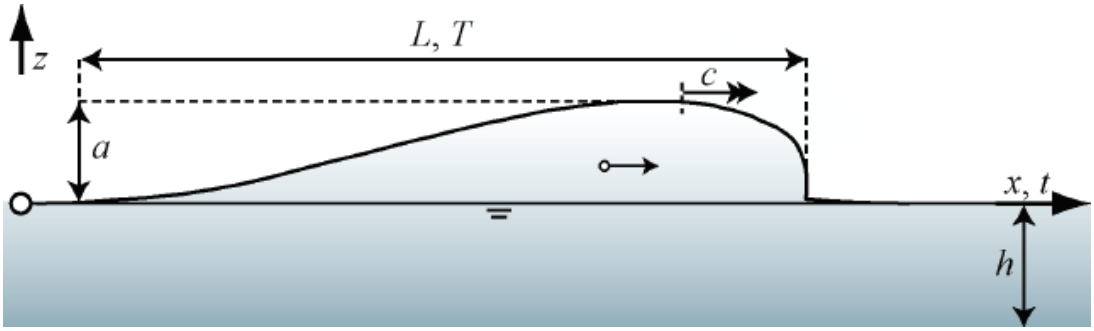

Figure 1.8: illustration of a Bore wave, highlighting its main parameters (Heller et al., 2009).

Different types of landslide generated impulse waves have been recognised in past studies (*Panizzo and De Girolamo., 2005*):

- leading wave with oscillatory wave characteristic;
- leading wave with solitary wave characteristics followed by a trough connecting it with the dispersive wave pattern;
- leading single wave with solitary wave characteristics, separated by the dispersive wave pattern;
- solitary wave with complex form.

When the dimension of the slide body is large in comparison to the water depth, solitary wave is to be expected. Instead, in deep water, a train of dispersive waves probably occurs.

The reservoir shape has a significant effect on the propagation of the impulse wave. The interaction between waves and the basin geometry can imply some alterations of the phenomenon (*Heller et al., 2009*):

- *refraction* occurs when a shallow water wave changes direction such that it moves mostly frontally towards the shore;
- *shoaling* can cause the height increase in shallow water wave and the wave length decrease;
- *diffraction* phenomenon consists in a loss of wave energy when the wave passes around an obstacle;
- *constriction* can be observed when a wave in a restricted area of the reservoir increases in height due to the concentration of wave energy (e.g. against a dam flank);

- *reflection* takes place when a wave, reaching the shore, is reflected and moves with reduced height back. The height of the reflected wave depends on how much of the energy is dissipated during the run-up;
- *interference* occurs when waves from different directions meet and interfere with one another. Wave interference can be *destructive* (two waves that cancel each other out, resulting in reduced or no wave), *constructive* (additive interference that results in waves larger than the original waves) or *rogue waves* (freak waves that occur due to interference and result in a wave crest higher than the theoretical maximum).

1.2.2 Landslide types

A landslide is the movement of rock, debris or earth down a slope, generated by one or more of several causes. The causal factors that result in slope failure can be divided into conditions and processes (*Popescu, 1996*). The term "conditions" indicates pre-existing long-term factors that induce the slope to become unstable. Examples of these are morphology and lithology of the area, hydrology of the soil and land use. Instead, the "triggering processes" are immediate actions that cause the slope movement. Intense rainfalls, rapid snowmelt, seismic shaking, volcanic eruption, coastal or stream erosion and filling of reservoirs may involve an immediate response in terms of landslide activity by increasing shear stresses or pore pressures and reducing the strength of slope materials.

In particular, sudden changes in surface level of water bodies in contact with adjacent slopes often reactivate dormant landslides or trigger shoreline failures. The sliding mass can move as a solid body or as a granular slide. If the slide impact velocity is low, the water height of the generated wave is considerably greater in case of solid bodies than in case of granular slides. In fact, if the slide material is granular, water can enter the pore volume whereas a solid body displaces all the water. Furthermore, the shape of a granular slide may change during impact (*Zweifel, 2004*).

Many classifications exist to distinguish and recognise different sliding phenomena. The classification herein proposed (*Cruden and Varnes, 1996*) is based on landslide kind of material, type of movement, causes, velocity, mass volume, state of activity

and other several factors. The mass movement types, which may occur on steep slopes generating waves in water bodies, are listed below.

- *Sliding* results from shear failure along one or several weak surfaces and it involves solid or granular bodies. If the slide plane is curved concavely upward, the movement will be rotational; instead, a surface rupture which is roughly planar entails a translational mass movement.
- *Flowing* involves plastic or predominantly fine-grained material, which becomes wet or dry flows. Wet flows commonly follow pre-existing drainage ways; they are of high density and may extend over long distances.
- *Falling* consists in an abrupt movement of rock or soil material that becomes detached from steep slopes. The movement occurs by free fall, bouncing and rolling and it is strongly influenced by gravity force and by the presence of interstitial water.
- *Toppling* takes place when a rock unit mass moves around a rotational point located below its gravity centre, under the actions of gravity and forces exerted by adjacent units and by fluid in cracks.
- *Complex landslide* is the combination of two or more of the above landslide's types.

A landslide is classified to be extremely slow if its velocity is lower than 16 mm/year. On the contrary, a velocity higher than 5 m/s typifies an extremely rapid sliding process.

Landslides can be categorized also basing on their mass volume: extremely small landslides have a volume lower than $5x10^2$ m^3, instead the biggest ones are characterized by a volume higher than 10^6 m^3.

Moreover, different states of activity of a landslide can be recognised: it may be active, inactive, suspended, re-activated, dormant, abandoned, stabilized or relict.

To assess the stability of slopes under existing conditions and the associated risk, a slope stability analysis needs to be performed. An understanding of geology, hydrology and soil properties is central to apply slope stability principles properly. Ground investigations include in-situ and laboratory tests, aerial photographs, study of geological maps and direct observation of the slope. This information, together with

numerical calculations and evaluation of various conditions effects, provide a method for preventing sliding phenomena.

1.2.3 Dam classification and associated hazard

Many cases of dam failure verified in past years. The highest failure rate is found in dams built between 1910 and 1920. In fact, less than the 0.5% of dams built since 1950 failed. The 70% of dam failures occurs in the first ten years of activity and more especially in the first year after commissioning, affecting mainly small dams (*ICOLD, 1995*). According to the International Commission on Large Dams, large dam is "a dam with a height of 15 meters or greater from lowest foundation to crest or a dam between 5 meters and 15 meters impounding more than 3million cubic meters, and defined in greater detail in the World Register of Dams" (*ICOLD, 2011*).

Dam failure mechanisms include:

- foundation problems as non-homogeneity and large settlement;
- overtopping caused by a non-functional structure or sliding of a body from steep slopes into the reservoir;
- internal erosion;
- cracks following settlements and causing piping;
- liquefaction.

Dams are usually classified in existing regulations according to several factors. The dam size (dimensions of the dam body, reservoir capacity and discharge capacity of the spillways) and type (dam shape and materials used during construction) provide indications about the flood wave that would be originated by the dam failure. The consequences of failure (human lives, properties and environment that could be affected by the flood wave) need to be evaluated basing on hazard classification, with the aim to estimate the risk of damage. The dam classification could also consider a combination of all those factors discussed above.

Criteria adopted for attributing grades to classification of dams are specific for each country. In general, all countries include the evaluation of downstream area of the valley affected by a possible generated flood wave, basing on simulations returned by dam-break flood models and on the calculation of factors related to the impacted valley, such as human occupation, land use and facilities. Through the risk analysis

methodology is possible to assess the probability of dam failure, starting from the evaluation of the main failure scenario.

Moreover, each country can have different approaches on dam emergency planning defining different responsibilities. However, it is a common practice having an emergency action plan (EAP) divided in five sections: detection, decision-making, notification to the local officials, warning to the population at risk and evacuation of the population at risk. The dam owner is responsible for the first three tasks, instead of warning and evacuation that are under civil defence authorities' responsibility. Emergency plans should be exercised periodically to ensure the preparedness of the organizations having responsibilities in emergency response. Hazard classification is appropriate not only to grade the level of safety control requirements but also to define the civil protection measures in managing emergencies (*ICOLD, 2012*).

Catastrophic failures of reservoirs and dams often result from series of hazards that occur sequentially. Dam design should include an environmental safety assessment for the entire reservoir area and immediate surrounding and for the river basin downstream the dam. An emergency warning system should be established cooperatively by the designer, the operator and the government agency.

In *Norway*, there are five dam consequence classes identified by a numerical scale from 0 to 4. Each class is associated to different dam failure consequences, evaluated in terms of the quantity of houses located downstream. Only classes from 1 to 4 implicate NVE (Norwegian Water Resources and Energy Directorate) regulations, because class 0 considers just the smallest dams which are characterized by a dam height lower than 2 m and a reservoir capacity smaller than 10^4 m^3. Classes 3 and 4 are also subject to regulations regarding the freeboard, which is required to be 4.5 m and 6 m respectively.

Table 1.1: main characteristics that define Norwegian dams consequence classes (Wright, 2015).

Consequence class	Hazard level	Housing units downstream
0	Minor	0
1	Low	1
2	Significant	1-20
3	High	21-150
4	Very high	150

The two Norwegian authorities responsible of emergency planning are the Ministry of Energy and Petroleum and the NVE. For all the dams in consequence class 4, 3 and 2, a dam break flood calculation is required as a basis for emergency action planning, including downstream evacuation plans made by local authorities. Regular inspections of the dam are conducted at different levels (according to consequence class) with trained personnel: periodic inspections every year, main inspections every 5-7 years and special inspections during and after unusual events (large floods etc.). In case of possible dam failure, the first warning is given by a Surveillance and Alarm system based on pneumatic sirens; further information is disseminated through television or radio broadcast.

Italy is one of those countries where dams are not subdivided into classes: only large dams, with a reservoir capacity higher than 10^6 m^3, are subject to regulations. The Italian authorities responsible for emergency planning are the Ministry of Infrastructures and Transport and the General Directorate for dams, water and electricity infrastructures. For the preparation of the EAP, flood propagation studies for all the large dams have been carried out by the dam owners, to determine the downstream areas affected by the possible flood generated wave. According to law, the staff of the owner must be present continuously on the dam site, living in a warden house located next to the dam. The owner must implement monitoring system of the dam, which is more or less complete for all dams. At each dam site, there is a siren that can be heard 1000 m downstream, to be activated before voluntary opening of the gates. Moreover, there are alert signs along the river, for 10 km downstream the dam, alerting about sudden floods due to water discharge from the dam.

1.3 Examples of historical events

Large water waves caused by slope failures on the margins of dam reservoirs, lakes, bays and oceans can result in flooding over the banks, run-up along the shoreline and overtopping dam crests. Historical landslide events with catastrophic consequences are readily available in literature with cases from all over the world.

In 1958, an 8.3 moment magnitude earthquake occurred in Lituya Bay, on the southern coast of Alaska. The event lasted from 1 to 4 minutes, causing a rock slide fall from a maximum altitude of 914 m above sea level on a slope averaging 40°. The impact of a mass with width dimensions from 730 m to 915 m, a maximum thickness of about 92 m and a centre of gravity at around 610 m elevation, generated a giant tsunami with a resulting maximum run-up of 524 m on a spur ridge on the southwest shore. The slide impact velocity was calculated equal to 92 m/s (*Slingerland and Voight, 1979*). Two people lost their lives and the run-up height was seven times larger than the highest run-up in Norwegian lake Loen event and roughly doubled wave run-up height in the Vajont reservoir in Italy.

Three tragic events occurred in Italy, at the Pontesei artificial reservoir (1959) and at the Vajont artificial reservoir (1960 and 1963). In Pontesei, a landslide with a front width and height of 400 m and 47 m respectively fell into the water without involving dam damaging. The slide covered a distance equal to 120 m in around 1 minute and the resulting run-up height was about 20 m, causing one casualty. However, the most catastrophic ever documented Italian phenomenon occurred in the Vajont valley, where the construction of the artificial reservoir amplified the instability of the slopes. In 1963, after the minor event of 1960, a subaerial landslide from Toc Mountain fell in the reservoir with an impact velocity of 20-25 m/s. The landslide mass was 2000 m wide and its front was 140 m high. The run-up height in correspondence of the dam was 235.5 m (*Semenza, 2002*) but the dam was not damaged. The huge overtopped wave destroyed the city of Longarone, located downstream, killing 2000 people.

Landslides are common in Norway due to the occurrence of valleys characterized by steep sides and adverse climate. Historical records (from the last 400 years) indicate that Norway has experienced about two to three catastrophic events every century. In the last one hundred years, three displacement wave events caused by the impact of rock sliding into the water occurred at Loen (1905 and 1936) and at Tafjord (1934), resulting in total 174 casualties. In these cases, the maximum run-up height ranged from 40.5 to 74.2 m (*Harbitz et al., 2014*).

Table 1.2: Some historical subaerial and partially submerged landslide generated impulse waves (Heller, 2007).

Year	Location	Material	W_s [$10^6 m^3$]	α [°]	h [m]	R [m]	Fatalities
1756	Tjelle (Norway)	Granite gneiss	15	>25	>200	46	38
1792	Shimbara (Japan)	Volcanic debris	500	10	64	10	>15000
1883	Krakatau (Indonesia)	Pyroxene/ basalt	-	-	-	35	36000
1888	Ritter Island (Papua New Guinea)	Basalt/ andesit	5000	10–15	1000	20	100
1905	Disenchantnent Bay (Alaska)	Glacier ice	29	28	80	35	0
1934	Tafjord (Norway)	Gneiss	2–3	60	>200	62	41
1936	Loen (Norway)	Gneiss	1	25	<60	74	73
1958	Lituya Bay (Alaska)	Schist	31	40	122	524	2
1959	Pontesei reservoir (Italy)	Silt/clay debris	5	5	47	20	1
1963	Vajont reservoir (Italy)	Limestone	240	0-40	50	235.5	200
1971	Yanahuin Lake (Peru)	Limestone	0.1	45	38	30	400-600
1980	Mount St. Helens (USA)	Rock	430	-	-	200	0

Figure 1.9: picture of Lituya Bay on the left and picture of Vajont valley on the right, both taken after the event.

2. State of the art

To expand the knowledge on landslide generated impulse waves in water bodies, many studies have been conducted in years. They have been mainly promoted in the 1960's, after disasters of major proportions. This chapter is an overview of earlier studies from literature and investigations performed on the same physical model of the present research.

2.1 Earlier studies

The past studies applied five different strategies: specific prototype studies (e.g., *Fritz and Liu., 2001 for Lituya Bay*), numerical simulations (e.g., *Falappi and Gallati, 2007*), predictions based on field data (e.g., *Ataie-Ashtiani and Malek Mohammadi, 2007*), analytical calculations (e.g., *Di Risio and Sammarco, 2008*), or general model studies (e.g., *Heller et al., 2009*).

Because of the unpredictable nature of the phenomenon, the exploration of landslide waves can best be conducted through laboratory experiments. Several analyses on both 2D and 3D general models have been promoted, studying waves propagation along a constricted channel or in a basin respectively. Further, the studies are either based on block or on granular slides.

General 2D studies, conducted on block slide physical models, focus on parameters study (*Walder et al. 2003*) and on dimensional analysis of the phenomenon (*Khamphuis and Bowering, 1970*). Additional 2D analyses on granular slide physical models concern parameters study (*e.g., Huber, 1980*) also by applying the PIV methodology (Particle Image Velocimetry; *Fritz et al. 2004*). Further analyses have been conducted to study scale effects (*Heller, 2007*) and to make a comparison between granular and block slide models (*Zweifel, 2004 and 2006*).

Moreover, 3D studies on granular slide models (*Huber, 1980)* and on block models (*Panizzo and De Girolamo, 2005*) have been carried out to perform additional parameters studies.

A complete computational method based on general model studies for reservoirs including the wave generation, propagation, run-up, dam overtopping, and the forces on dams have been conducted (*Heller et al., 2009*).

2.2 Previous investigations conducted on the model

Since 2014, many experimental studies have been carried out on the physical model in the NTNU hydraulic laboratory. General conclusions, about the phenomenon of landslide generated impulse waves in a reservoir, have been drawn.

Following Archimedes' Principle, it has been shown that landslides with a bigger volume falling into reservoir cause a greater amount of overtopping water; the relation between these two parameters is not linear. Also, the dam freeboard, that is inversely proportional to still water depth in the basin, strongly influences overtopping water volumes. In detail, in the experiments with a smaller freeboard, higher overtopping volumes are measured (*Bolzoni, 2015; Ramìrez, 2016; Mortensen, 2016*). Moreover, considering constant slide volumes but varying the freeboard and the dam slope, waves propagation in the basin has been proved to be always the same (*Ramìrez, 2016*).

The relationship between dam construction design and overtopping from landslide generated waves has been analysed; four dam types have been investigated (straight dam, rotated clockwise dam, rotated counter clockwise dam and Chevron dam). It has also been demonstrated that an increase in the dam roughness involves small differences in overtopping water volumes (*Mortensen, 2016)*.

A further study about the influence of slide particle size on the phenomenon has been conducted, confirming that higher values of slide density means bigger water outflows (*Lorås, 2014*).

The results from the physical model tests have been also compared to numerical methods developed by Norwegian Geotechnical Institute (NGI). A numerical simulation has been carried out based on an input data set from the experimental model in the laboratory to test if the numerical tools are capable to model reasonably well the

experimental tests (*Bolzoni, 2015*). The result from simulation has been compared to the physical model test result.

3. The physical model

In order to well interpret results returned by performed trials, this paper section wants to describe thoroughly physical models structure and instruments used. Chapter 3 represents a general framework about input model variables, that condition the phenomenon analysed, and resulting outputs. Given that tests have been carried out on two different physical models, a specific paragraph is devoted to explain their particularities. Subsequently, instruments calibration procedure is discussed in detail since it is essential to obtain interpretable results.

Experiments have been conducted on a physical model in the hydraulic laboratory (Norsk Hydroteknisk Laboratorium) at NTNU University of Trondheim, in Norway. The model was built in 2010 as a reproduction of Geirangerfjord in Western Norway for studying the flood risk caused by the possible Åkneset rockslide. In the following years, the model has been rebuilt many times and a dam has been placed at one of its end with the aim to understand better the impact of landslide generated waves on rockfill dams. For this reason, the model cannot be linked with an existing case, however, a scale of 1:190 has been applied as well to implement some technical procedures and analysis.

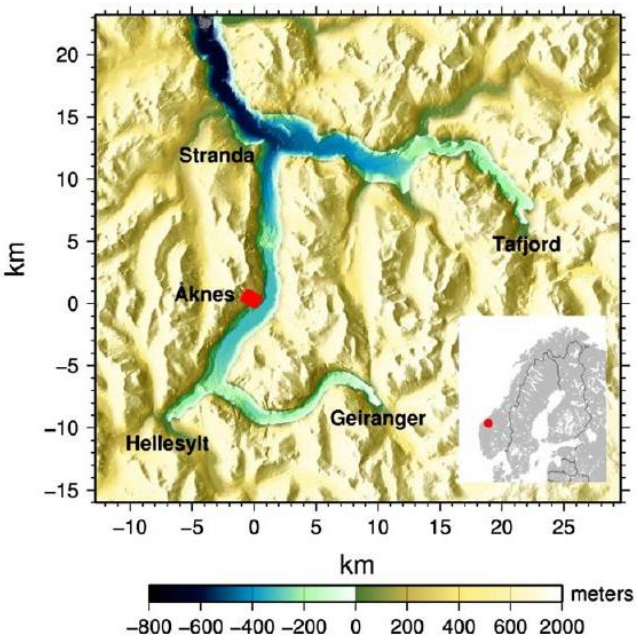

Figure 3.1: map of Åkneset site and surroundings.

3.1 Model description

The model simulates a landslide fall in the reservoir, where an impulse wave is generated and propagates towards the dam. The model main structural components are: a basin, a ramp placed upstream on a reservoir side and a Chevron dam located downstream.

3.1.1 The basin

The basin has a trapezoidal shape of 4.50 x 2.97 x 0.76 m. In the majority of experiments, the water volume contained in this part of the reservoir is about 2.5 m^3. The basin sides are covered with a concrete paste for increasing the roughness and making the phenomenon more realistic.

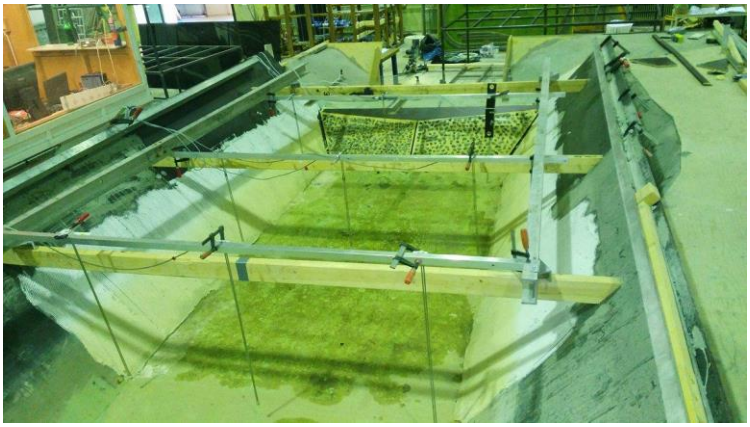

Figure 3.2: picture of the trapezoidal basin with sensors inside and the dam on background.

3.1.2 The slide

The slide is made up of rigid blocks set on a sloping ramp. A block model has been chosen in place of a granular one, basing on what geological surveys in Geirangerfjords have revealed about the nature of deposits related to previous incidents in the site. Six different blocks are available and they can be joined with appropriate rings. The distance between two rows of blocks is approximately 7-8 cm extended, in such a way that the slide could bend at the connections.

Figure 3.3: picture of the slide ramp placed on a basin side.

This gap is assumed to have only minor effects on the generated waves. In each blocks arrangement, the landslide has a 45° sloped front, to push the water out and to simulate a slide that has a smaller front and a larger body *(Sælevik et al., 2009).*

Rigid blocks can have different shape and size as illustrated in figure 3.4; their properties are listed in table 3.1. Each block has a volume equal to almost 1.5 % of water volume contained in the trapezoidal basin.

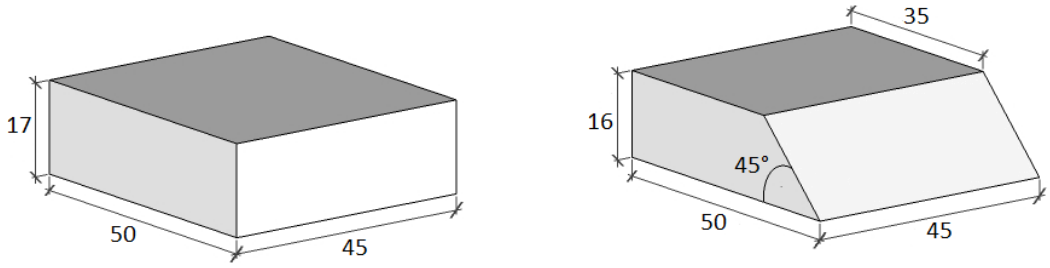

Figure 3.4: rigid blocks scheme with geometrical measurements in cm; rectangular parallelepiped on the left and right trapezoidal solid on the right.

Table 3.1: rigid blocks properties.

Block number	Weight [kg]	Volume_model [m^3]	Volume_prototype [m^3]	Shape
1	42.3	$3.83x10^{-2}$	$2.63x10^{5}$	Rectangular parallelepiped
2	42.4	$3.83x10^{-2}$	$2.63x10^{5}$	Rectangular parallelepiped
3	42.3	$3.83x10^{-2}$	$2.63x10^{5}$	Rectangular parallelepiped
4	42.4	$3.83x10^{-2}$	$2.63x10^{5}$	Rectangular parallelepiped
7	37.7	$3.06x10^{-2}$	$2.10x10^{5}$	Right trapezoid solid
8	37.6	$3.06x10^{-2}$	$2.10x10^{5}$	Right trapezoid solid

3.1.3 The dam

The type of dam used in the present study case is “Chevron”. It is one of the most popular geometrical dam design in Norway; previous analysis performed on the physical model compared different kinds of dam geometry (*Mortensen, 2016*).

The dam is composed by two identical and symmetrical wooden faces, with stones 16-35 mm glued on to simulate roughness and a dam slope of 1:1.5. The structure top,

which should be flat, is a bit sloped, therefore the dam height measured at the ends differs by 1.7 cm from the one measured at the centre.

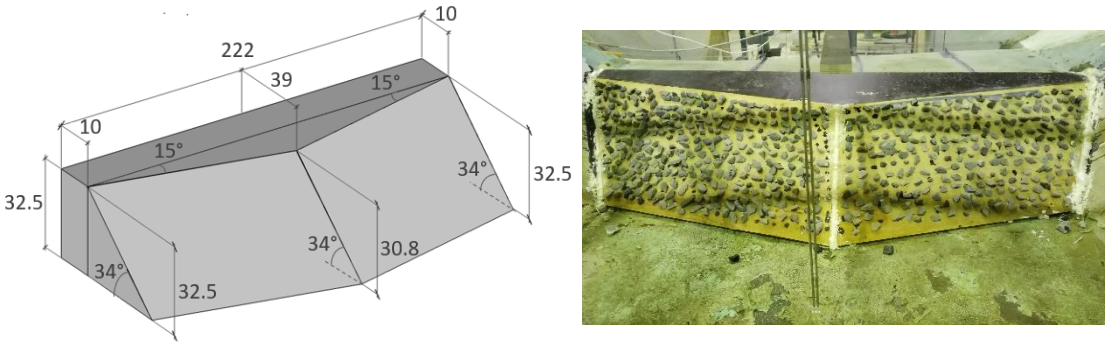

Figure 3.5: dam scheme with geometrical measurements in cm on the left and dam picture on the right.

Water that overtops the hydraulic structure crosses a concrete flat surface prior to be funnelled into a plexiglas channel; both the concrete surface and the channel are subdivided in four different sectors, through duct tape and thin plexiglas plates respectively (figure 3.6). To permit a good evaluation of the overtopped volume, the water is guided from each channel segment to the corresponding bucket, via pipes with 10 cm diameter. Only water that arrives in the fourth channel segment may be collected in two different buckets: one tube comes out from the channel bottom, the other one is placed on the lateral side in a higher position. The five collecting buckets have the same size: 68.5 x 46.5 x 31.5 cm.

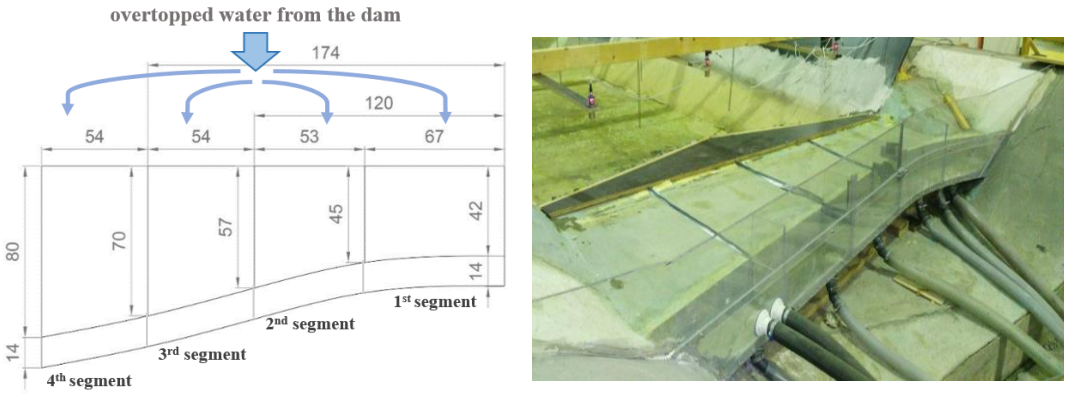

Figure 3.6: scheme and picture of the model part that is crossed by the water during overtopping, before reaching the plexiglas channel; geometrical measures are in cm.

Figure 3.7: picture of the five collecting buckets connected to the plexiglas channel through pipes.

3.2 Model rebuilding

The available model used for the first part of experiments was suspected to be affected by some laboratory effects. For this reason, the first model has been rebuilt, by raising the bottom in slide impact zone in order to obtain the same water depth in the whole basin.

During the reconstruction, ramp location and slope were modified for analysing their influence on impulse wave generation and propagation.

Instead, the part of the model upstream was not subjected to any modification.

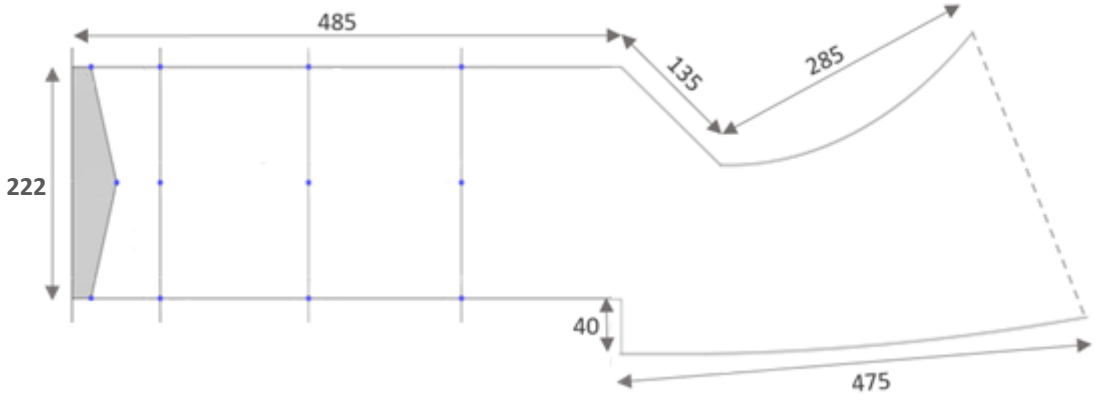

Figure 3.8: scheme of the entire model with geometrical measurements in cm.

3.2.1 Model A

The initial model, named Model A, presents a slide located on the left side of the reservoir, considering the wave propagation direction. The ramp slope is 40° and the

structure is almost 5 m far from the dam. This arrangement results in an impulse generated wave that propagates not only downstream, in the basin, but also in the part of the reservoir upstream. Hence, a lot of minor reflected waves overlap the incident wave, disturbing its propagation record.

In the slide impact zone, the reservoir is 24 cm deeper than in the basin. This laboratory effect also influences the wave propagation.

Nine sensors are in the reservoir for measuring the height of landslide generated waves. Each detector is partially submerged and corresponds to a channel with an identification number from 1 to 9 which returns voltage values. They are regularly spaced out on three different parallel steel bars, in order to obtain measurements at various distances from the dam. This grid of sensors permits a good estimation of waves path in the basin.

In order to evaluate the run up wave height, there are three detectors connected to channels from 12 to 14. They are placed above the Chevron dam crest following its shape to describe better the overtopping process.

Channel 10 returns an evaluation of slide covered distance, instead, channel 11 is not taken into consideration because it is not connected to any instrument.

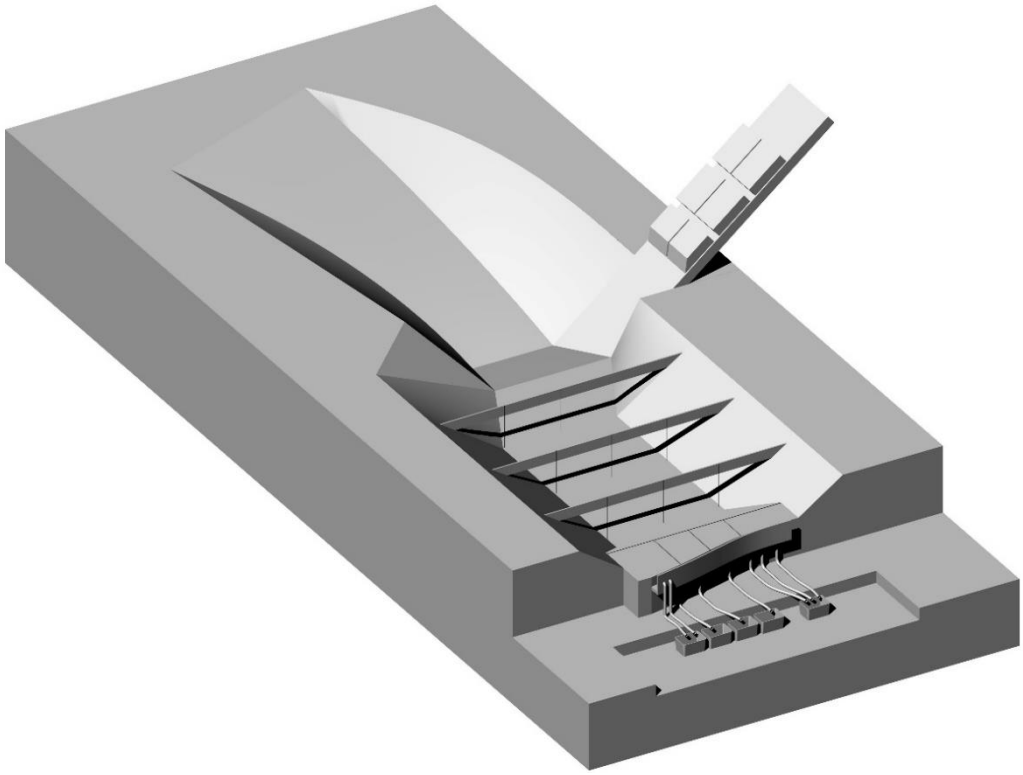

Figure 3.9: 3D scaled representation of Model A.

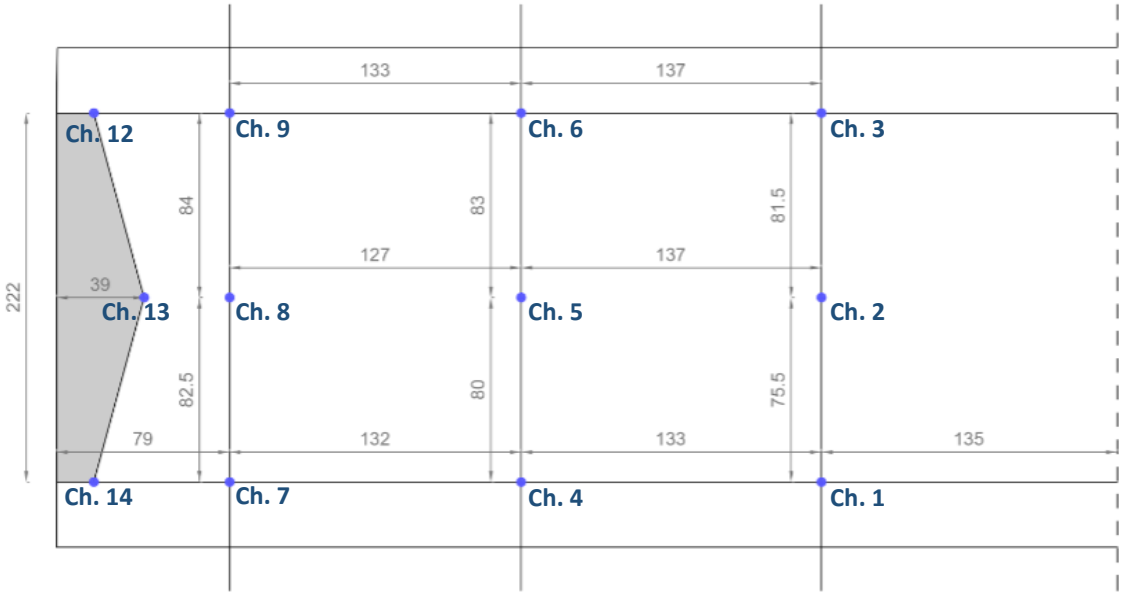

Figure 3.10: sensors grid scheme in Model A, where blue dots correspond to sensors; geometrical measurements are in cm.

3.2.2 Model B

During model rebuilding, the ramp has been moved on the right side of the basin, in a location opposite to the previous one. In the second model, named Model B, the ramp slope is 50° and it aligns with the basin side slopes. The distance between the slide and the dam, being about 3 m, is shorter than in the previous model. In this way, the wave reflection effect due to the model upstream part is attenuated.

Furthermore, to remedy previous model defects, the basin bottom has been raised by 24 cm in the slide impact zone.

Because of the new slide location, the first line of sensors (channels 1-3) has been moved in a direction towards the dam to prevent damage to instruments from falling blocks.

The remaining wave height sensors (channels 4-9) and run up sensors (channels 12-14) have not been moved, and are in the same location as in Model A.

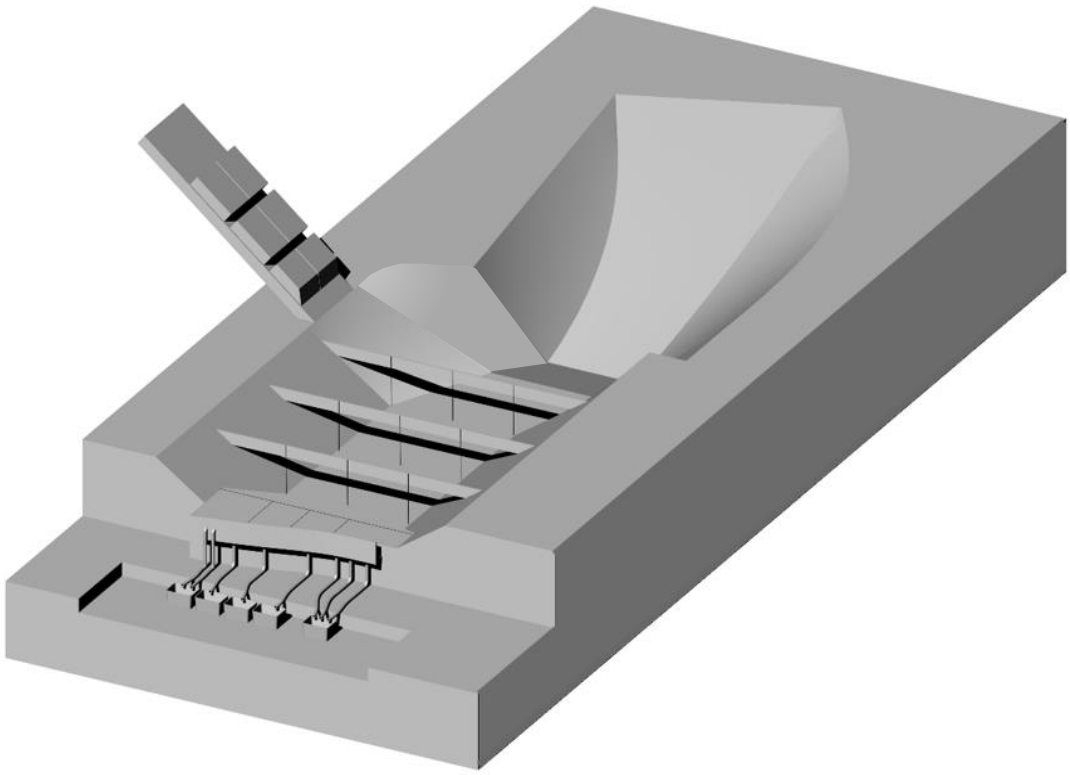

Figure 3.11: 3D scaled representation of Model B.

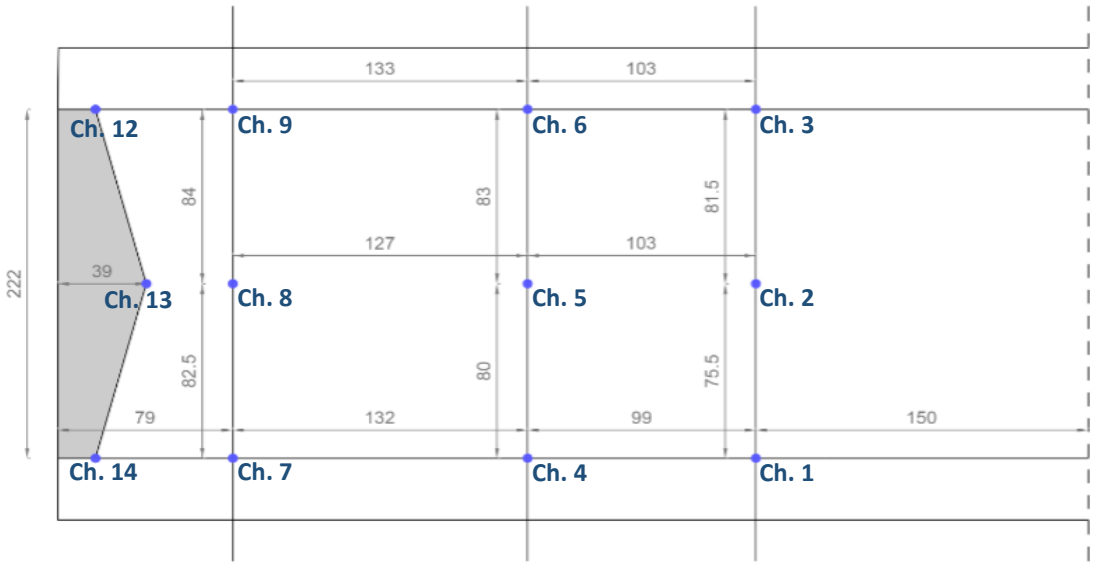

Figure 3.12: sensors grid scheme in Model B, where sensors correspond to blue dots and geometrical measurements are in cm.

Differences between the two models are summarized in table 3.2.

Table 3.2: structural properties of Model A and Model B.

	Slide location	Ramp slope [°]	Ramp length ** [cm]	Slide-dam distance [m]	Impact zone-basin bottom gap [cm]
Model A	Right side	40	348	5	24
Model B	Left side	50*	365	3	0

** aligns with basin side slope*
*** evaluated from the slide higher end to the basin bottom*

3.3 Froude's model law

A physical model is a miniature reproduction of a physical system, useful in finding solutions to hydraulic engineering problems through direct simulations in laboratory. Being a continuous representation of the prototype, it covers the gap between numerical models and reality.
In a physical model, the flow conditions are said to be close to those in the prototype if the model displays similarities shown in table 3.3.

Table 3.3: list of similarity types.

Similarity type	Symbol	Ratio
Similarity of form (geometric similarity)	L_r	$\frac{L_m}{L_p}$
Similarity of motion (kinematic similarity)	V_r	$\frac{V_m}{V_p}$
Similarity of forces (dynamic similarity)	F_r	$\frac{F_m}{F_p}$

Where subscript *p* means prototype (full scale) parameters, *m* means model parameters and *r* is the ratio of model to prototype quantity.

To achieve the perfect dynamic similarity, it is necessary that:

$$\frac{\bar{F}_{i_m}}{\bar{F}_{i_p}} = \frac{\bar{F}_{g_m}}{\bar{F}_{g_p}} = \frac{\bar{F}_{\mu_m}}{\bar{F}_{\mu_p}} = \frac{\bar{F}_{\sigma_m}}{\bar{F}_{\sigma_p}} = \frac{\bar{F}_{e_m}}{\bar{F}_{e_p}} = \frac{\bar{F}_{pr_m}}{\bar{F}_{pr_p}} \qquad \textit{Equation 3. 1}$$

Where forces are defined in the table 3.4:

Table 3.4: list of forces involved in equation 3.1.

Symbol	Force	Formula	Unit
$\overline{\boldsymbol{F}}_{\boldsymbol{i}}$	inertial force	$\rho L^2 V^2$	Newton [N]
$\overline{\boldsymbol{F}}_{\boldsymbol{g}}$	gravitational acceleration	$\rho L^3 g$	Newton [N]
$\overline{\boldsymbol{F}}_{\mu}$	viscous force	$\mu V/L$	Newton [N]
$\overline{\boldsymbol{F}}_{\boldsymbol{\sigma}}$	surface tension	σL	Newton [N]
$\overline{\boldsymbol{F}}_{\boldsymbol{e}}$	elastic compression	EL^2	Newton [N]
$\overline{\boldsymbol{F}}_{\boldsymbol{pr}}$	pressure force	pL^2	Newton [N]

Given that the achievement of perfect dynamic similarity is impossible, it is necessary to consider only the most important ratio, neglecting the other ones. In free-surface flow problems, inertial and gravity forces are dominant. For this reason, in this study case *Froude scale modelling* is adopted:

$$Fr_r = \frac{Fr_m}{Fr_p} = 1 \qquad \textit{Equation 3.2}$$

If the gravity acceleration is the same in both the model and prototype, the equation 3.2 implies:

$$V_r = \frac{V_m}{V_p} = \sqrt{\frac{g_m L_m}{g_p L_p}} = \sqrt{L_r} \qquad \textit{Equation 3.3}$$

Other important relations derived from equation 3.2 are:

$$A_r = \frac{{L_m}^2}{{L_p}^2} = {L_r}^2 \qquad \textit{Equation 3.4}$$

$$W_r = \frac{{L_m}^3}{{L_p}^3} = {L_r}^3 \qquad \textit{Equation 3.5}$$

$$Q_r = \frac{V_m A_m}{V_p A_p} = A_r V_r = {L_r}^2 \sqrt{L_r} = {L_r}^{2.5} \qquad \textit{Equation 3.6}$$

$$t_r = \frac{L_m V_m}{L_p V_p} = \frac{L_r}{\sqrt{L_r}} = \sqrt{L_r} \qquad \textit{Equation 3.7}$$

Thanks to Froude's model law it is possible to scale model outputs in the reality, even if scale effects always occur because of non-identical force ratios, involving a deviation between scaled model and prototype. Laboratory effects may also influence results due to mistakes in model design.

3.4 Model parameters

The main goal of this study is to analyse the features of impulse waves as functions of landslide and basin main parameters. Additionally, to study the effect of this on the volume of water overtopping a dam. Model structure allows to act on four parameters that affect trial results: still water depth in the basin and volume, shape and starting position of the slide.

A piezometer has been placed next to the basin with a level indicator inside, in order to achieve the exact water depth wanted. Water filling and draining are enabled by a pumps system. The freeboard is one of the main parameters and consists in the vertical distance from the dam crest to the still water level in the basin.

Figure 3.13: water level indicator on the left and piezometer on the right.

Slide volume, shape and velocity may be changed by adding and removing rigid blocks and by varying their initial location on the ramp. The six blocks available can be arranged in rows made by one or two blocks in order to obtain a slide more extended in length or in width. Blocks placed at the top of the slide are joined to the upper part of the ramp with a chain of variable length and a hook.

These parameters affect directly model outputs: slide velocity (channel 10), wave height in the basin (channels 1-9), run-up height on the dam (channels 12-14), and overtopping volume.

3.5 Instruments description and calibration

Sensors measurements are electrically sent by cables to the software "Agilent Measurement Manager", that gives *.csv* files as outputs. The sampling rate of

measurement is $\frac{200\ samples}{1\ sec}$; it permits a dense data set and a good description of waves propagation and overtopping event.

3.5.1 Wave gauge sensors

The nine wave gauge sensors, hung from the steel bars, are necessary to measure the wave height. The sensor type is "DHI wave-meter 102E"; it is composed by two parallel electrodes almost 80 cm long which work basing on the electrical conductivity principle in a fluid. The nine sensors need to be calibrated before each test, every time that the water level in the basin changes, in order to obtain more accurate results.

The calibration procedure develops in different steps:

- when the water surface is flat, the zero level could be fixed by setting each channel at 0 V even if it is impossible reaching this value in a stable way because of errors which affect the instruments;
- then, it is necessary to elevate the steel bars of 50 mm and then to fix -1 V. The same process is applied lowering the sensors of 50 mm and setting the voltage at +1 V. In this way, it is possible to simulate a decrease/increase of water level;
- when the calibration process is over, the steel bars are located again at the initial position (zero level) to start the test.

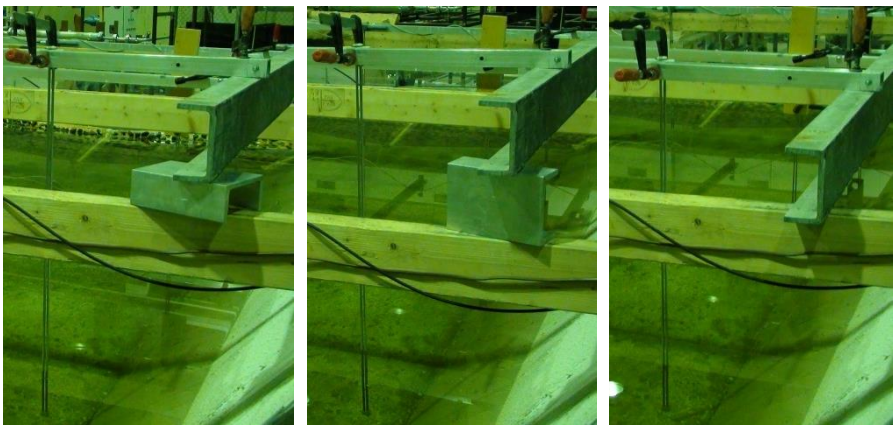

Figure 3.14: calibration procedure steps for channels 1-9.

Through this procedure the calibration factor is obtained ($\frac{50\ mm}{1\ V}$), allowing the output data conversion from voltage to water wave height.

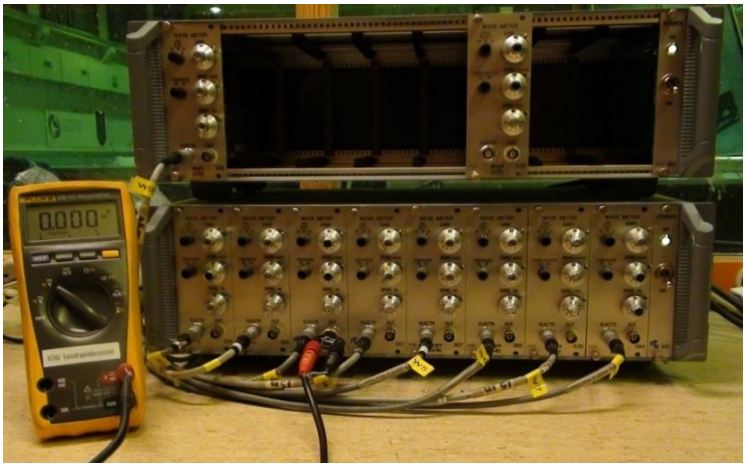

Figure 3.15: wave channels 1-9 and voltmeter beside.

3.5.2 Ultrasonic sensors

Three sensors, placed above the dam crest, allow the run-up measurement that represents the height of water which crosses the structure. These are ultrasonic detectors, which emit a high-frequency sound pulse: considering the time taken by this signal to be reflected back, they evaluate a voltage measurement. Instruments have been calibrated by moving a block of 50 mm height below the sensor itself.

Figure 3.16: ultrasonic sensors above the dam crest during an overtopping event (Mortensen, 2016).

The voltage difference between the measurements with and without the block below the sensor allows the calibration factor calculation. This procedure has been applied many times, obtaining an average value of $\frac{50\ mm}{2.4\ V}$ at the end.

A fourth sensor of the same kind is used to find out the overtopping volume from the dam, which is collected in five different buckets. The instrument needs to be moved

manually from one bucket to another and measurements are not automatically transmitted to the software. This ultrasonic sensor returns data in millimetres, which need to be converted in volumes. After many trials conducted, a calibration factor of $\frac{1\ dm^3}{5.6\ mm}$ has been settled (see Appendix A "Calibration procedure applied to obtain overtopping volume measurement").

In case of very small overtopping volumes, results are strongly affected by errors due to the irregular shape of buckets bottom, which causes a non-uniform water layer in the pails. To avoid this phenomenon, 1 l of water was poured into each bucket before each experiment.

Figure 3.17: ultrasonic sensor used for the evaluation of overtopping volume collected in the buckets.

3.5.3 Rotational sensor and speedometer

A rotational sensor is located above the slide mass and connected to the rigid blocks through a hook. It is composed by a rope, which unrolls together with the slide mass allowing the knowledge of distance covered by the slide and, as a consequence, its velocity. Before starting the experiment, it is important to be sure that the speedometer triggering wheel, placed on a side of the ramp, is attached to the first rigid block; in this way Agilent software starts to record at the same moment in which the sliding process begins.

The rotational sensor needs to be calibrated to establish a correlation between voltage given by the instrument itself and covered distance. By pulling out the rope 50 cm many times and by reading with a voltmeter the corresponding difference in Volt, a calibration factor of $\frac{0.5\ m}{0.67\ V}$ is obtained.

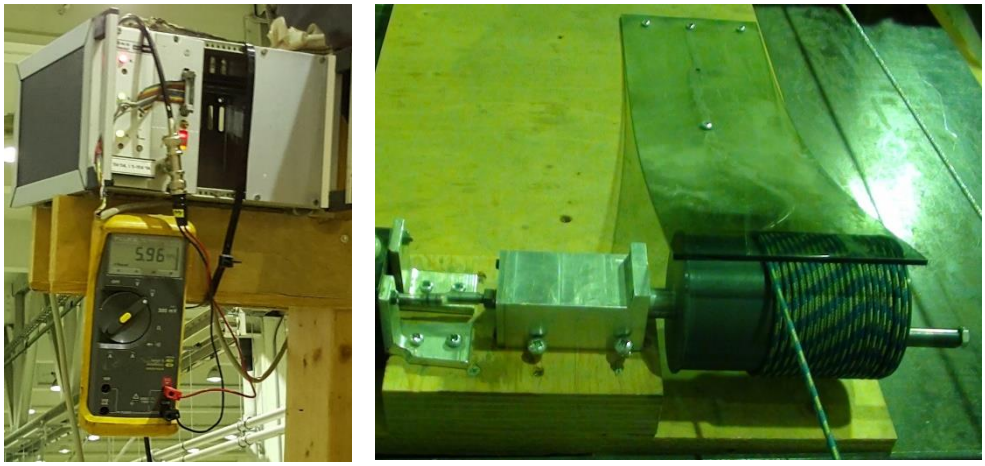

Figure 3.18: voltmeter on the left and rotational sensor on the right.

4. Procedure and tests

Chapter 4 describes all the phases that compose the experimental procedure, clarifying their duration and the main operations involved. The operative steps are reiterated in the same way for all tests. Trials setup is provided, including an identifying classification that is adopted throughout the paper. Calibrated data processing and filtering procedures are discussed.

4.1 Experimental procedure

Each test is carried out following a standard procedure, composed of three main operative steps.

4.1.1 Preliminary phase

The basin is filled through a pump and the water level is monitored using the piezometer, to reach the wanted freeboard. The calibration of channels from 1 to 9 can be done only when the water table is completely flat. Meanwhile, the slide is arranged by placing rigid blocks at the chosen starting position on the ramp. Before the slide release it is necessary that the triggering wheel, located on the ramp lateral side, is in contact with the blocks and the rope of the rotational sensor has to be stretched. Moreover, each bucket need to be refilled with 1 l of water using a graduated cylinder. The preliminary phase is the most important one because its accuracy acts directly on results. This step takes approximately 20 minutes.

4.1.2 Test execution phase

Test execution phase starts with the activation of two digital cameras emplaced so that landslide fall and dam overtopping could be filmed. Then, Agilent software is switched on and, as soon as the slide starts moving, it begins collecting data from channels 1 to

14. Slide release occurs manually through a simple rope system, by unhooking the chain which keeps slide mass at the initial position on the ramp.

Each record time length is set between 45 and 60 seconds because this period is long enough to study properly the phenomenon: after this time, waves are low and overtopping does not occur again.

4.1.3 Data gathering phase

Obtained raw data need to be downloaded from the software and transferred in an Excel file. Overtopping water heights, read moving the ultrasonic sensor manually on each bucket, are transcribed in the same Excel file, in addition to results automatically returned by channels from 1 to 14. Later, all these data need to be processed applying the correspondent calibration factor.

At the end, blocks fallen in the basin are lifted and replaced on the ramp and buckets are emptied. This step takes approximately 30 minutes.

Concluded the third operative step, it is possible to restart the same procedure for the next trial.

4.2 Tests description

The experimental part of this study lasted from 10th October to 15th December 2016. Tests made until 7th November were executed on Model A; instead, after the rebuilding, from 14th November, trials were conducted on Model B. Altogether, 130 experiments have been carried out.

First of all, a statistical analysis is performed, considering 26 tests with the same setup in terms of slide and basin properties. The aim of this evaluation is verifying the repeatability of instruments results.

Then, on both models, the impulse waves generated by landslide are investigated, after changing the blocks starting position (P_0) on the ramp. This is possible by reducing or extending the length of the chain

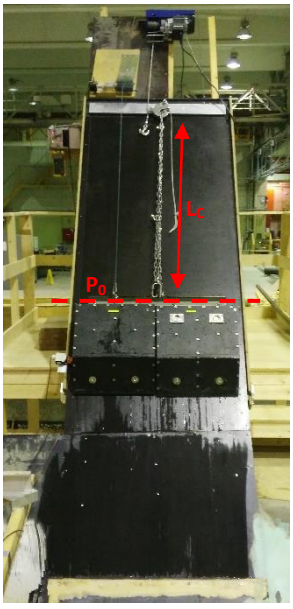

Figure 4.1: picture of blocks on the ramp, with indication of chain length (L_C) and slide starting position (P_0).

(L_C) which keeps rigid blocks before their release. The triggering wheel need also to be relocated up or down, on the ramp side, according to the blocks starting position. Three different chain lengths, that differ by 50 cm each other, are studied for Model A. Other four different slide starting positions are applied in the case of Model B. Each of them is named with a Roman numeral that is higher for lower distance between P_0 and the basin water level; position IV_B is the only exception.

Table 4.1: identification codes of slide starting positions and related chain lengths applied in Model A and Model B.

Model A – 40° ramp slope		*Model B – 50° ramp slope*	
P_0 ID	**L_C [cm]**	**P_0 ID**	**L_C [cm]**
I_A	15	I_B	130
II_A	65	II_B	147
III_A	115	III_B	178
		IV_B	90

The position III_B is chosen trying to achieve the same maximum slide velocity obtained in starting position I_A, by keeping unchanged slide shape and volume (trials 2h.II_A - 2h.III_B and 4.II_A - 4II_B are comparable in terms of slide velocity; see tables 4.4 and 4.5). Slide starting positions lower than III_B are not taken into account because of the impossibility to move the triggering wheel in a lower position on the ramp side. Moreover, it is useless to study cases with slide starting position higher than I_B because the corresponding full scaled slide velocity would be associated to exceptional events. Location IV_B is applied only to analyse slides especially extended in length, avoiding that blocks are too close to the water level.

Six different slide configurations are considered to evaluate the influence of slide width, length and volume on results. Each slide arrangement is named with a number indicating the quantity of blocks involved and, if it is necessary, the horizontal (h) or vertical (v) blocks alignment is specified (see figure 4.2).

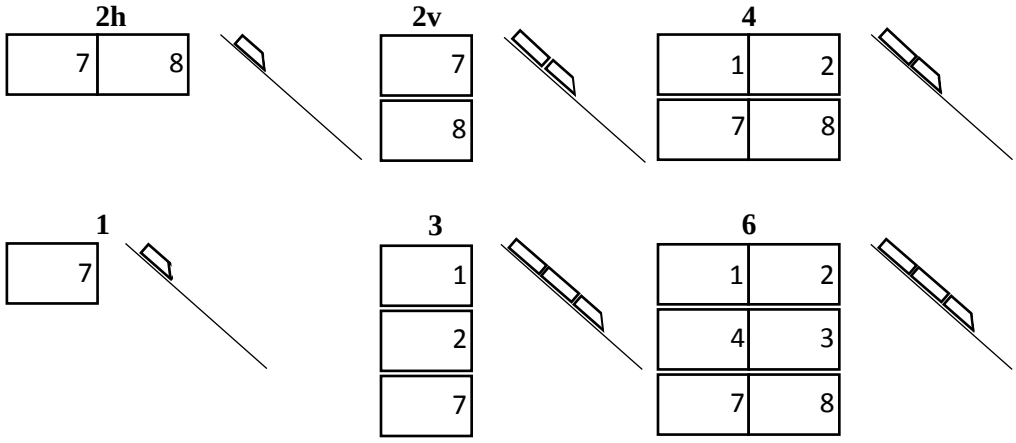

Figure 4.2: schematization of blocks arrangements applied, with related codes.

Table 4.2: slide dimensional characteristics.

Blocks arrangement	Slide length (l_S) [cm]	Slide width (b_S) [cm]	Shape ratio (l_S/b_S) [-]
2h	50	90	0.55
2v	108	45	2.40
4	108	90	1.20
1	50	45	1.11
3	166	45	3.69
6	166	90	1.84

The freeboards studied are associated to dam classes 3 and 4 (see table 4.3), characterized by largest consequences in case of dam failure (*NVE, 2012*). The still water depth, chosen in the majority of experiments, is related to a full scaled freeboard of 4.5 m. In order to have a possible comparison between effects of two different water levels in the reservoir, in some trials the additional 6 m freeboard is analysed.

Table 4.3: freeboard values applied in experiments considering the 1:190 scale.

Consequence class (Norway)	Freeboard_real dam [m]	Freeboard_ model dam [cm]	Still water depth [cm]
3	4.5	2.4	29.5
4	6	3.2	28.7

All tests have an identification code whose first element indicates the blocks arrangement, the second one specifies the slide starting position and the subscript is related to the model type. In case of trials performed with a 6m freeboard, the code subscript also makes the freeboard value explicit (see tables 4.4 and 4.5). At least three trials have been performed for each test type to assure data fitting in terms of slide

velocity variation curve and overtopping volume; the experiments with inconsistent velocity curves have been discarded.

Test 4.I_A has been repeated many times because it corresponds to the trial type on which uncertainties statistical analysis is based. In cases 4.II_A and 4.III_A only one experiment has been carried out, therefore the reliability of obtained results is smaller.

Table 4.4: list of tests conducted with related ID codes, Model A. Δb is the distance between the slide centre of mass and the basin water level; Δa is the distance between the slide lower end and the basin water level.

Model A

Test ID	Starting position	Amount of blocks used	Freeboard [cm]	Δb [cm]	Number of trials performed	Δa [cm]
2h.I_A	I_A	2	2.4	272	3	247
2v.I_A	I_A	2	2.4	243	3	189
4.I_A	I_A	4	2.4	243	27	189
2h.II_A	II_A	2	2.4	222	3	197
2v.II_A	II_A	2	2.4	193	4	139
4.II_A	II_A	4	2.4	193	1	139
2h.III_A	III_A	2	2.4	172	4	147
2v.III_A	III_A	2	2.4	143	3	89
4.III_A	III_A	4	2.4	143	1	89

Table 4.5: list of tests conducted with related ID codes, Model B. Δb is the distance between the slide centre of mass and the basin water level; Δa is the distance between the slide lower end and the basin water level.

Model B

Test ID	Starting position	Amount of blocks used	Freeboard [cm]	Δb [cm]	Number of trials performed	Δa [cm]
2h.I_B	I_B	2	2.4	251	3	226
2v.I_B	I_B	2	2.4	222	3	168
4.I_B	I_B	4	2.4	222	3	168
1.II_B	II_B	1	2.4	234	4	209
2h.II_B	II_B	2	2.4	234	4	209
2v.II_B	II_B	2	2.4	205	3	151
4.II_B	II_B	4	2.4	205	7	151
1.II_{B_6}	II_B	1	3.2	233	3	208
2h.II_{B_6}	II_B	2	3.2	233	3	208
2v.II_{B_6}	II_B	2	3.2	204	3	150
4.II_{B_6}	II_B	4	3.2	204	3	150
2h.III_B	III_B	2	2.4	203	6	178

2v.III$_B$	III$_B$	2	2.4	174	3	120
4.III$_B$	III$_B$	4	2.4	174	4	120
2h.III$_{B_6}$	III$_B$	2	3.2	202	4	177
2v.III$_{B_6}$	III$_B$	2	3.2	173	4	119
4.III$_{B_6}$	III$_B$	4	3.2	173	4	119
3.IV$_B$	IV$_B$	3	2.4	233	4	150
6.IV$_B$	IV$_B$	6	2.4	233	3	150
3.IV$_{B_6}$	IV$_B$	3	3.2	232	3	149
6.IV$_{B_6}$	IV$_B$	6	3.2	232	7	149

4.3 Signal processing and filtering

Before processing, gathered raw data need to be multiplied by calibration factors, evaluated during instruments calibration procedure.

Table 4.6: calibration factors applied before data processing.

	Wave height (Ch. 1 - 9)	**Run-up height (Ch. 12 - 14)**	**Overtopping volume**	**Rotational sensor (Ch. 10)**
Calibration factor	$\frac{50\ mm}{1\ V}$	$\frac{50\ mm}{2.4\ V}$	$\frac{1\ dm^3}{5.6\ mm}$	$\frac{0.5\ m}{0.67\ V}$

Despite the instruments adjustment, results are affected by an initial offset respect to the zero value. To fix this problem that interests each channel, recorded value at zero instant is subtracted from all data of the time series. This measurements refining procedure allows samples to show a zero value at the beginning of the record.

The spectral analysis of wave height signals, given by channels 1-9, in some cases revealed the presence of a peak related to a 50 Hz frequency. Signal filtering proved that this electrical interference does not involve important changes in wave height time series. For this reason, it was not considered of importance to process further the wave propagation records.

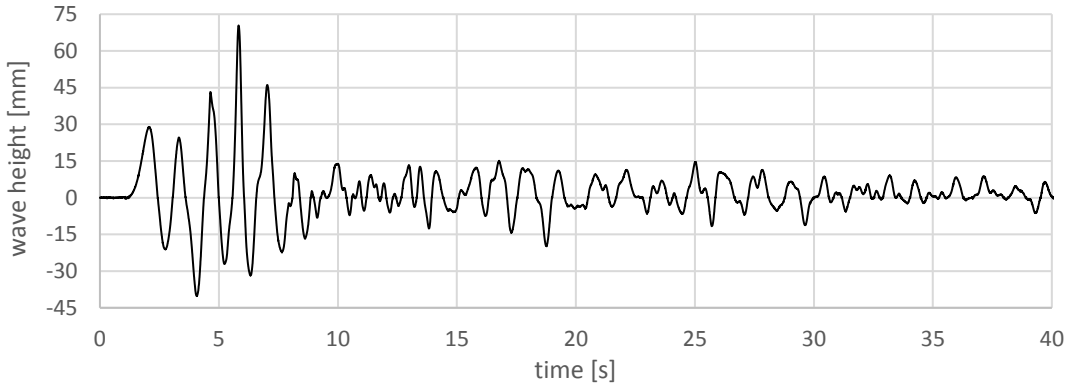

Figure 4.3: diagram of wave height signal recorded by channel 2; trial 2h.II$_A$.

Data returned by channel 10 represent instantaneous position of the slide during the fall. By processing and graphing the time series, slide covered distance (d) can be obtained. This measure consists in the slide path from the starting position (P_0) on the ramp to the point where blocks stop on the basin bottom. Instantaneous position of the slide allows the evaluation of its instantaneous velocity (v) through the relation:

$$v_i = \frac{(d_i - d_{i-1})}{\Delta t} \qquad \textit{Equation 4.2}$$

where the subscript refers to the time instant and Δt is the sample rate equals to 0.005 s. After plotting instantaneous velocity values, it is possible to obtain slide velocity variation curve. Time - velocity diagrams show a significant oscillation during the whole recording time; this noise is due to the same interference discussed above and it is proved by the presence of a 50 Hz peak in spectra. The filtering procedure is essential to remove this disturbance and to work with clean velocity signals. In figure 4.4, slide velocity curve shows that blocks increase their speed during the plunge on the ramp, then, after collision, slide motion is abruptly slowed by water. Furthermore, covered distance curve shows a plateau when slide velocity reaches the zero value. At that moment, slide fall stops and blocks are motionless on the basin bottom. The red cross located on the slide covered distance curve indicates the instant when blocks touch the water and the blue one points out the instant after that blocks are completely submerged in water. Given that, despite the filtering procedure, signal background noise cannot be completely deleted, a polynomial function is applied to filtered velocity signals in order to extrapolate more accurately the peak of velocity curves (see Appendix B "Slide velocity signal processing"). The velocity curve peak is conventionally considered the landslide velocity at the instant of impact with water; it

is a simplification as the slide impact velocity is reached just before the moment related to the curve highest velocity. The diagram below shows that the slide velocity peak instant is very close to the red cross instant; this fact demonstrates the acceptability of considering the slide velocity curve peak as the slide impact velocity (confirmed by *Panizzo et al., 2005*).

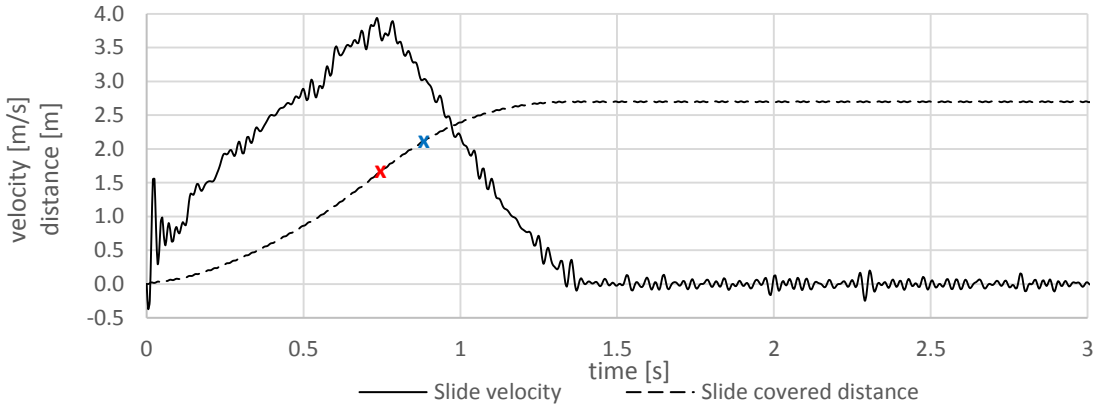

Figure 4.4: diagram of filtered slide velocity and slide covered distance, truncated at 3 s; trial 2h.II$_A$. The red cross indicates the instant when blocks touch the water and the blue one points out the instant after that blocks are completely submerged in the water.

Run-up height values, given by channels 12, 13 and 14, describe the height of water during crossing on the dam. In this case too, spectra reveal the presence of the 50 Hz peak but it is lower than in previous cases. After applying filtering procedure, the curve appears smoother than the original one; however, run-up peak values are not significantly altered. In figure 4.5 the zero level refers to stillwater elevation in the basin and results from each sensor are elevated to represent the elevation of the dam at each location, considering that the dam top is a bit sloped. Channel 13 always starts recording before the other two channels due to the dam shape (see figures 3.10 and 3.12).

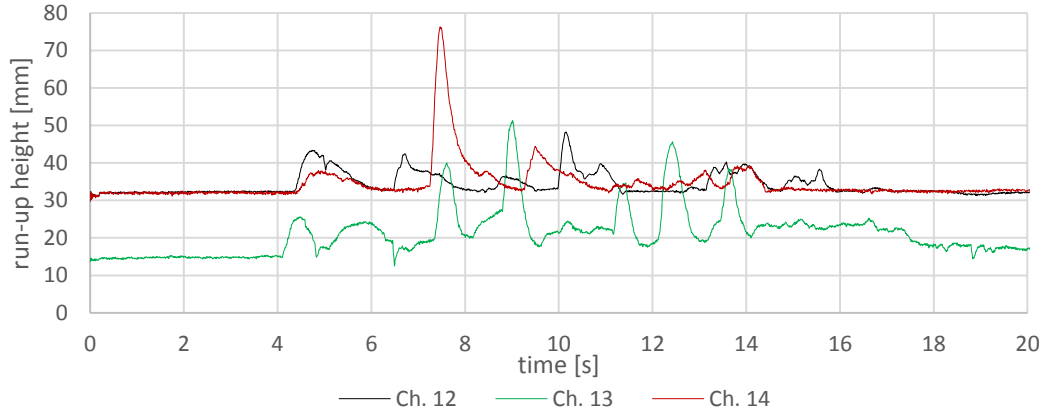

Figure 4.5: diagram of filtered run-up height recorded by channel 12, 13 and 14 truncated at 20 s; trial 2h.II$_A$.

5. Instruments reliability and data statistical analysis

Before proceeding with data analysis, it is necessary to be aware of possible errors that may affect measurements. On Model A, 26 experiments with the same setup ($4.I_A$) have been carried out with the aim of evaluating result repeatability through a statistical assessment. This procedure has been applied to each type of output, estimating variability of results returned by speedometer, wave gauges and ultrasonic sensors. The process comprises three different phases: calculation of normal distribution in observed values, application of Kolmogorov-Smirnov goodness-of-fit test and submission of instruments standard error.

5.1 Dam fixing effects

Prior to starting the experimental study on the model, gaps were noticed along the wooden faces junctions of the dam. Assuming that these gaps would invalidate overtopping volume results, they were filled with an appropriate foam.

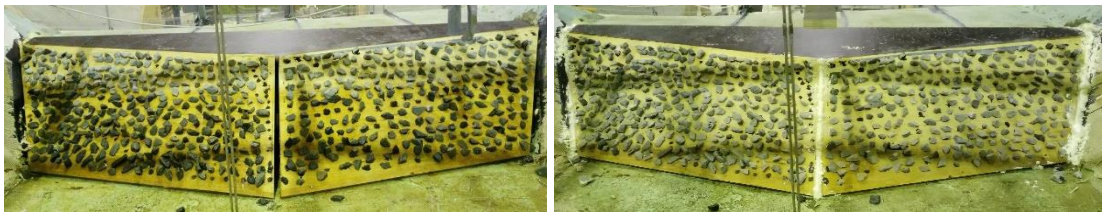

Figure 5.1: pictures of the dam, before fixing (on the left) and after fixing with the application of the foam (on the right).

Investigation into the difference between outgoing water quantities in the two different cases represented in figure 5.1 was conducted by carrying out 10 tests before fixing the dam, and 16 after fixing with the application of the foam.

The gathered data series are used as inputs to obtain the related box plots in Matlab. The following graphs (figures 5.2, 5.3 and 5.4) confirm that the dam structural defects

involve significant alterations in overtopped volumes, especially in the central part of the dam where there is the largest gap. Indeed, the water collected in buckets 2, 3 and 4 is lower in the tests preceding the dam fixing. This analysis also permits to estimate measurements dispersion around median value. The red crosses in the box plot diagrams below are outliers, values not included in a specific range established with the following equation:

$$outlier < q_1 - 1.5\times(q_3 - q_1) \quad \text{V} \quad outlier > q_3 + 1.5\times(q_3 - q_1) \qquad \textit{Equation 5.1}$$

where q_1 and q_3 are the 25th and 75th percentiles of the sample data, respectively.
Basing on diagrams in figures 5.3 and 5.4, it can be noticed that the area of box plots is wider in the case of fixed dam. For this reason, the measurements' scattering around the median is greater. Besides, there are more outliers than in the case with the not fixed dam. It could be due to the major sample's size, that is sign of more reliable statistical analysis.

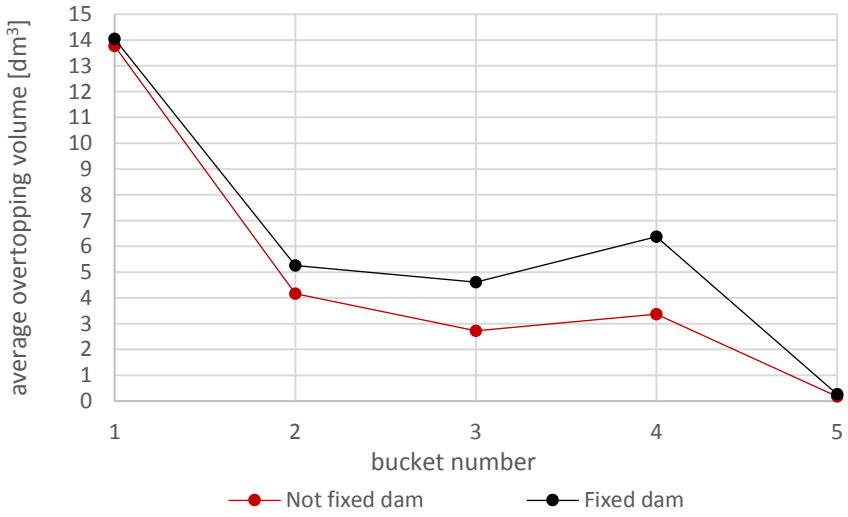

Figure 5.2: the series illustrate the averages of collected overtopping volumes in each bucket, considering results obtained in case of not fixed dam and fixed dam.

Not fixed dam

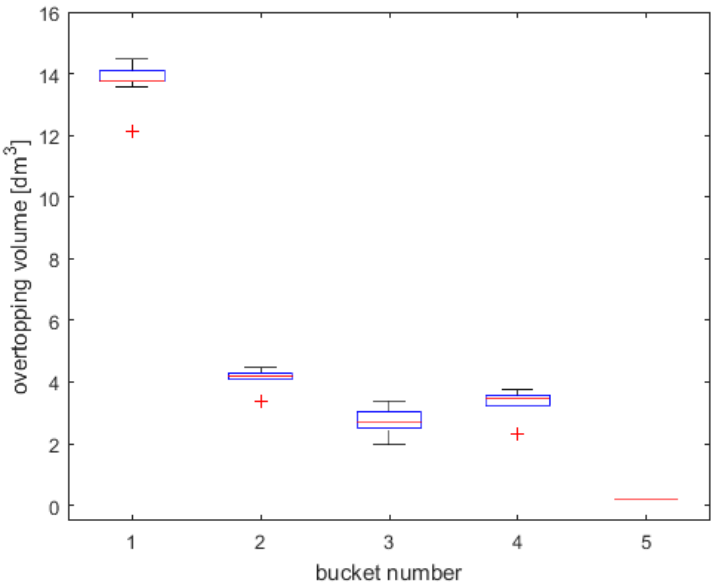

Figure 5.3: box plot per each bucket considering 10 tests performed on Model A before fixing of the dam.

Fixed dam with the application of the foam

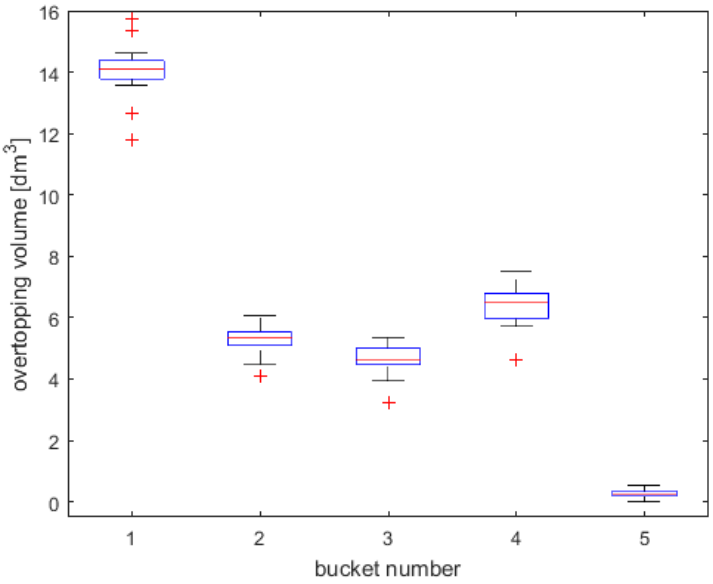

Figure 5.4: box plot per each bucket considering 16 tests performed on Model A after fixing of the dam.

5.2 Normal distribution of data

Accidental errors are inevitable random errors that occur without regard to any known physical law or pattern. These errors can be evaluated by repeating many times the same test, indeed results scattering represents an important indication of measurements error. It is known that physical measurements often follow a normal distribution. Gaussian curve is bell-shaped, entailing that many values are similar to the series mean, the distribution central value, and that the number of positive and negative deviations compared to the average is almost the same.

Basing on gathered experimental data, a bar graph could be made out of the numbers of occurrences of each value: if the shape of the histogram resembles a bell curve, the data distribution is likely normal. In order to compare the histogram with the normal distribution curve, calculated on the basis of the observed values, the height of each bar (f_k) is defined as:

$$f_k \times \Delta x_k = \frac{n_k}{N} \qquad \textit{Equation 5.2}$$

Where Δx_k is the k-bar width, n_k is the number of measurements included in the k-class and N is the number of values in the sample.

This procedure has been applied to all outputs: 16 replicate trials have been considered for statistical analysis of wave height, run-up height and overtopped volume results, whereas 26 tests (performed both before and after dam fixing) have been taken into account for statistical analysis of slide impact velocity values.

Here below (figure 5.5) are some diagrams illustrating the overlapping between the histograms and the Gaussian curve.

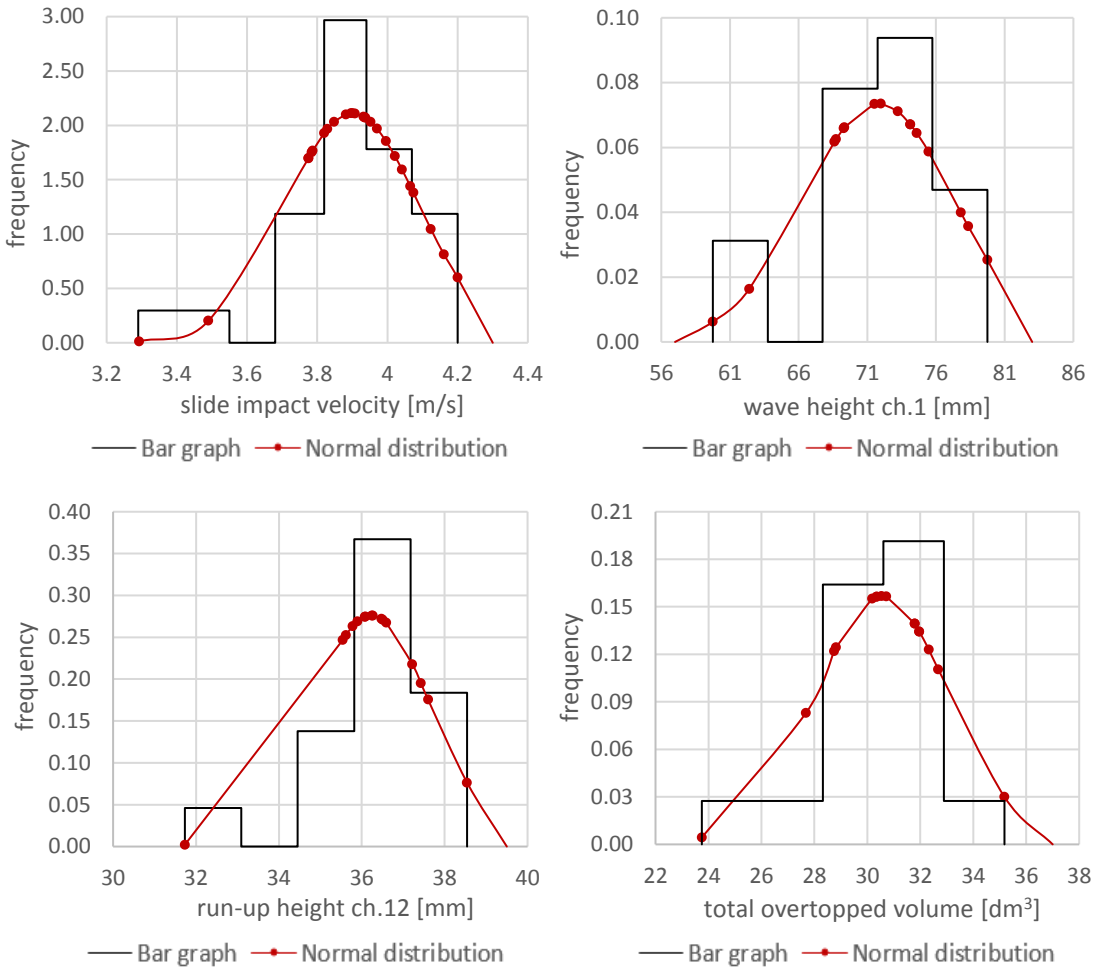

Figure 5.5: the diagrams show the overlapping of bar graph and normal distribution curve evaluated in observed values. They consider slide impact velocity data series, wave height peaks recorded by channel 1, run-up height peaks returned by channel 12 and total overtopped water volume, respectively.

The histograms seem to resemble a normal distribution. The Kolmogorov-Smirnov goodness-of-fit test is applied to verify that data actually follow a Gaussian distribution (null hypothesis). This nonparametric test quantifies the distance between the empirical distribution function of the sample (F_n), evaluated as cumulative relative frequency, and the cumulative normal distribution function (F) basing on the Kolmogorov-Smirnov's statistic:

$$D_n = sup_x|F_n(x) - F(x)| \qquad \textit{Equation 5.3}$$

Where *n* is the number of observations *x*.

The significance level, denoted by α, is the probability of rejecting the null hypothesis when it is true. If the value of α is lower, the acceptance region of null hypothesis is wider but the test accuracy is reduced. The significance levels considered are 0.2, 0.15,

0.10, 0.05, 0.01. Tables 5.1, 5.2, 5.3 and 5.4 report the values of mean and standard deviation for all data series and also indicate the α limit value to accept the null hypothesis; when there is no indication of significance level, the null hypothesis is always rejected. For this reason, the data series returned by channels 6, 12 and 14 have been further analysed: the outliers recognised by box plots implementation have been deleted and the Kolmogorov-Smirnov test has been applied again on the new data series.

Table 5.1: parameters of normal distribution, evaluated considering wave height peaks series, used for applying Kolmogorov-Smirnov goodness-of-fit test.

	Ch.1	**Ch.2**	**Ch.3**	**Ch.4**	**Ch.5**	**Ch.6**	**Ch.7**	**Ch.8**	**Ch.9**
μ [mm]	71.7	67.0	57.6	108.4	63.5	46.7	107.5	58.7	46.7
σ [mm]	5.6	10.0	1.8	5.9	8.9	8.9	6.4	3.5	1.6
α_{limit}	0.2	0.2	0.05	0.05	0.2	-	0.2	0.2	0.2

Table 5.2: parameters of normal distribution, evaluated considering run-up height peaks series, used for applying Kolmogorov-Smirnov goodness-of-fit test.

	Ch.12	**Ch.13**	**Ch.14**
μ [mm]	36.2	35.3	55.2
σ [mm]	1.4	3.0	10.3
α_{limit}	-	0.2	-

Table 5.3: parameters of normal distribution, evaluated considering slide impact velocity series, used for applying Kolmogorov-Smirnov goodness-of-fit test.

	Slide impact velocity
μ [m/s]	3.9
σ [m/s]	0.2
α_{limit}	0.01

Table 5.4: parameters of normal distribution, evaluated considering overtopped water volume series, used for applying Kolmogorov-Smirnov goodness-of-fit test.

	Total overtopped water volume
μ [dm^3]	30.6
σ [dm^3]	2.5
α_{limit}	0.1

Figures 5.6, 5.7 and 5.8 show the overlapping between the empirical and the normal distributions for measurements from channels 6, 12 and 14 respectively. In the first case, even if outlier has been deleted, the null hypothesis is not accepted; indeed, the signal returned by this sensor usually presents anomalous oscillations. Since it is a systematic error of the instrument, wave gauge 6 has been replaced. On the contrary, channel 12 and 14 measurements, after outliers removal, both pass the test with a significance level of 0.2.

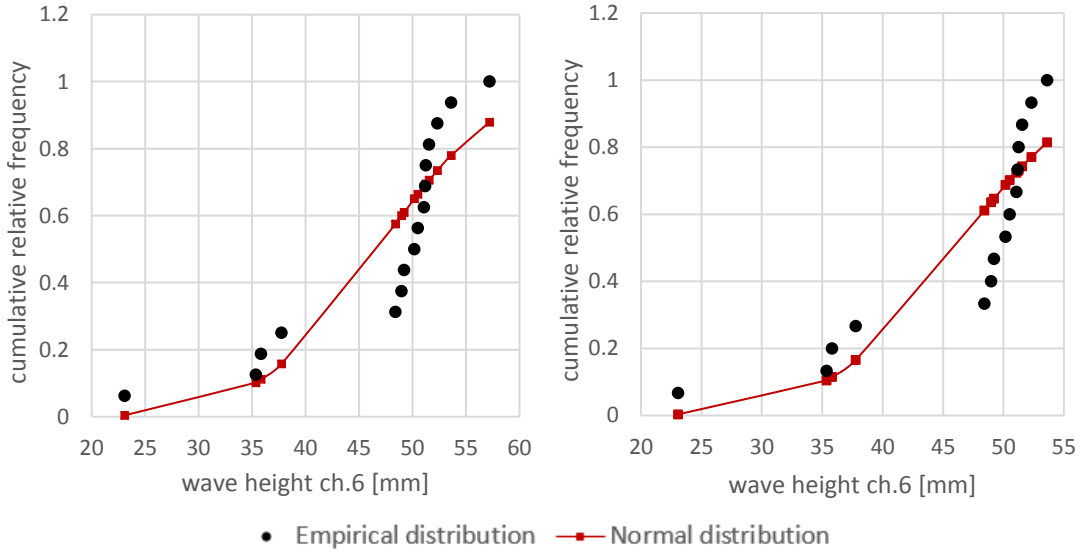

Figure 5.6: the diagrams show normal and empirical distributions of wave height peaks recorded by channel 6. The graph on the left is obtained considering the entire sample, instead, the one on the right is evaluated after removal of outliers.

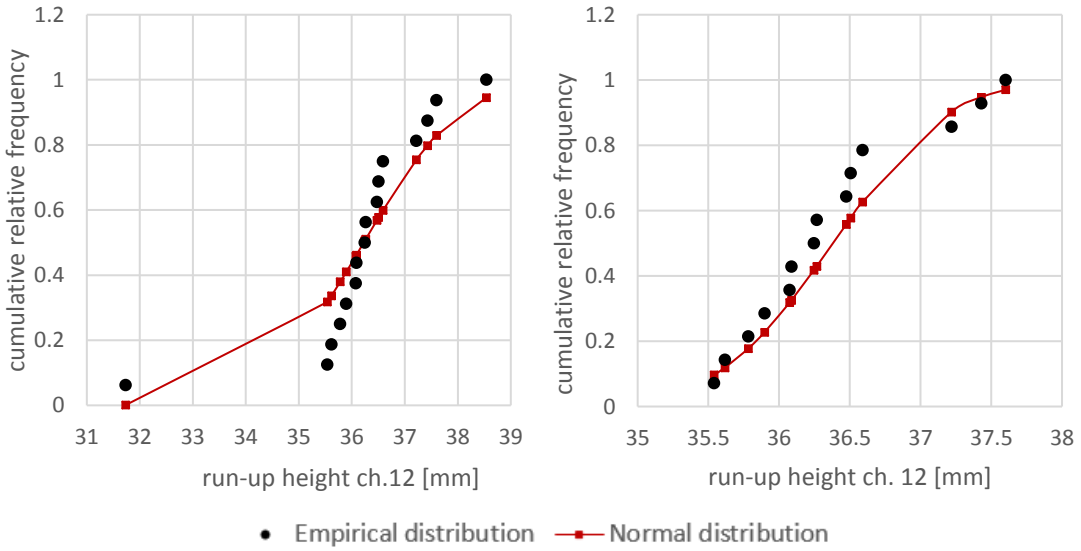

Figure 5.7: the diagrams show normal and empirical distributions of run-up height peaks recorded by channel 12. The graph on the left is obtained considering the entire sample, instead, the one on the right is evaluated after removal of outliers.

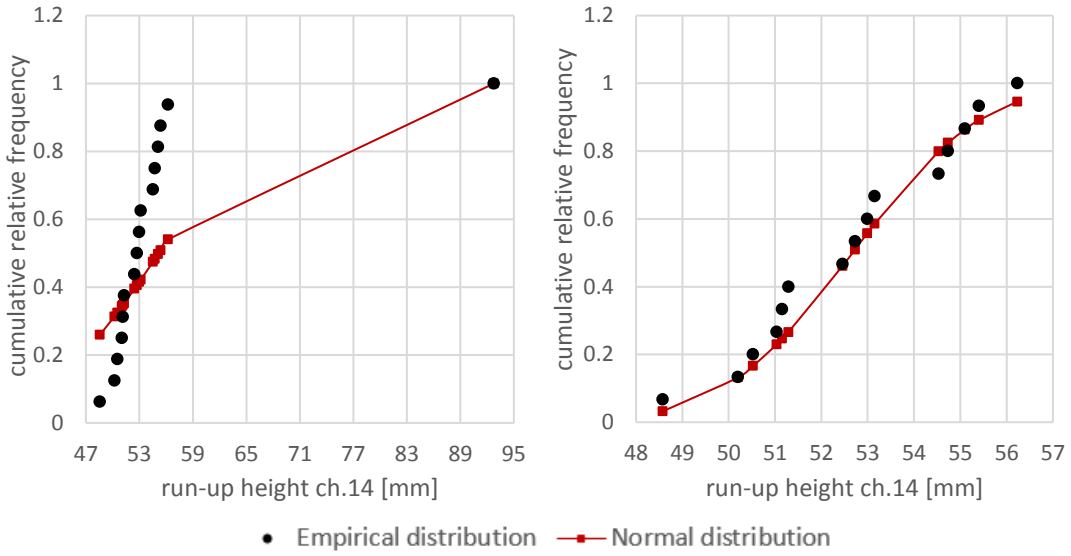

Figura 5.8: the diagrams show normal and empirical distributions of run-up height peaks recorded by channel 14. The graph on the left is obtained considering the entire sample, instead, the one on the right is evaluated after removal of an outlier.

5.3 Measurement of the standard error

Standard error is a statistical term that determines the accuracy of samples by analysing the deviation within the means. The formula for the standard error of the mean is:

$$\sigma_M = {}^{\sigma}/_{\sqrt{N}} \qquad \textit{Equation 5.4}$$

where σ is the standard deviation of the original distribution and N is the sample size. If more data points are involved in the calculation of the mean, the standard error tends to be smaller. When the latter is small, data are said to be more representative of the true mean.

This evaluation has been applied to all types of output considered in the following analysis for estimating results variability (see tables 5.5, 5.6, 5.7 and 5.8).

Table 5.5: standard errors evaluated for wave height peaks series, evaluated including outliers.

Wave height peaks [mm]								
Ch.1	**Ch.2**	**Ch.3**	**Ch.4**	**Ch.5**	**Ch.6**	**Ch.7**	**Ch.8**	**Ch.9**
± 1.4	± 2.5	± 0.5	± 1.5	± 2.2	± 2.2	± 1.6	± 1.0	±0.4

Table 5.6: standard errors evaluated for run-up height peaks series, evaluated including outliers.

Run-up height peaks [mm]		
Ch.12	**Ch.13**	**Ch.14**
± 0.4	± 0.7	± 2.6

Table 5.7: standard error evaluated for slide impact velocities series, evaluated including outliers.

Slide impact velocity [m/s]
± 0.04

Table 5.8: standard error evaluated for overtopped water volumes series, evaluated including outliers.

Total overtopped water volume [dm^3]
± 0.5

6. Results analysis and discussion

This chapter focuses on model results analysis and discussion. Each output is studied in a specific paragraph which explains how the analysis is implemented and shows results elaboration. Model B outcomes are thoroughly discussed, since they embrace a wider range of sliding phenomenon effects on generated waves in the basin. A comparison between Model A and Model B is only carried out for significant cases.

6.1 Slide velocity analysis

The slide starting position on the ramp directly influences the slide velocity and the moment when the blocks impact with water. Reducing the chain length (Lc), the distance between slide centre of gravity and water level (Δb) decreases (see Tables 4.4 and 4.5). In case of smaller barycentre heights, the slide covers a shorter path on the ramp and, consequently, its impact velocity is lower and anticipated. This behaviour can be observed for all the studied slide arrangements in different starting positions on the ramp (see Table 4.1). Diagrams corresponding to two blocks horizontally organized are shown below in figure 6.1 as examples.

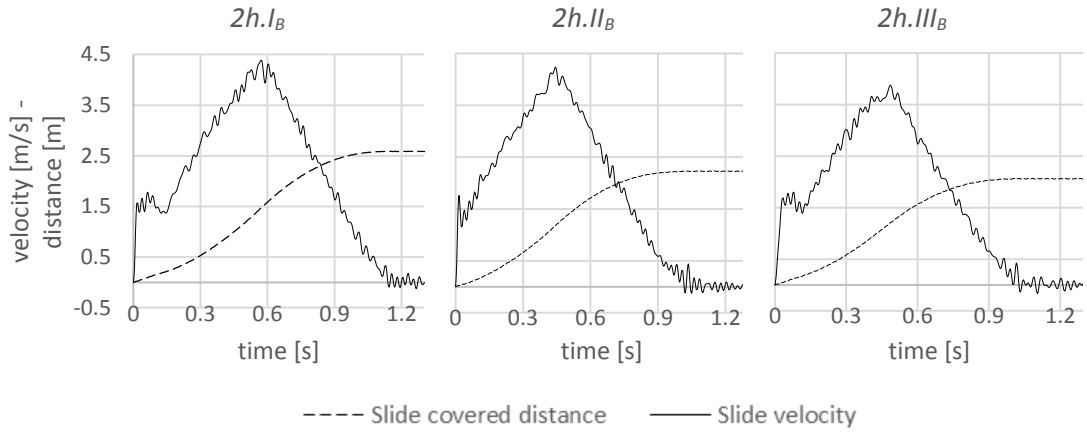

Figure 6.1: variation of slide velocity and covered distance considering three different slide starting positions on the ramp for the same slide arrangement (trials 2h.I_B, 2h.II_B, 2h.III_B).

Slide velocity curves vary according to the number of rigid blocks rows composing the slide. The block arrangement, not only defines the slide barycentre position, but also modifies the velocity curve shape. Indeed, when the slide is made up of more than one raw of blocks, its velocity diagram shows an additional peak following the main one (see figures 6.3 and 6.4). The first peak occurs just after the blocks impact with water, whereas the second peak is due to the collision between different slide blocks rows during submersion. It is clear that this behaviour does not affect velocity curve related to slides composed by one block or two blocks horizontally arranged (see figure 6.2).

Comparing the distance between crosses in figures 6.2, 6.3 and 6.4, it is also evident that slides with a larger number of rows take a longer time to be completely submerged.

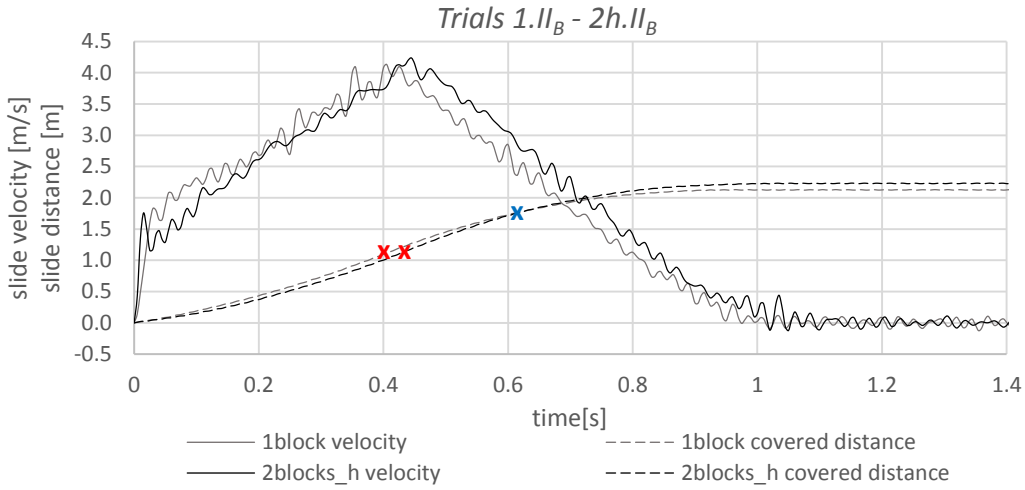

Figure 6.2: overlapping of slide velocity and covered distance curves for two trials with the same slide centre of mass (tests 1.II$_B$ and 2h.II$_B$). Red crosses point out the instant when blocks impact with water. The blue cross points out the instant when blocks are completely submerged; this instant is the same for both trials 1.II$_B$ and 2h.II$_B$.

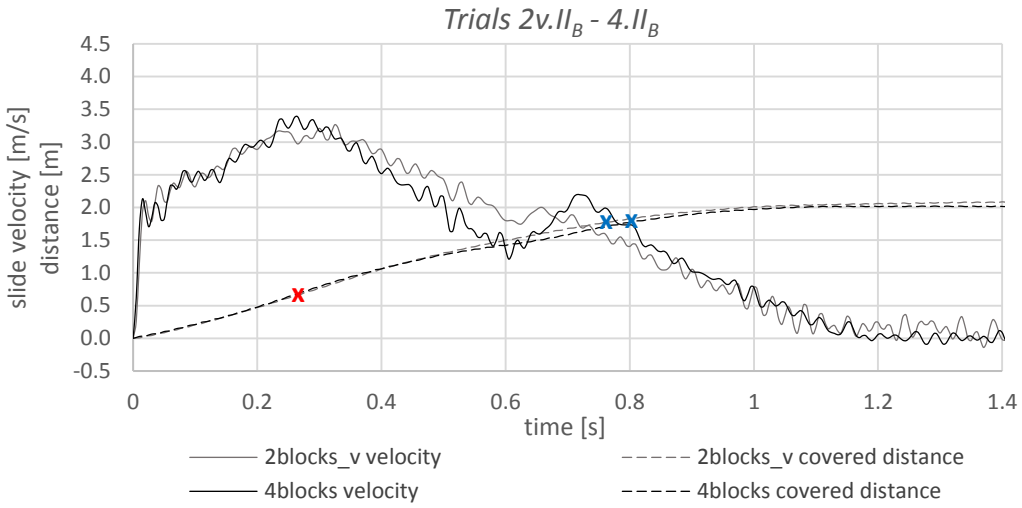

Figure 6.3: overlapping of slide velocity and covered distance curves for two trials with the same slide centre of mass (tests 2v.II$_B$ and 4.II$_B$). The red cross points out the instant when blocks impact with water; this instant is the same for both trials 2v.II$_B$ and 4.II$_B$. Blue crosses point out the instant when blocks are completely submerged.

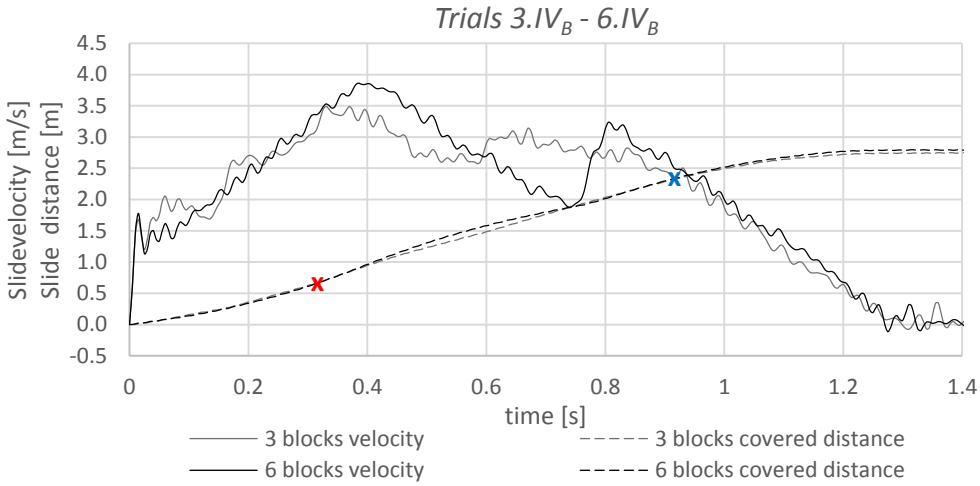

Figure 6.4: overlapping of slide velocity and covered distance curves for two trials with the same slide centre of mass (tests 3.IV$_B$ and 6.IV$_B$). The red cross points out the instant when blocks impact with water; this instant is the same for both trials 3.IV$_B$ and 6.IV$_B$. The blue cross points out the instant when blocks are completely submerged; this instant is the same for both trials 3.IV$_B$ and 6.IV$_B$.

Velocity curves peak has been evaluated for all slide configurations following the procedure explained in Appendix B “Slide velocity signal processing”.

Table 6.1: velocity curves peak for all tests performed on Model A and Model B; each measurement is evaluated with a standard error of ±0.04 m/s.

Slide impact velocity [m/s] Model A			
	I_A	**II_A**	**III_A**
2h	4.37	3.75	3.03
2v	3.90	3.37	2.43
4	3.85	3.32	2.46

Slide impact velocity [m/s] Model B							
	I_B	**II_B**	**II_{B_6}**	**III_B**	**III_{B_6}**	**IV_B**	**IV_{B_6}**
2h	4.15	4.10	4.02	3.68	3.39	-	-
2v	3.58	3.18	3.14	2.97	2.71	-	-
4	3.58	3.32	3.33	3.10	2.55	-	-
1	-	3.89	3.83	-	-	-	-
3	-	-	-	-	-	3.30	3.17
6	-	-	-	-	-	3.76	3.80

Concerning figures 6.5, 6.6 and 6.7 below, it is possible to draw some conclusions (see table 4.2 about slide dimensional characteristics and tables 4.4 and 4.5 about parameters of tests conducted).

Figure 6.5 illustrates the relation between slide impact velocity and distance between slide centre of mass and water level (Δb). In trials having equal slide length (cases 1-2h, 2v-4 and 3-6) the slide impact velocity increases according to slide volumes. Instead, considering constant slide volumes and shapes, tendency lines show that slide impact velocity increases according to the distance Δb.

Figure 6.6 shows the relation between the slide impact velocity and the distance between slide lower end and water level (Δa). If the distance covered by the slide on the ramp before its impact with water (which can be assimilated to Δa) increases, the slide impact velocity grows. Considering constant Δa, the slide impact velocity is higher for bigger slide volumes.

Figure 6.7 points out the relation between the slide impact velocity and the slide shape ratio (l_S/b_S). Considering similar slide barycentre positions on the ramp, it is possible to extract the slide shape influence on impact velocity. Indeed, velocity peak values prove to be always higher for trials with 2h arrangement, which present a slide that is wider than longer, therefore characterized by the lowest value of shape ratio (l_S/b_S). In wider terms, among cases with similar Δb, the slide impact velocity is always higher for slide configurations identified by a lower shape ratio.

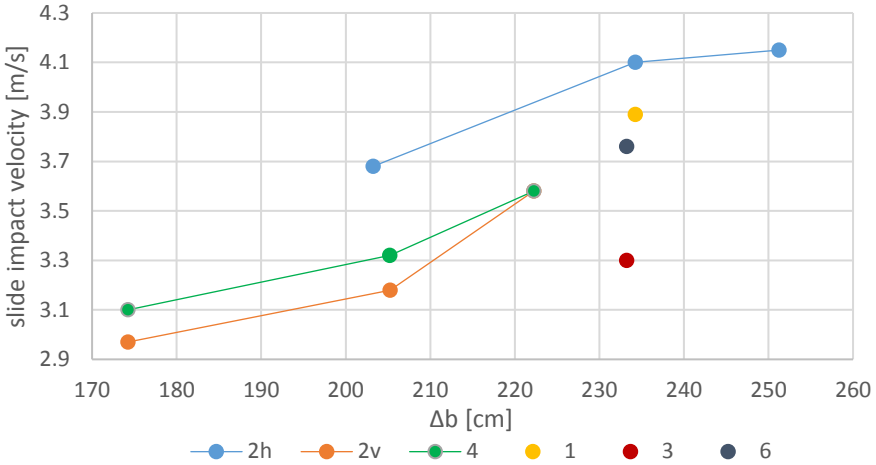

Figure 6.5: the diagram shows the relation between slide centre of mass position and slide impact velocity, for all trial arrangements performed on Model B.

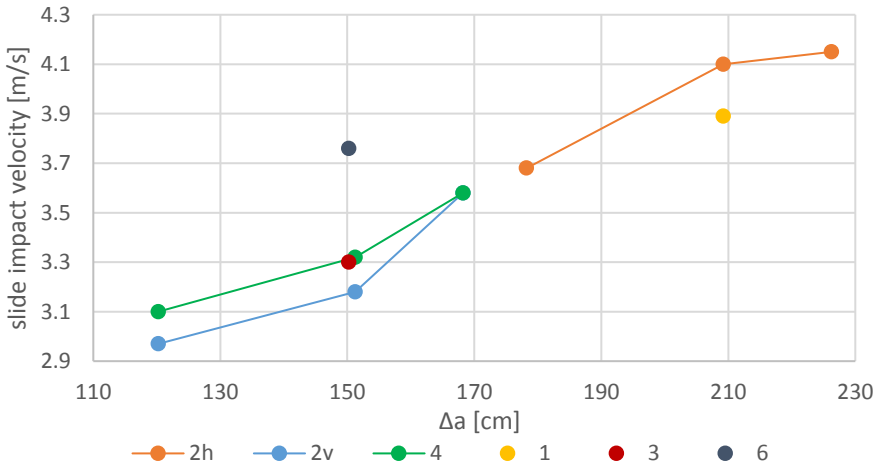

Figure 6.6: the diagram shows the influence of distance between slide lower end and basin water level on slide impact velocity, for all trial arrangements performed on Model B.

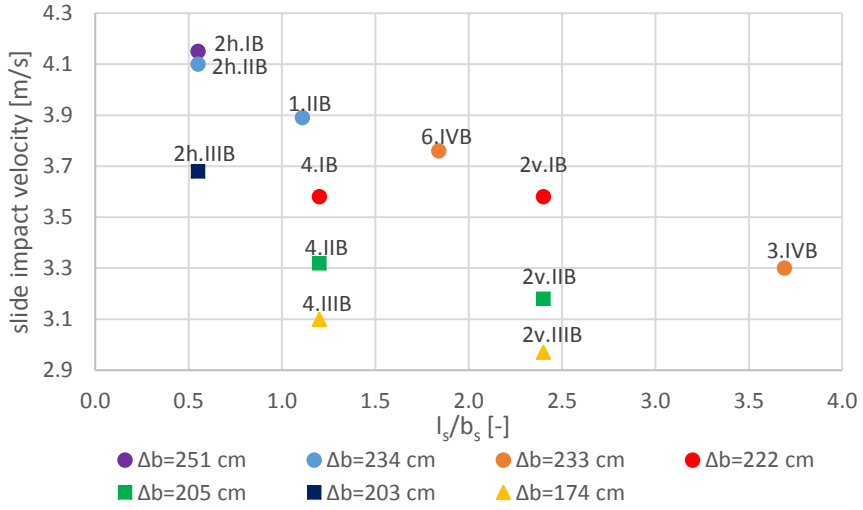

Figure 6.7: the diagram shows the influence of slide shape on slide impact velocity, for all studied distances between the slide centre of gravity and the water level in Model B. Circular symbols are referred to trials with Δb=222 to 251 cm, square symbols are referred to trials with Δb=203 to 205 cm and triangular symbols are referred to trials with Δb=174 cm.

6.2 Wave propagation analysis

In addition to trials video recordings, waves propagation in the trapezoidal basin has been simulated using a Matlab code. The aim of the simulation is to make a qualitative evaluation of the phenomenon, setting measurements returned by channels from 1 to 9 as inputs. Starting from real model dimensions, a regular mesh has been created and wave height values have been associated to corresponding spatial coordinates in the grid. Sections corresponding to 1-2-3 and 7-8-9 in-line sensors limit the representation of water motion in the basin.

Implementing the code, simulation videos have been created for each test performed. Basing on these elaborations, two different propagation modes can be recognized in Model A and Model B because of rebuilding effects. However, in both models, there are no significant differences between the various slide arrangements effects on impulse waves propagation (see Appendix C "Video screenshots regarding wave propagation consistencies in trials with different slide arrangements").

The wave pattern in the basin is complex and, for the purpose of discussion, a simplification is adopted, focusing on the first recorded impulse waves. In all cases analysed from this point forward, the first wave that reaches the dam, generated by the slide impact with the quiescent water body, is defined as the "incident wave". All subsequent waves are named "reflected waves", although their formation may be more complex than being only from reflection; the highest wave, visible in this train of waves following the incident one, is called "main reflected wave".

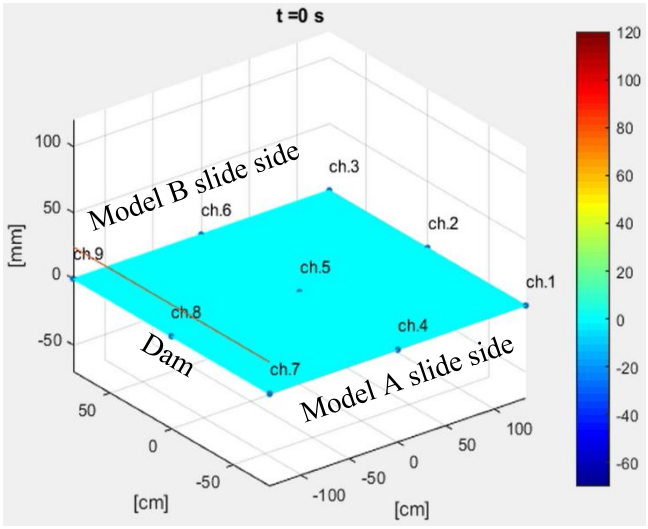

Figure 6.8: screenshot of the wave propagation video at time zero (before slide fall), with indication of slide position in Model A and Model B. The red line specifies the dam top level, above which overtopping may occur.

6.2.1 Wave propagation in Model A

Slide falling generates a wave extended for all the basin width, which propagates in a one-dimensional way towards the dam (figure 6.9). However, wave heights are slightly higher in the right basin side. This behaviour involves a significant water level increase in channels closest to the dam, suggesting possible overtopping.

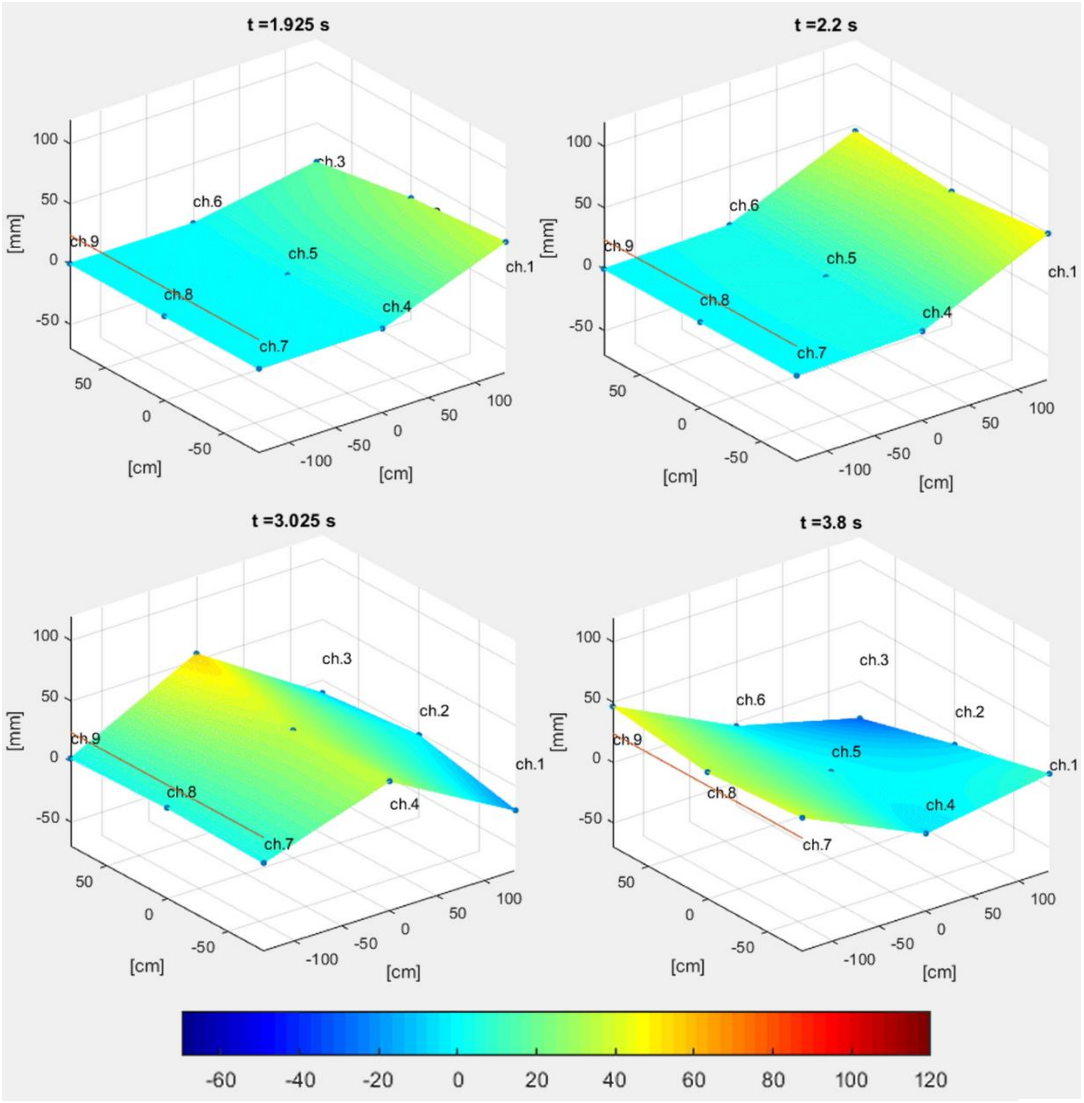

Figure 6.9: video screenshots at time 1.925, 2.2, 3.025 and 3.8 seconds illustrating incident wave propagation in the basin; trial 4.I_A.

Another important wave is generated by the many reflected waves and it potentially arises from the model effects (figure 6.10). These reflections are probably caused by the presence of a structural protuberance in the model side opposite to the slide ramp. In addition to this structural disturbance, other phenomena may possible be involved in forming the waves such as wave interference and wave shoaling due to the step in

the bottom of the basin. Wave height reaches its maximum value in channel 4, as a result of wavelets overlapping. Then, it spreads from there to channel 7, along the left basin side considering the wave propagation direction; this likely implies dam overtopping.

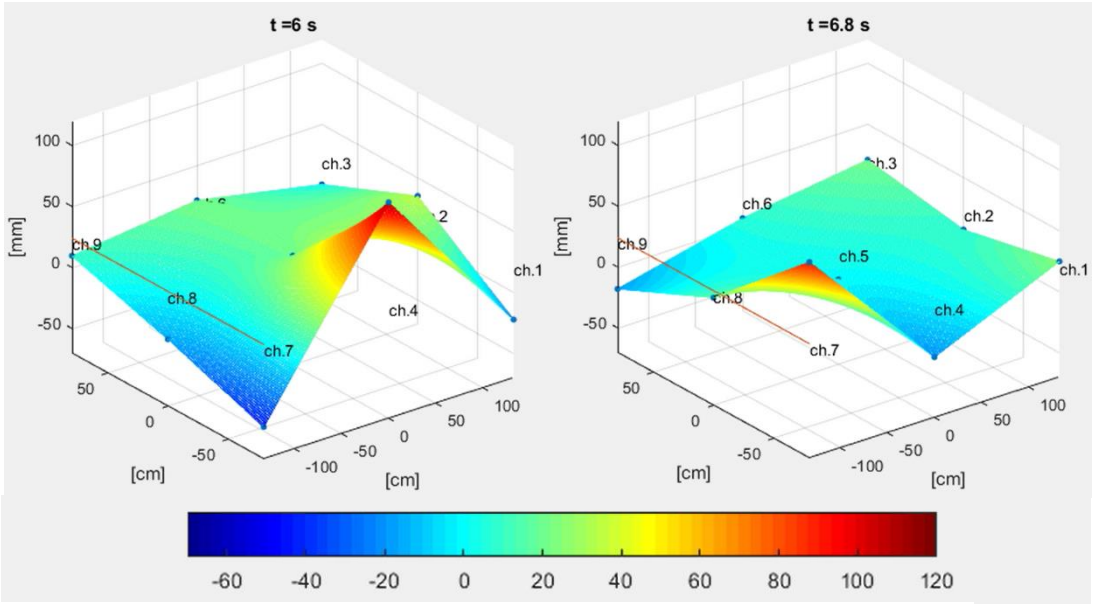

Figure 6.10: video screenshots at time 6 and 6.8 seconds illustrating main reflected wave propagation in the basin; trial 4.I_A.

Wave recorded after 7 seconds are not as relevant as previous ones: basin internal reflections continue but wave heights attenuate. Other minor waves occur in channel 7, 8 and 9 until around t=16 s.

The following figure 6.11 is a scheme of the propagation of the incident and main reflected waves; the structural protuberance in the basin side opposite to the slide ramp is also illustrated.

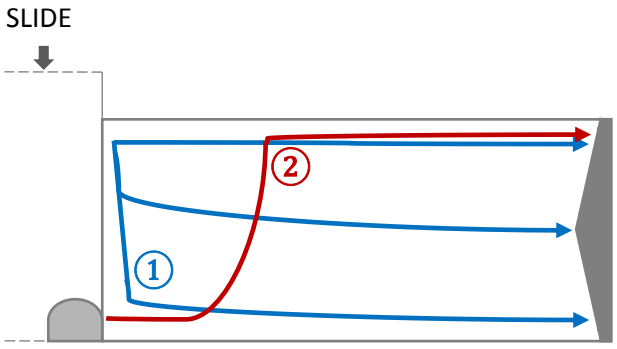

Figure 6.11: schematization of waves propagation in the basin, considering Model A. Number 1 is referred to the incident wave and number 2 is referred to the main reflected wave.

The diagrams in figure 6.12 are a confirmation of incident wave one-dimensionality: first wave peak occurs almost simultaneously in channels 7, 8 and 9. Basing on this simplification it is possible to calculate the average velocity of the incident wave; considering the path between channels 3 and 9, through propagation direction, an average velocity of 1.9 m/s has been estimated. The third peak recorded by channel 7 corresponds to the main reflected wave discussed above; it is higher than the one associated to the incident wave, suggesting that a constructive interference phenomenon probably occurs.

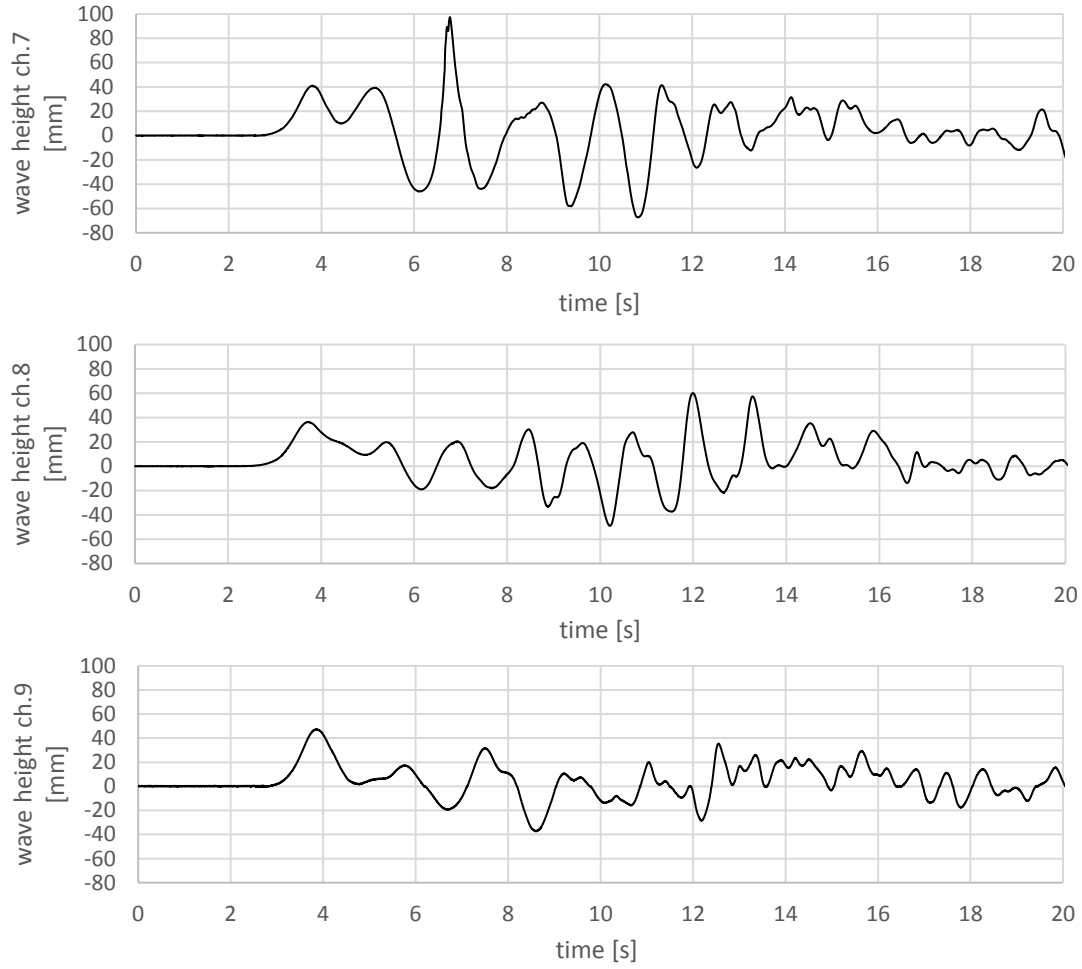

Figure 6.12: wave height signals measured by in line sensors 7, 8 and 9 (trial 4.I_A).

6.2.2 Wave propagation in Model B

Blocks sliding in the basin produces a sudden water level increase, progressively in channels 3, 2 and 1; the last one, opposite to the slide ramp, records the highest peak of incident wave, which grows not only according to the slide volume but also

according to the slide length. The incident wave propagates in an almost one-dimensional way towards the dam, even if, unlike Model A, considering the propagation direction, wave heights are higher in the left basin side. As a consequence, wave height in channels 7, 8 and 9 increases; the overtopping seems to occur on the entire dam length, with bigger quantity of water beyond channel 7 (figure 6.13).

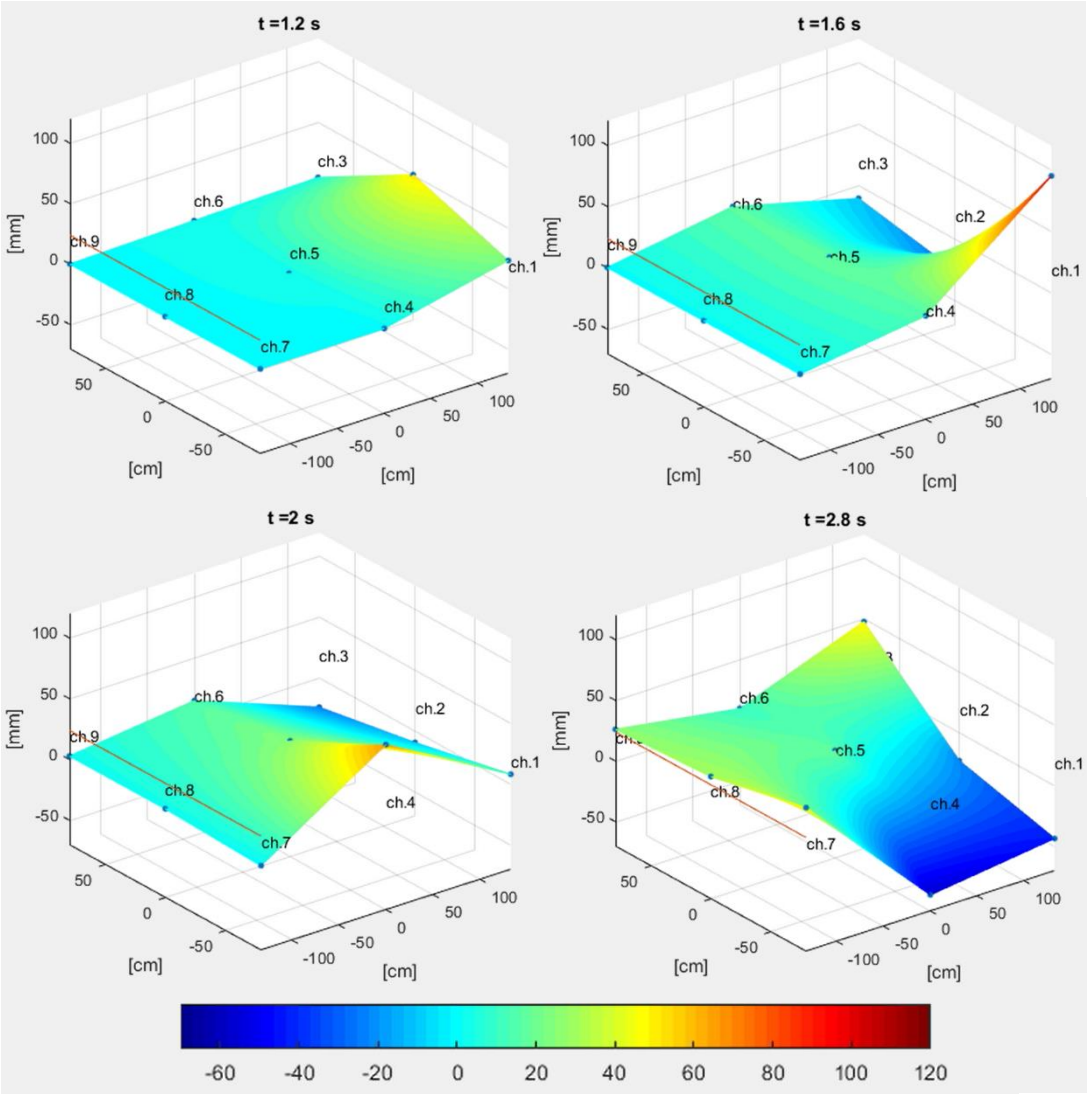

Figure 6.13: video screenshots at time 1.2, 1.6, 2 and 2.8 seconds illustrating incident wave propagation in the basin; trial 4.I$_B$.

A reflected wave is generated immediately after the incident one, as it can be seen in figure 6.14. It is caused by blocks collision against the basin bottom throughout slide submersion. This wave, in fact, arises in channel 2 and moves towards channel 3, hitting the basin side. Then, it proceeds unto channel 9 entailing a possible dam overtopping.

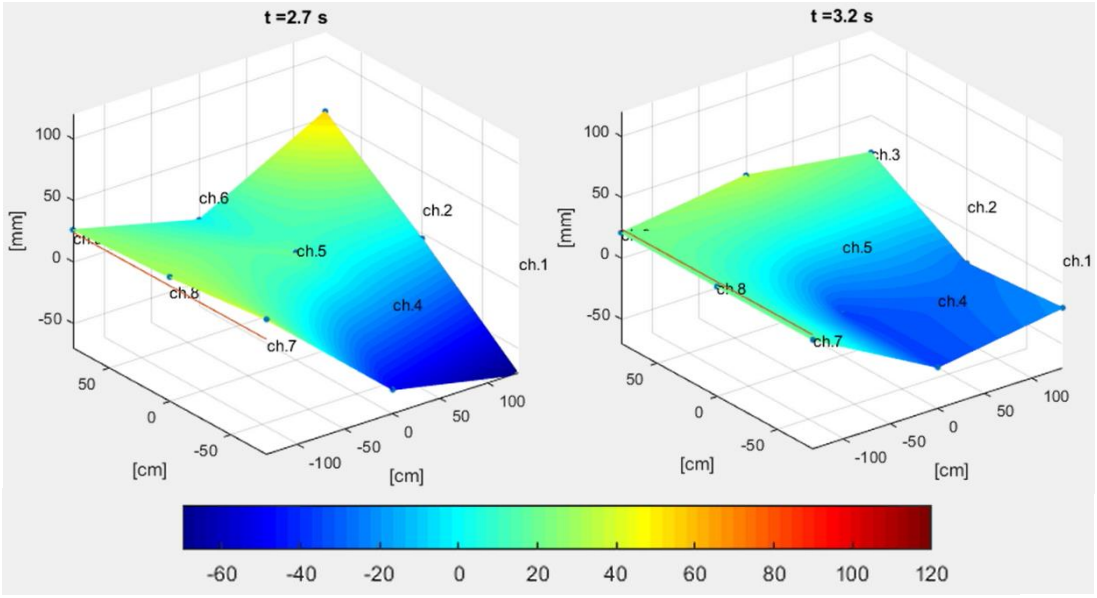

Figure 6.14: video screenshots at time 2.7 and 3.2 seconds illustrating the first reflected wave propagation in the basin; trial 4.$I_{B.}$

The next reflected wave, that can be observed in the wave propagation video, shown in figure 6.15, is the main one. It is not caused by the physical protuberance present in Model A, because in Model B the ramp has been aligned with the basin opposite side, closer to the dam, during model rebuilding. The main reflected wave can be due to the collision of water moved by the slide submersion against the basin side opposite to the ramp; it is recorded firstly by channel 1 and 2, then it propagates towards the dam along channels 3, 6 and 9 progressively.

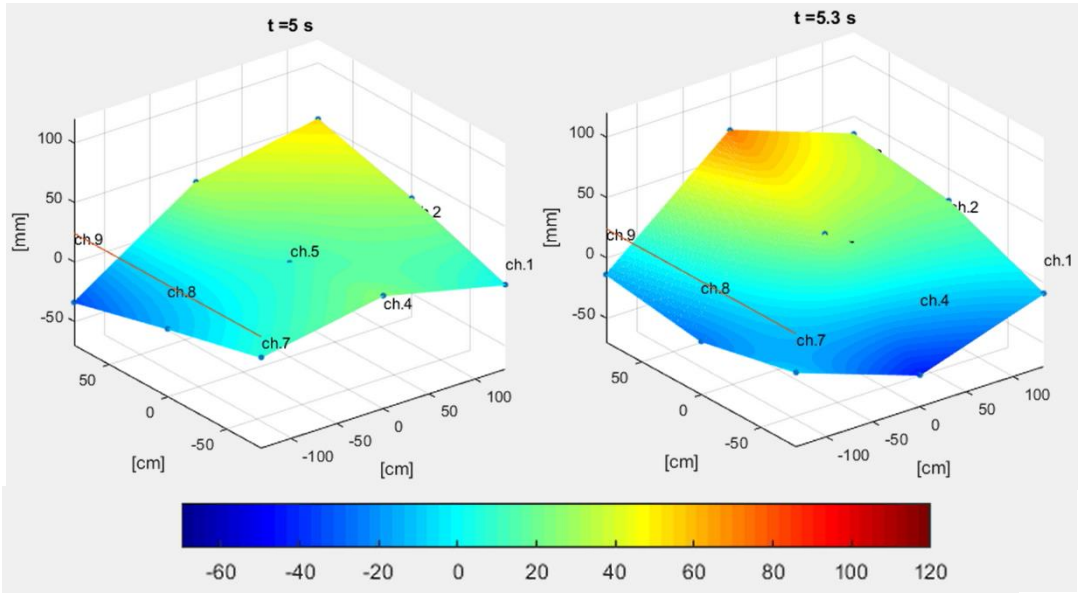

Figure 6.15: video screenshots at time 5 and 5.3 seconds illustrating main reflected wave propagation in the basin; trial 4.$I_{B.}$

Other minor waves are measured in proximity to the dam, until about t=14 s. They are due to ongoing reflections in the basin, across the main propagation direction, dissipating waves energy.

Figure 6.16 shows a schematization of waves propagation in the basin.

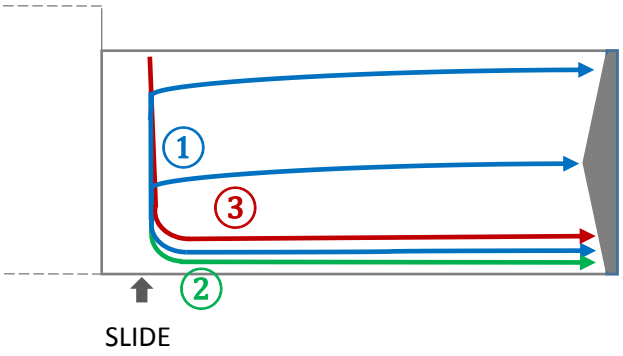

Figure 6.16: schematization of waves propagation in the basin, considering Model B. Number 1 is referred to the incident wave, number 2 is referred to the first reflected wave and number 3 is referred to the main reflected wave.

Diagrams in figures 6.17a and 6.17b prove that, despite Model A case, channels 7, 8 and 9 measure the incident wave peak at slightly different instants and that wave heights significantly diverge. Nevertheless, wave impact average velocity, along the line defined by sensors 1, 4 and 7, has been evaluated equal to 1.9 m/s. The second wave height peak registered by channel 9 at around 4 s is associated to the first reflected wave and the one recorded at around 6 s is related to the main reflected wave.

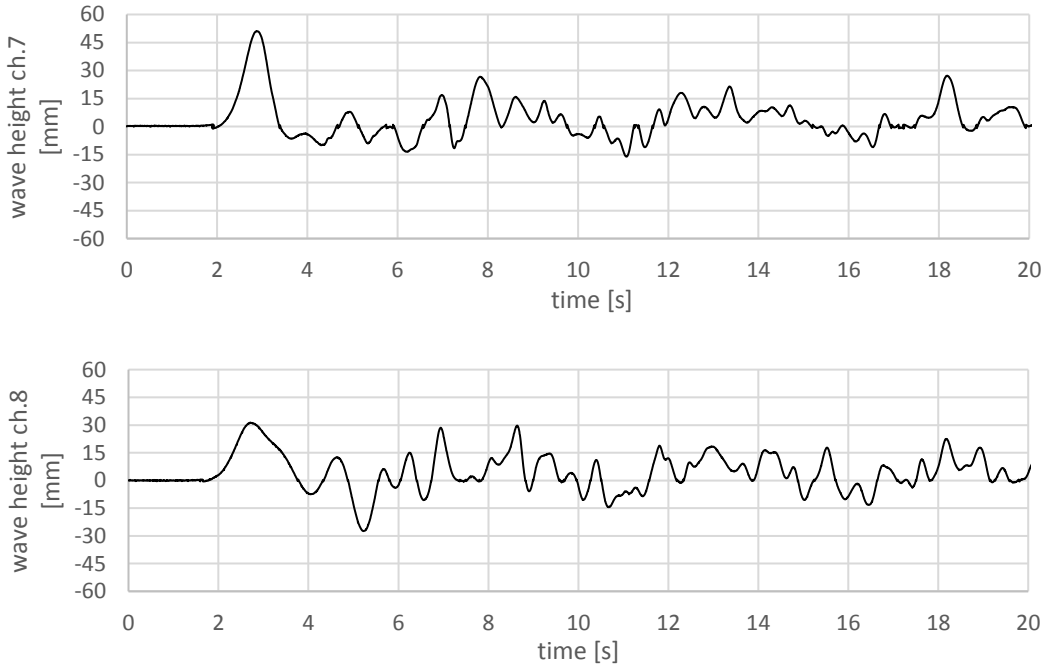

Figure 6.17a: wave height signals measured by sensors 7 and 8, which are in line with sensor 9 (trial 4.I_B).

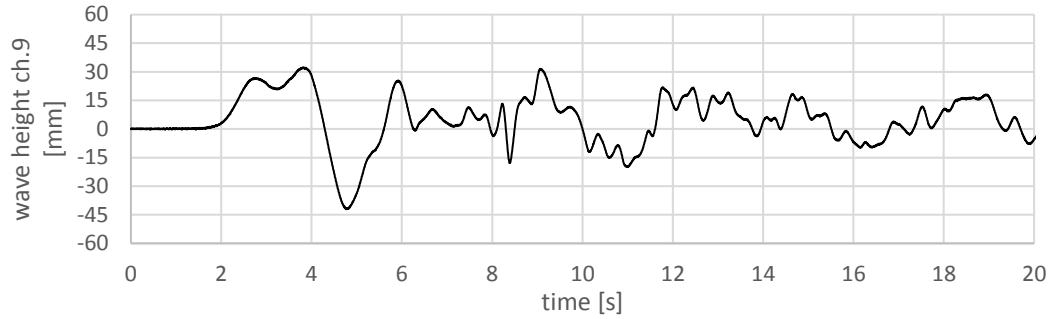

Figure 6.17b: wave height signal measured by sensor 9, which is in line with sensors 7 and 8 (trial 4.I_B).

6.2.3 Slide parameters influence on wave height

Slide impact velocity has not a relevant influence on wave propagation neither near the slide or near the dam. In both the models, wave height diagrams reveal an increase by about 5 mm caused by a slide impact velocity increment of 0.5 m/s. To show this behaviour, first and second starting positions are considered for Model A and first and third starting positions are taken into account for Model B (figure 6.18 and 6.19 respectively). This difference in wave height is mainly observable in the first two waves, however, the development of the following waves cannot be easily interpreted since they come out of reflected waves overlap.

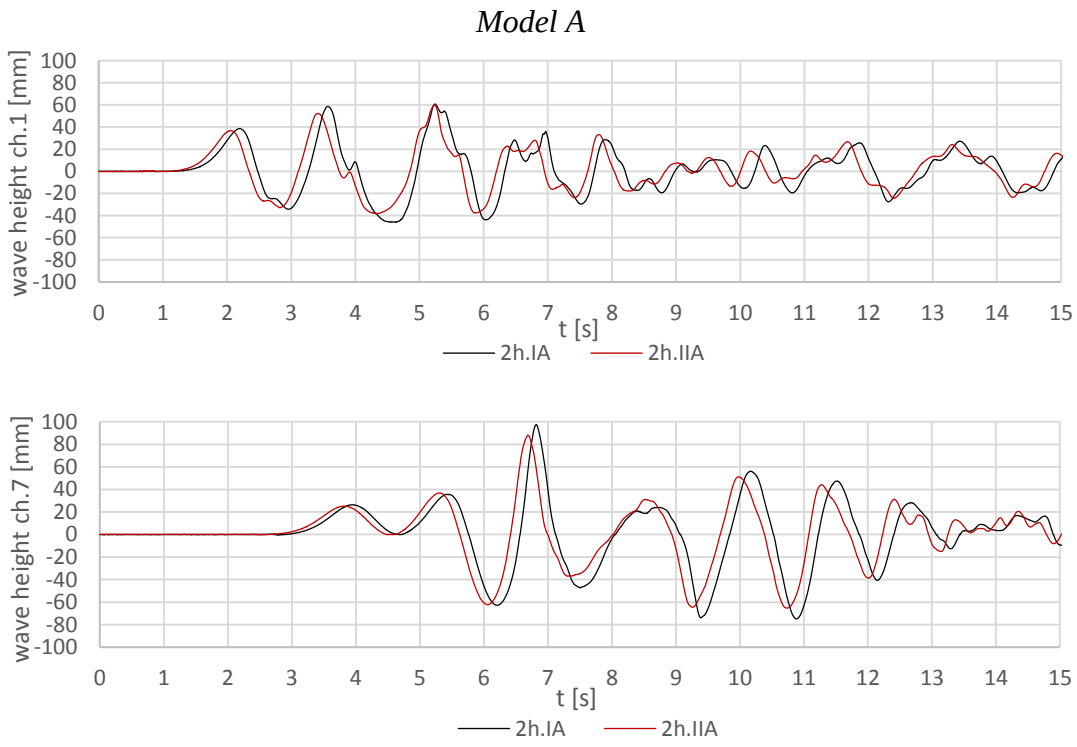

Figure 6.18: wave height signals measured in Model A by channel 1, close to the slide ramp, and by channel 7, close to the dam. Trials considered are 2h.I_A (Lc=15 cm) and 2h.II_A (Lc=65 cm).

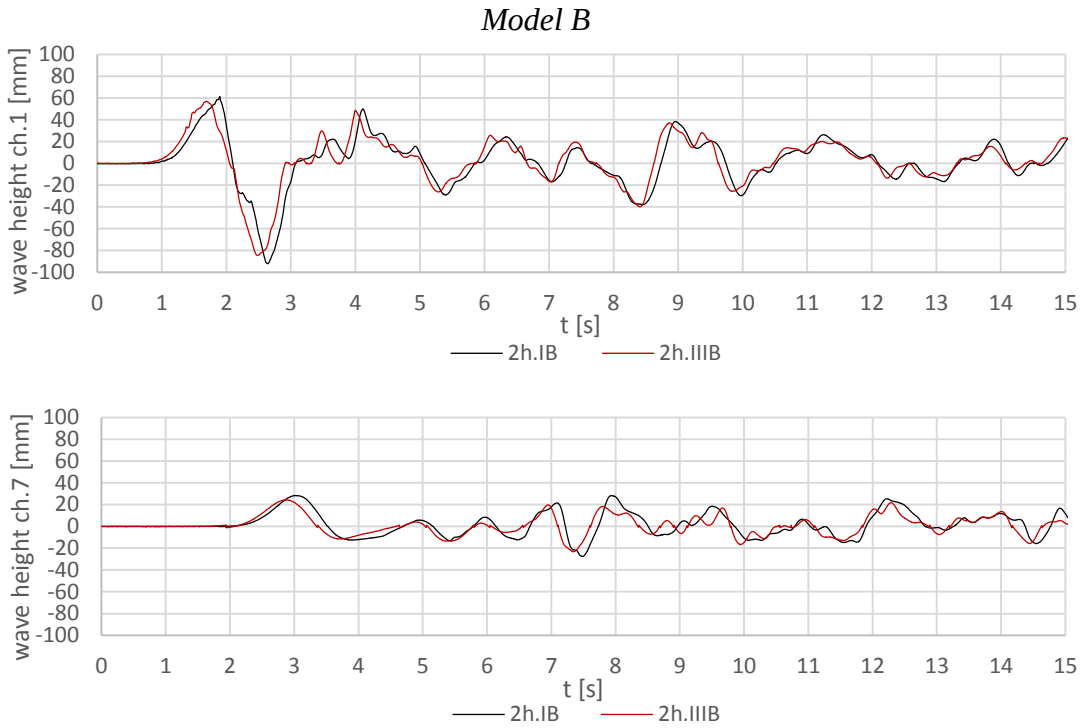

Figure 6.19: wave height signals measured in Model B by channel 1, close to the slide ramp, and by channel 7, close to the dam. Trials considered are 2h.I_B (Lc=130 cm) and 2h.III_B (Lc=178 cm).

To evaluate how the slide volume influences wave propagation in the basin, wave height signals have been grouped keeping slide barycentre height constant. Considering channel 1, located near the slide ramp, it is possible to see that a doubling of slide volume involves an incident wave height increase of at least 20 mm. In proximity to the dam, observing channel 7, this behaviour is still clear but damped. During the entire recording, waves generated by bigger slide volumes have higher height (see figures 6.20a, 6.20b and 6.21). What above said is identifiable in all trials performed on both models.

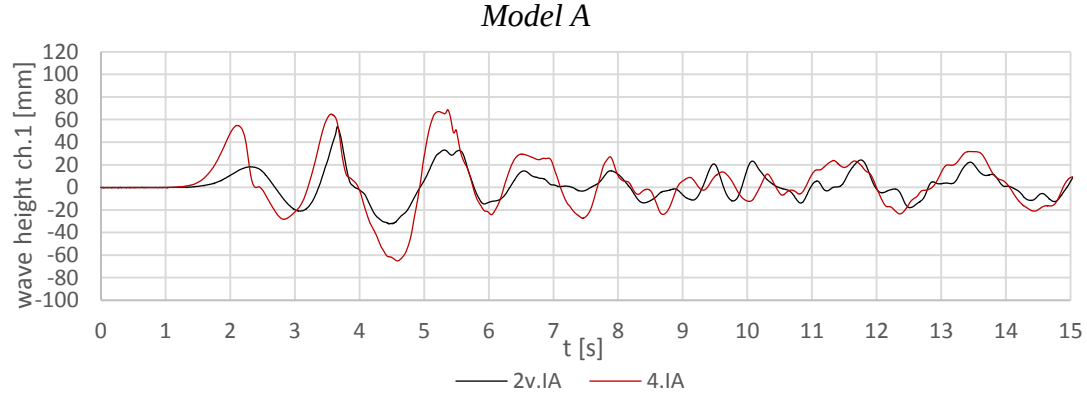

Figure 6.20a: wave height signals measured in Model A by channel 1, close to the slide ramp. Trials considered are 2v.I_A (Δb=243 cm) and 4.I_A (Δb=243 cm).

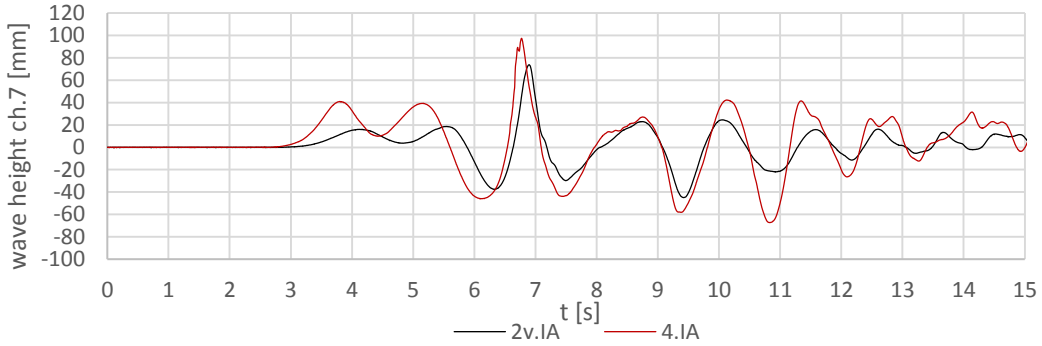

Figure 6.20b: wave height signals measured in Model A by channel 7, close to the dam. Trials considered are 2v.I_A (Δb=243 cm) and 4.I_A (Δb=243 cm).

Model B

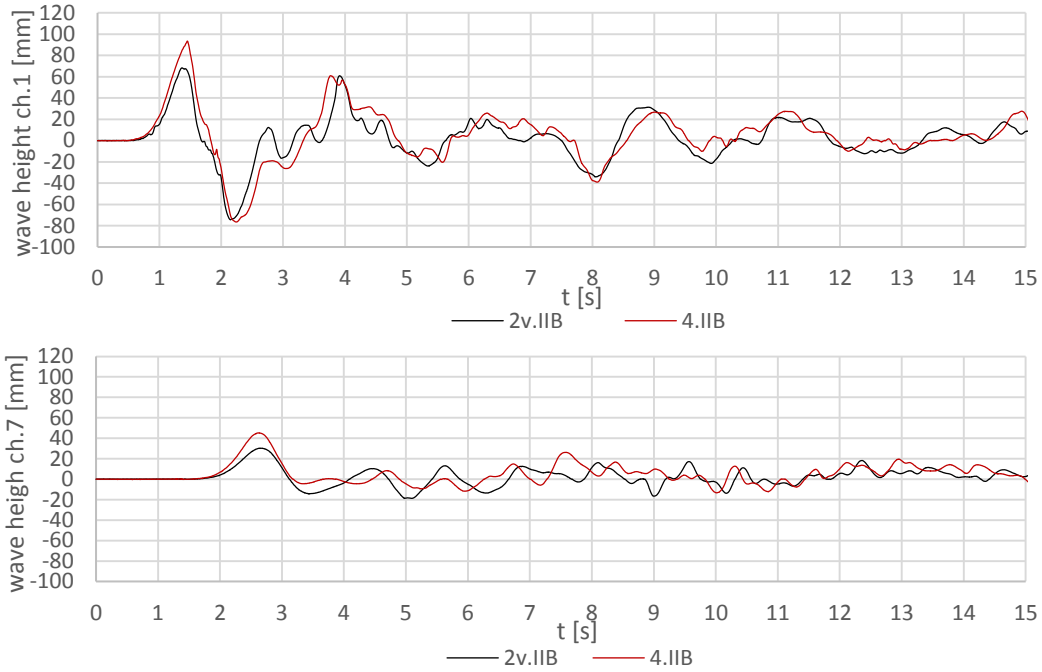

Figure 6.21: wave height signals measured in Model B by channel 1, close to the slide ramp, and channel 7, close to the dam. Trials considered are 2v.II_B (Δb=205 cm) and 4.II_B (Δb=205 cm).

The diagrams below show slide parameters effects on wave heights. Regarding the relation between slide impact velocity and wave height in figure 6.22, recurring data trends are not observable. However, trials with the same slide volume spread in a limited wave height range of the diagram. Furthermore, it can be assumed that an increase of wave height is not necessary ascribable to a slide impact velocity growth. Instead, figures 6.23 and 6.24 highlight a strong wave height dependence on slide volume: higher wave heights are due to bigger slide volumes. Moreover, the diagrams in figure 6.24, that describe the relation between slide shape ratio and incident wave height peak, show two different trendlines: wider slides (arrangements 2h, 4 and 6,

characterized by two columns of blocks) involve a faster growth of the incident wave height peak than cases with slide made up by only one column of blocks (arrangements 1, 2v and 3).

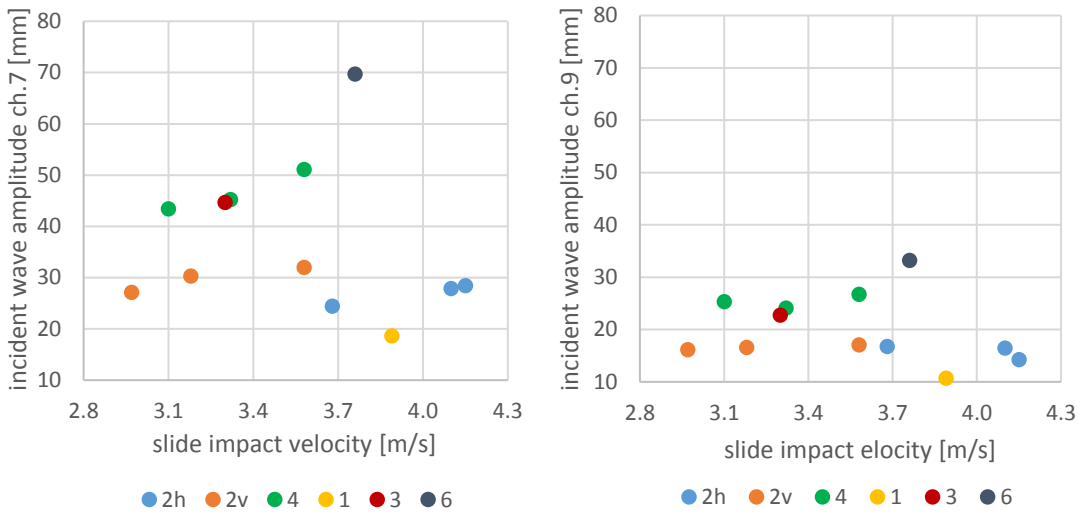

Figure 6.22: the diagrams show the relation between slide impact velocity and the maximum amplitude of incident wave in the basin. Channels considered are 7 and 9, both close to the dam. The slide impact velocity measurements are evaluated with a standard error of ±0.04 m/s, the incident wave peaks returned by channel 7 are evaluated with a standard error of ±1.6 mm and the incident wave peaks returned by channel 9 are evaluated with a standard error of ±0.4 mm. All trials arrangements of Model B are considered.

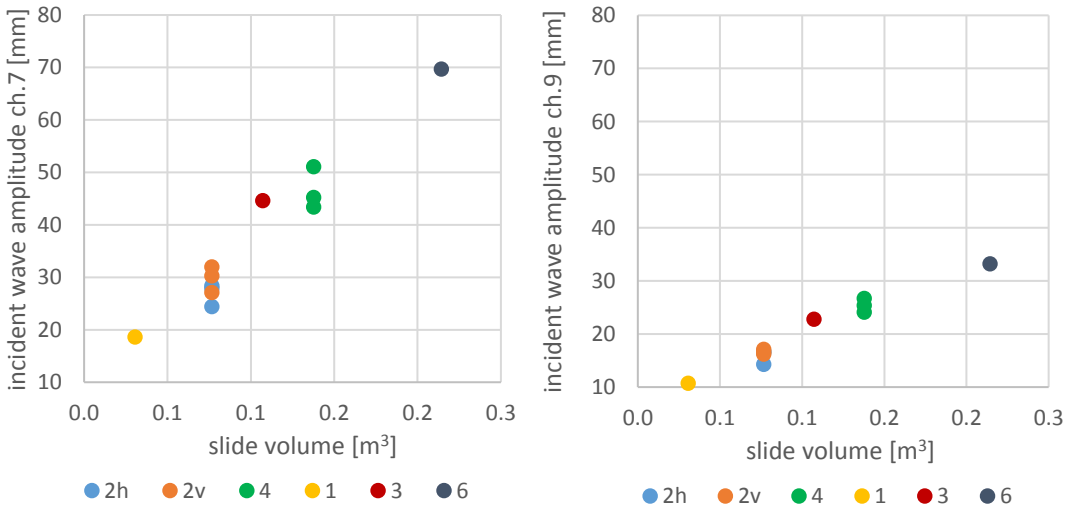

Figure 6.23: the diagrams show the relation between slide volume and the maximum amplitude of incident wave in the basin. The incident wave peaks returned by channel 7 are evaluated with a standard error of ±1.6 mm and the incident wave peaks returned by channel 9 are evaluated with a standard error of ±0.4 mm. Channels considered are 7 and 9, both close to the dam. All trials arrangements of Model B are considered.

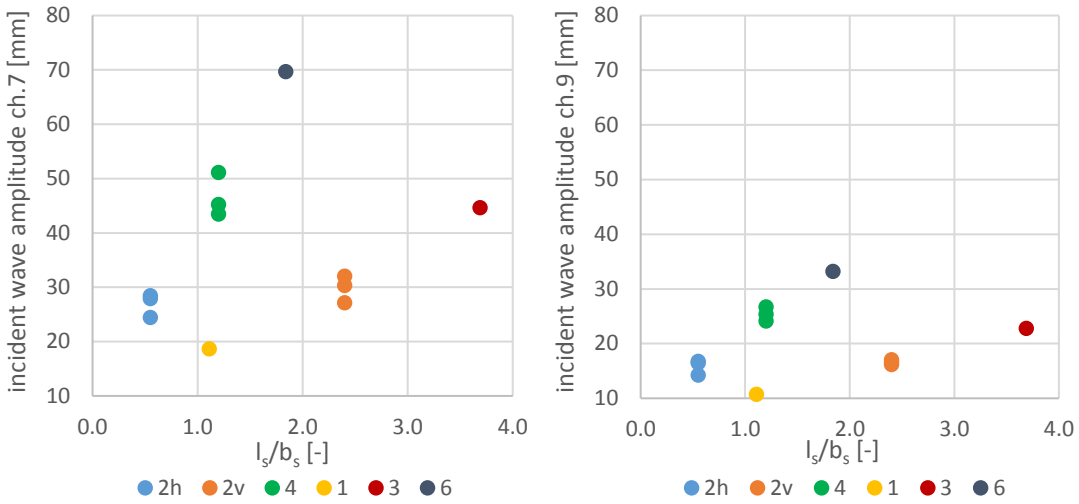

Figure 6.24: the diagrams show the relation between slide shape ratio and the maximum amplitude of incident wave in the basin. The incident wave peaks returned by channel 7 are evaluated with a standard error of ±1.6 mm and the incident wave peaks returned by channel 9 are evaluated with a standard error of ±0.4 mm. Channels considered are 7 and 9, both close to the dam. All trials arrangements of Model B are considered.

6.3 Run-up height analysis

The same Matlab code implemented for water propagation analysis has been applied also to study wave height run-up on the dam. The mesh grid has been extended by adding channels 12, 13 and 14 coordinates, in order to display the dam overtopping phenomenon. Signals returned by the three corresponding ultrasonic sensors describe wave height above dam top, which represents the zero level for run-up height signals. To make run-up height measure consistent with wave height signal, it has been necessary to define a common reference plane. The level of flat water in the basin has been chosen as the reference plane: for this purpose, the distance in height between the reference plane and the dam top has been added to run-up height values, complying with the fact that dam height at extremities is higher than at the centre. As a consequence, in figure 6.25, light green colour is associated to channels 12, 13 and 14 even if there is not a real water layer on the dam before slide falling.

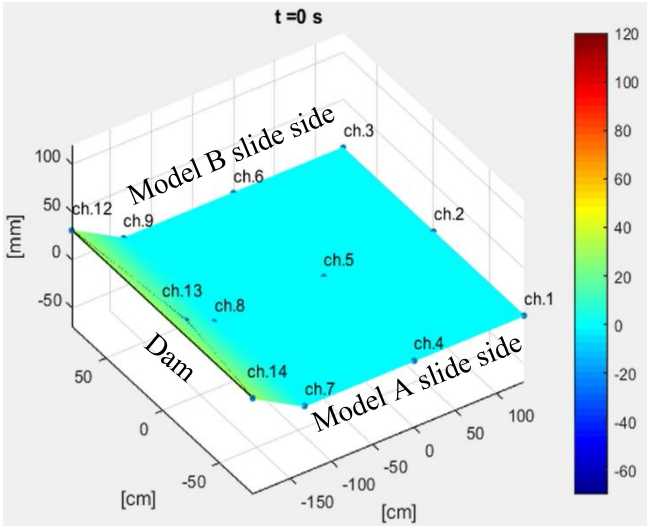

Figure 6.25: video screenshot of wave propagation and run-up phenomenon at time zero (before slide fall), with indication of slide position in Model A and Model B. Black line indicates the dam top.

6.3.1 Run-up height in Model A

As examples, video screenshots regarding the dam overtopping due to the incident and the first reflected waves are shown below, in figure 6.26; as in paragraph 6.2.1, the trial considered is characterized by a four blocks slide placed at first starting position on the ramp. Incident wave arrival in the dam proximity induces overtopping on the entire structure width, entailing the most dangerous situation. Otherwise, the highest run-up height occurs in channel 14 and it is caused by the main reflected wave that travels on the left basin side, considering wave propagation direction.

In Model A, four blocks slide arrangement involves the worst scenario in terms of overtopping water volumes, however the phenomenon takes place roughly in the same way also considering other slide configurations

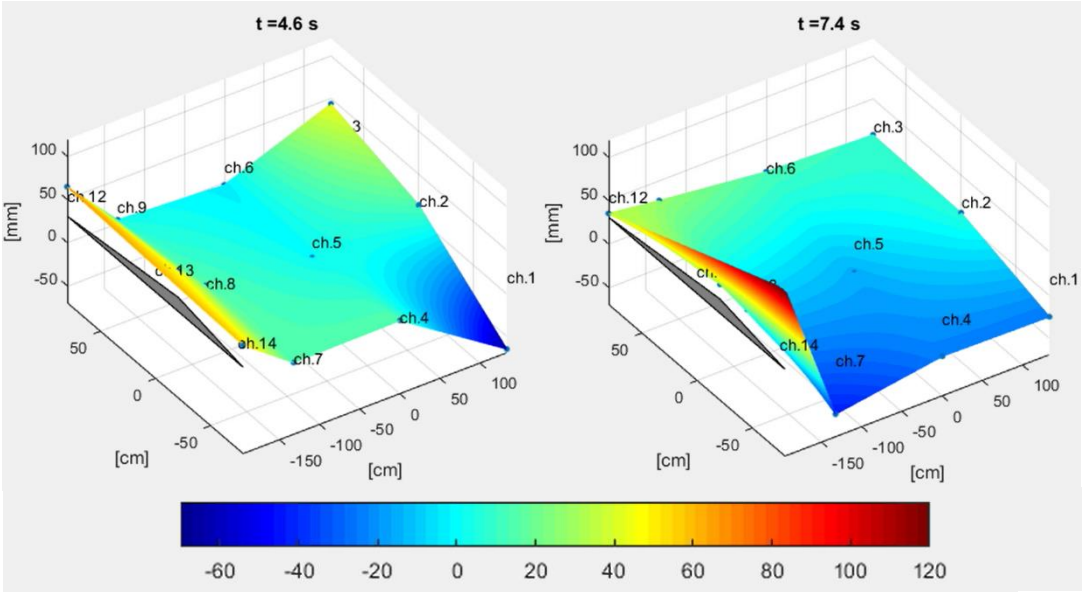

Figure 6.26: video screenshots at time 4.6 and 7.4 seconds illustrating dam overtopping caused by incident wave (on the left) and main reflected wave (on the right); trial 4.I_A.

Diagrams in figures 6.27, 6.28 and 6.29 describe run-up height variation in time; zero millimetres correspond to flat water level in the basin. Analysing signals detected by channels 12, 13 and 14, it may be inferred that incident wave overtopping occurs only in trials with 2h and 4 slide arrangements; in these cases, the one-dimensionality of the first wave is confirmed by a clear coincidence in time among channels 12, 13 and 14 recorded peaks. Actually, in trial 2h.I_A signal returned by channel 13 shows that run-up peak is not high enough to provoke overflow: incident wave run-up peak does not reach the dam extremities elevation, identified as threshold overtopping height.

Run-up highest peak is recorded by channel 14 and it is observable in all trials reported below. It is caused by the main reflected wave, which, only in trial 4.I_A entails also a considerable wave height raising in channel at the dam centre.

The influence of slide volume and impact velocity is confirmed by the phenomenon duration: taking into consideration all the overtopping waves generated during the tests, trial 2v.I_A overtopping takes 2.5 s, instead in experiments 2h.I_A and 4.I_A it takes 12 s and 12.5 s respectively. Indeed, cases with the same slide volume present very different overtopping duration but the highest run-up height peaks are always related to the biggest slide volumes.

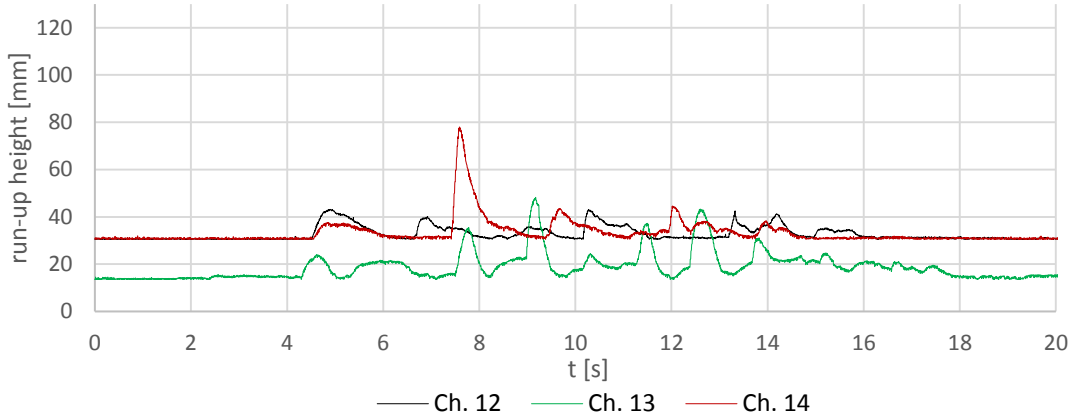

Figure 6.27: overlapping of run-up height signals (channels 12, 13, 14); trial 2h.I_A.

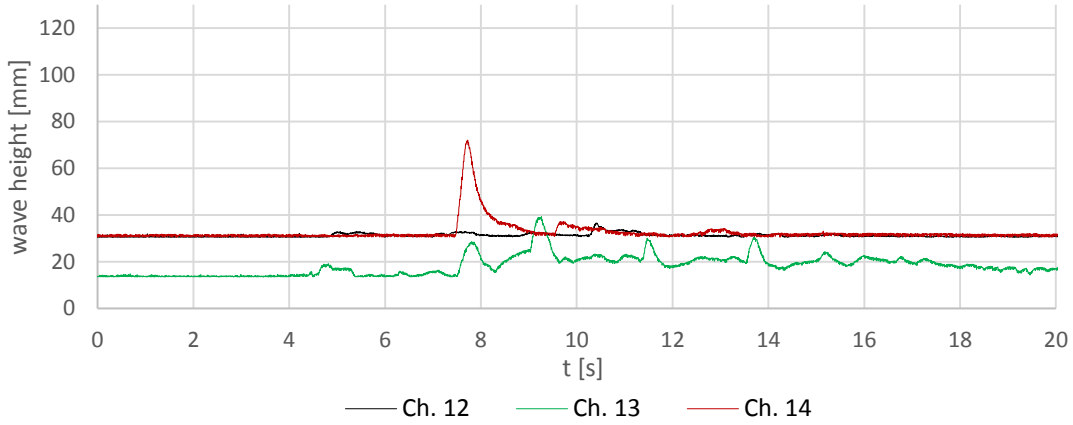

Figure 6.28: overlapping of run-up height signals (channels 12, 13, 14); trial 2v.I_A.

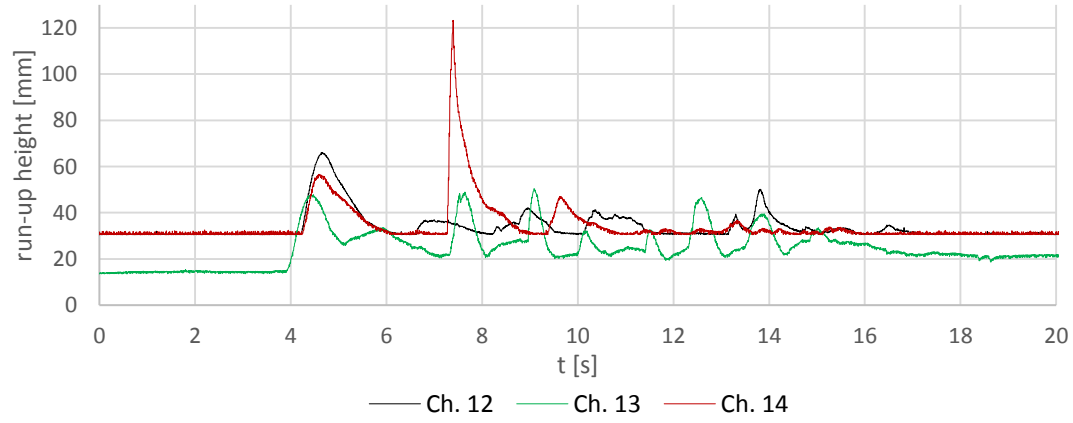

Figure 6.29: overlapping of run-up height signals (channels 12, 13, 14); trial 4.I_A.

6.3.2 Run-up height in Model B

For Model B, the video screenshots regarding run-up height variation in time are shown below in figures 6.30. In accordance with wave propagation analysis, trial 4.I_B is considered for demonstrating effects of main impulse waves on run-up height. Incident wave generates an overflow along the dam width, more marked in the proximity of channel 14. Arrival of the first reflected wave near the dam causes overtopping in channel 12, that partially overlaps the run-up due to the incident wave (see t=3.6 s on figure 6.30). This behaviour is confirmed by wave height signal returned by channel 9 (see figure 6.17b).

The main reflected wave, which travels in right basin side (considering wave propagation direction), brings a run-up height raising especially in correspondence of channel 12 (see t=6.6 s on figure 6.30).

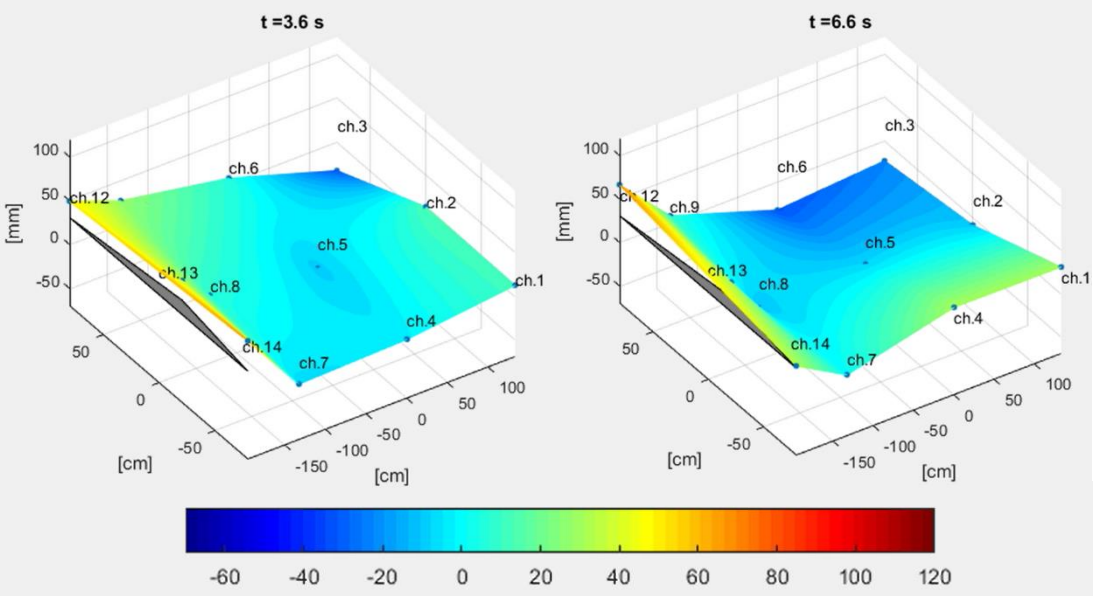

Figure 6.30: video screenshots at time 3.6 and 6.6 seconds illustrating dam overtopping caused by incident and first reflected waves (on the left) and main reflected wave (on the right); trial 4.I_B.

It is possible to observe an additional dam overtopping between the first overflow and the one caused by the main reflected wave (figure 6.31). The wave causing the second run-up height peak, recorded by channel 14, cannot be observed basing on wave propagation analysis. This overtopping event cannot be easily interpreted; its source probably is the same of the main reflected wave, associated to water hitting against basin side opposite to the ramp. This second reflected wave proceeds along left basin

side, considering wave propagation direction, causing dam overtopping although channels in the dam proximity do not record any wave height peak in previous seconds.

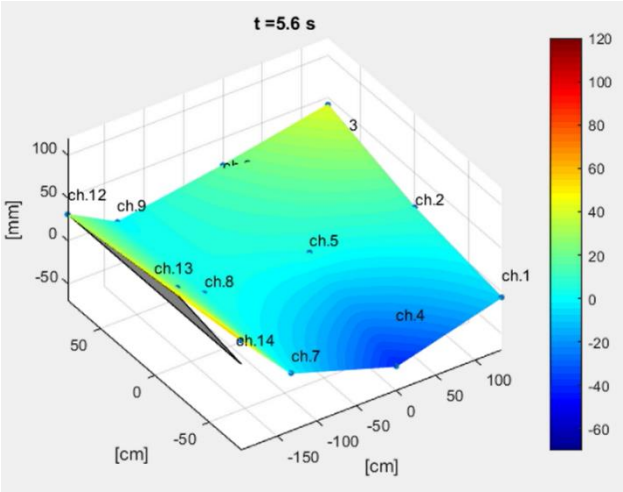

Figure 6.31: video screenshot illustrating second run-up height peak occurred in channel 14; trial 4.I_B.

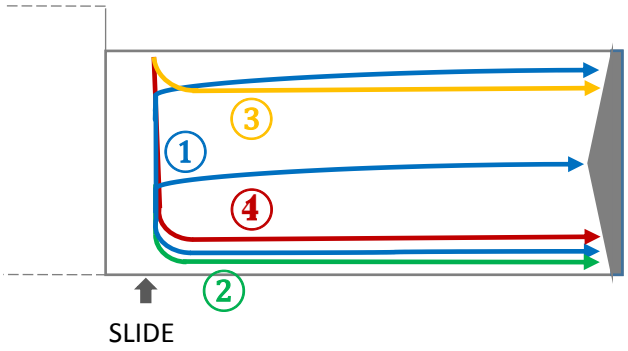

Figure 6.32: schematization of waves propagation in Model B, with the addition of second reflected wave description. Number 1 is referred to incident wave, number 2 is referred to the first reflected wave, number 3 is referred to the second reflected wave and number 4 is referred to the main reflected wave.

From diagrams below, showing run-up height's signal variation in time (figures from 6.33 to 6.39), it can be deduced that run-up height raising associated to incident wave is non-existent in 1.II_B signal; instead, it is recorded by channel 14 in cases 2h.II_B and 2v.II_B and by all three channels above the dam crest in tests 4.II_B, 3.IV_B and 6.IV_B. These last experiments confirm that overtopping phenomenon induced by incident wave occurs simultaneously but not uniformly, in terms of water heights, along the dam width.

As shown by all the diagrams below, at the exact moment the second run-up height peak (associated to the second reflected wave) decreases, the third one develops. The

latter is recorded by both channels 12 and 13 and it is generated by the main reflected wave.

Both slide volume and impact velocity influence run-up height signals: if these two parameters increase, run-up recorded peaks are higher. Instead, the overtopping phenomenon duration is different according to the slide volume.

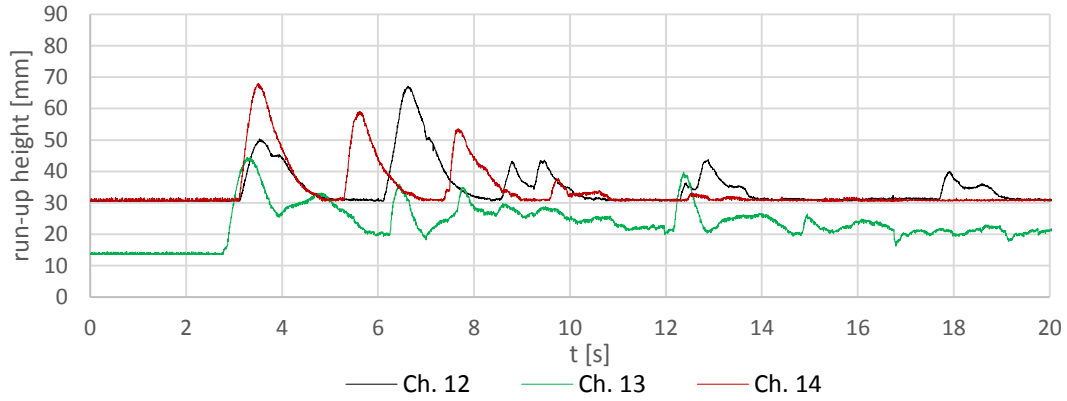

Figure 6.33: overlapping of run-up height signals (channels 12, 13 and 14); trial 4.I_B.

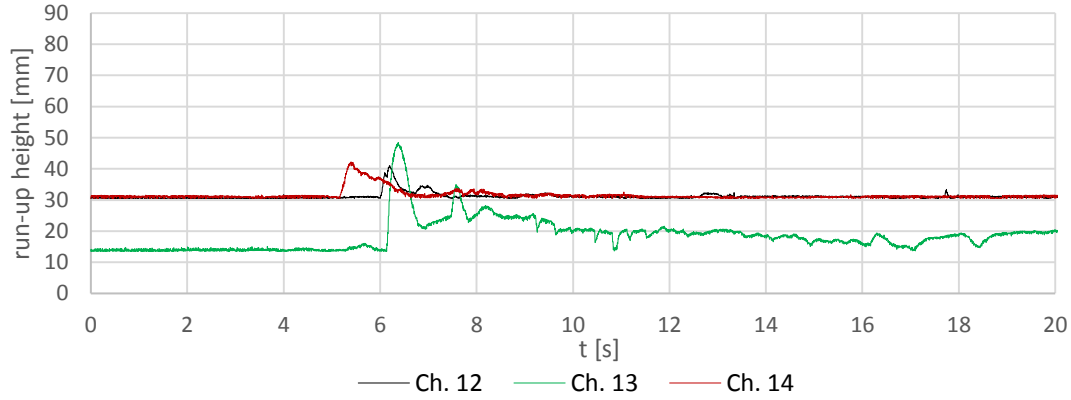

Figure 6.34: overlapping of run-up height signals (channels 12, 13 and 14); trial 1.II_B.

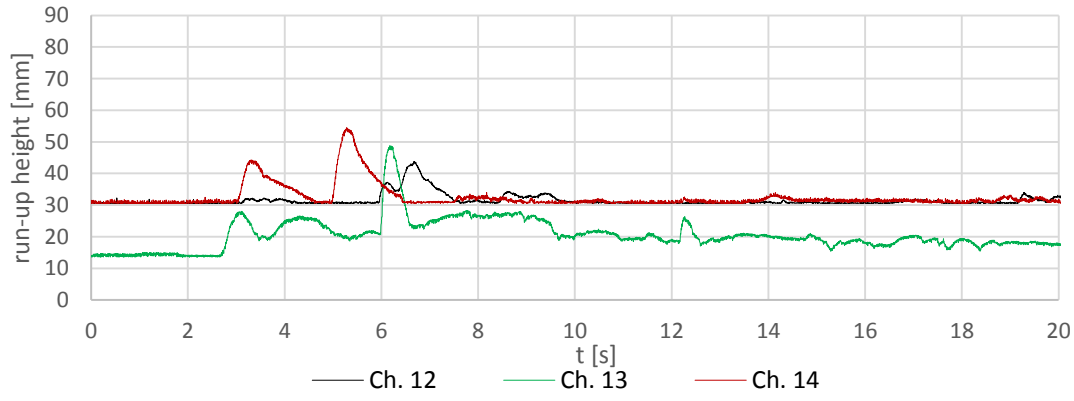

Figure 6.35: overlapping of run-up height signals (channels 12, 13 and 14); trial 2h.II_B.

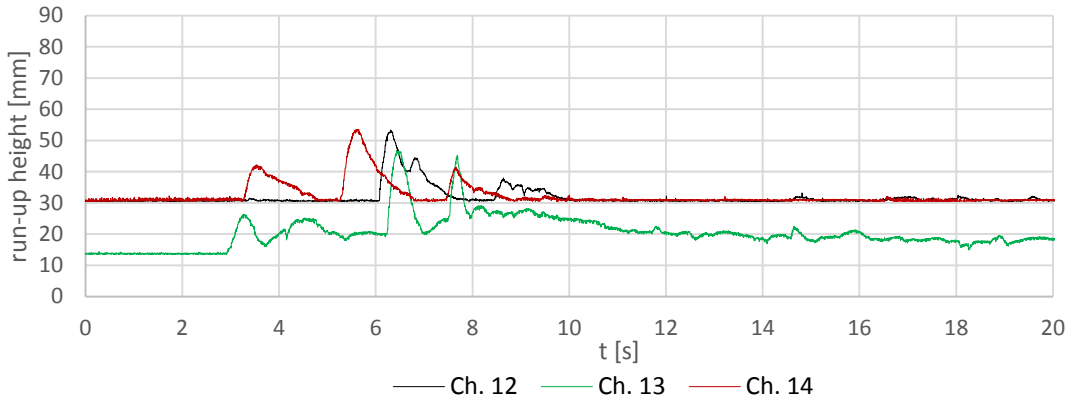

Figure 6.36: overlapping of run-up height signals (channels 12, 13 and 14); trial 2v.II$_B$.

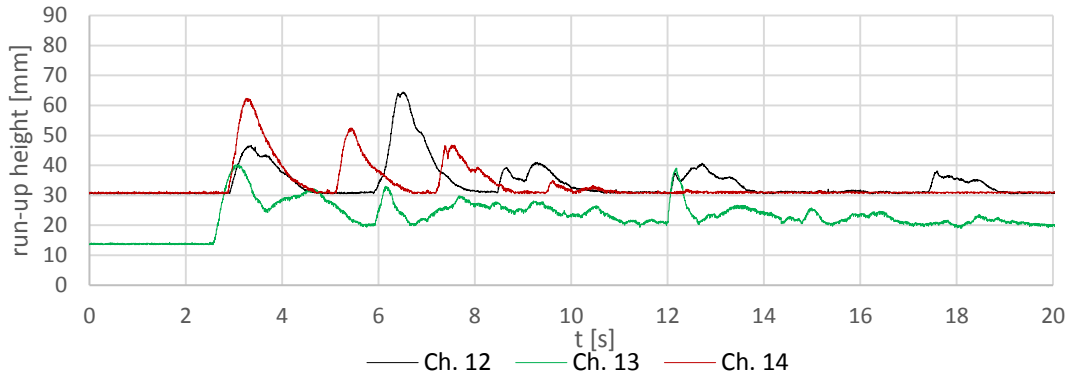

Figure 6.37: overlapping of run-up height signals (channels 12, 13 and 14); trial 4.II$_B$.

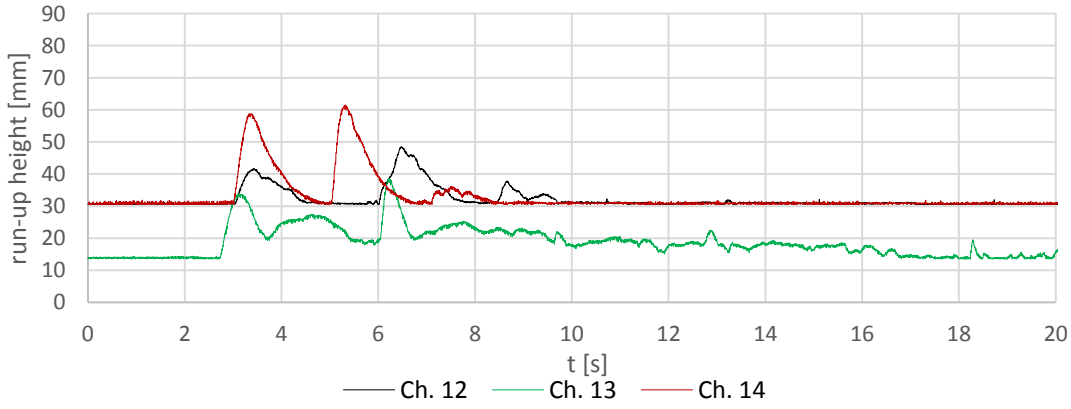

Figure 6.38: overlapping of run-up height signals (channels 12, 13 and 14); trial 3.IV$_B$.

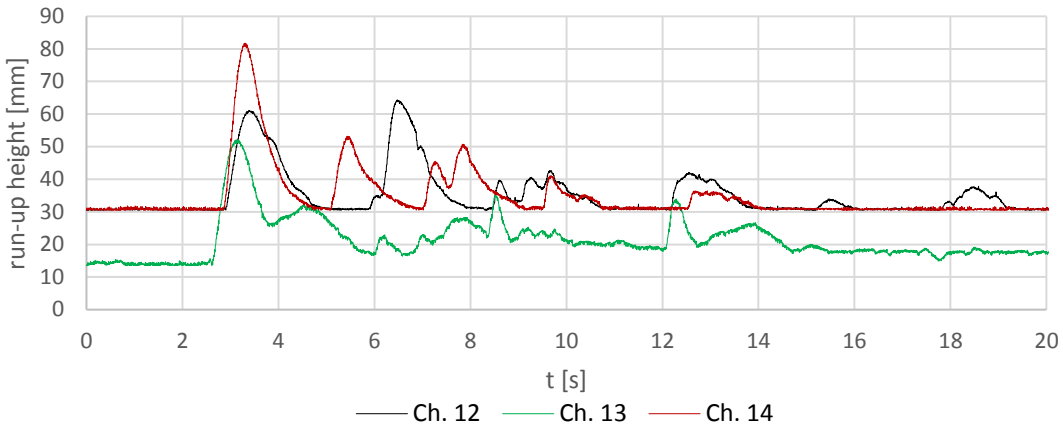

Figure 6.39: overlapping of run-up height signals (channels 12, 13 and 14); trial 6.IV$_B$.

6.4 Overtopped water volume analysis

Starting from the run-up height signals discussed in section 6.3, it is possible to evaluate the effect of main waves in terms of overtopped water volume.

The definition of the specific energy E [m] of a free surface flow is:

$$E = h + \frac{Q^2}{2gA^2} \qquad \textit{Equation 6.1}$$

Where h [m] is the water depth and $\frac{Q^2}{2gA^2}$ [m] is the velocity head. The flow area A [m] is defined as the product of a cross-section top width B [m] and the water depth h [m]; Q [m^3/s] is the discharge for given flow section area.

The specific energy is minimum when the water depth corresponds to the critical depth (k). Basing on the assumption that the height of the water in channels 12, 13 and 14 is equal to the critical depth, after setting the derivative of equation 6.1 with respect to h equal to zero, the outgoing discharge from the corresponding dam top segment can be calculated as:

$$Q_{ji} = \sqrt{k^3 \times B_i^2 \times g} \qquad \textit{Equation 6.2}$$

Where: Q_{ji} [m^3/s] is the instantaneous outgoing discharge from the i-dam top segment at the j-instant, k [m] is the critical depth measured by channels 12,13 and 14, B_i [m] is the width of the i-dam top segment and g [m/s^2] is the gravitational acceleration.

After the integration of the instantaneous discharge in time, it is possible to obtain the instantaneous overtopping water volume. Cumulating this last in time, the cumulative overtopping volume curve is obtained. The final value of this curve (estimated volume) should be equal to the overtopped volume measured in the buckets (measured volume). However, the estimated water volume diverges from the measured water volume; this means that water flow is not critical at the top of the dam. To make these two volumes equivalent, a multiplication factor has been introduced in the equation 6.2; it has been evaluated for each channel and trial. So that the final value of the cumulative water volume curve truly represents the total overtopping volume as collected in the buckets. This empirical procedure provides only a good representation of the relation between run-up height and overtopped volume. As it is possible to observe in the figures 6.40 and 6.41 below, we did not report the measurement of channel 13 because main waves especially reach the channels located at dam extremities.

In Model A, the wave that causes the greater outgoing water volume in channel 12 is the incident one (at t=4.6 s), instead, in channel 14, it is the main reflected one (at t=7.4 s). In general, the wave that principally causes dam overtopping is the main reflected one, arisen from model structural effect (protuberance in the basin side and step in the basin bottom).

In Model B, the more important overtopped water volume, in channel 12, is involved by the main reflected wave (at t=6.6 s), instead, in channel 14, by the incident wave (at t=3.6 s). In this case, because of the regular basin shape, the first wave, having the greatest amplitude, is the one that mainly contributes to generating water overtopping. See figures 6.11 and 6.32 for wave propagation illustration in Model A and B respectively.

Model A

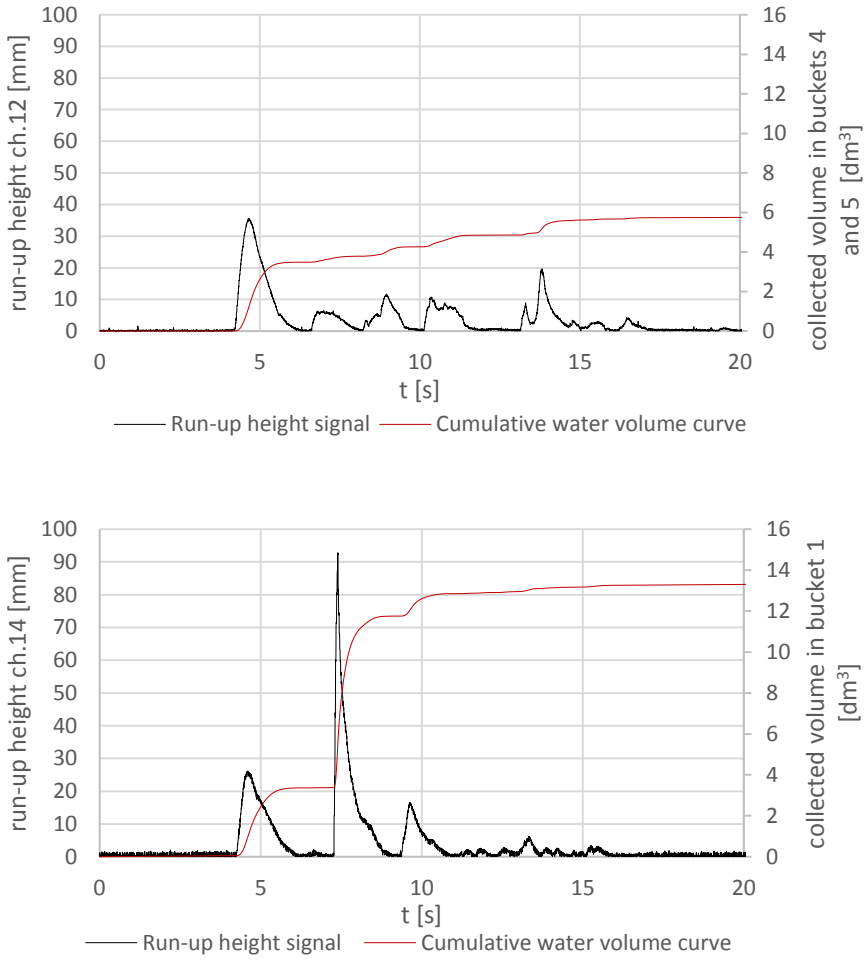

Figure 6.40: overlapping of the run-up height signal to the corresponding cumulative water volume curve in time. The first graph concerns channel 12 measurement, where the first run-up wave is due to the incident wave (t=4.6 s). The second graph concerns channel 14 measurement, where the first run-up wave is due to the incident wave (t=4.6 s) and the second one is due to the main reflected wave (t=7.4 s). The trial considered is 4.I_A.

Model B

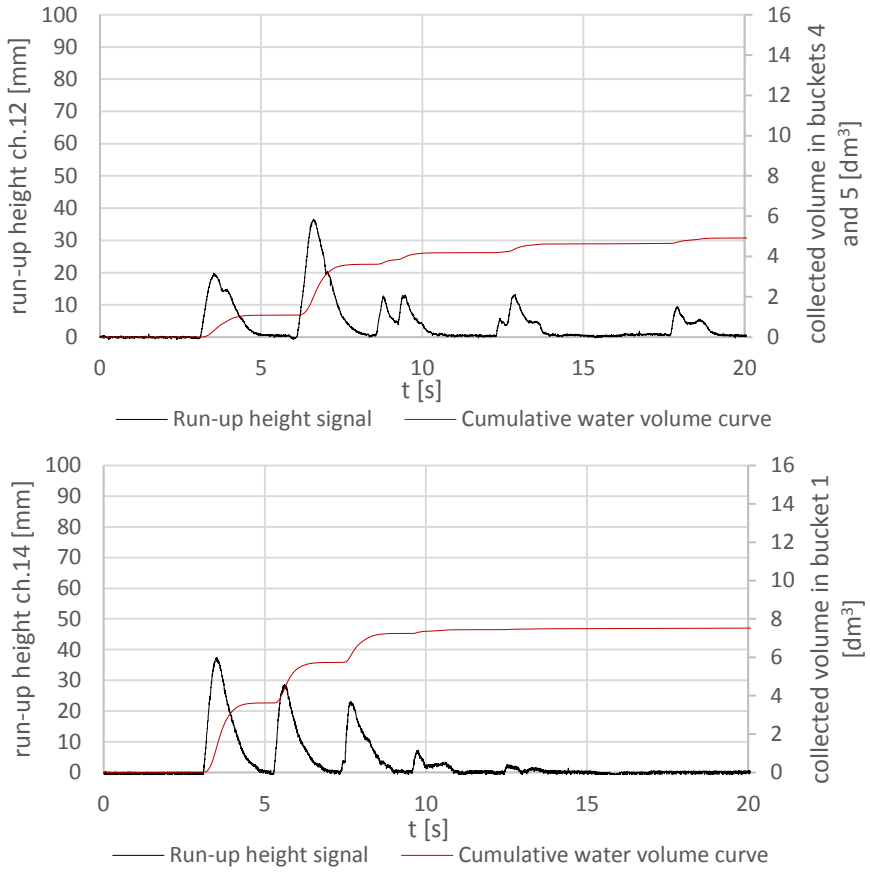

Figure 6.41: overlapping of the run-up height signal to the corresponding cumulative water volume curve in time. The first graph concerns channel 12 measurement, where the first run-up wave is due to the overlapping of incident and first reflected wave (t=3.6 s), the second run-up wave, instead, is due to the main reflected wave (at t=6.6s). The second graph concerns channel 14 measurement, where the first run-up wave is due to the incident wave (t=3.6 s) and the second one is due to the second reflected wave (t=5.6 s). The trial considered is 4.I_B.

The histograms illustrated below (figures 6.42 and 6.43) show the total overtopped volume measured in the trials performed on both models. The values reported are not associated to a specific test; they are the average of the overtopped water volumes obtained by several experiments with the same setup.

Focusing on the results, it is clear that overflows occurred in model A are greater than the ones observed in Model B, even if, the distance between the slide ramp and the dam location is shorter in the last case. It could be due to the fact that, in Model A, the waves mainly propagate towards the dam; on the contrary in Model B many reflections are caused by basin sides, implying waves energy dissipation. Moreover, the still water depth in the slide impact zone is higher in Model A, due to the presence of the step in the basin bottom, than in Model B. The waves height values, discussed previously in

sections 6.2 and 6.3, confirm this hypothesis; as a matter of fact, they are greater in Model A than in Model B.

Both diagrams show that the slide volume clearly influences overtopping phenomenon because larger overflows take place as this parameter increases. However, the slide impact velocity also affects overtopping; indeed, outgoing water volume is lower if slide starting position on the ramp is closer to water level in the basin. Considering trials with 2v and 2h arrangements, characterized by the same slide volumes but by very different slide impact velocities, it is possible to conclude that in Model A the slide impact velocity has a great influence on overtopped volume, instead, in Model B, the slide volume is the most influential parameter.

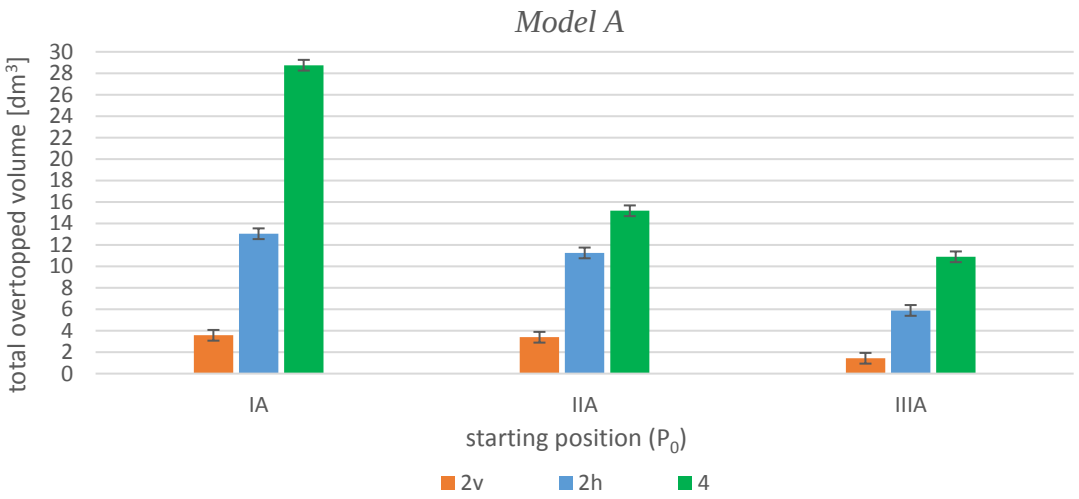

Figure 6.42: the histogram shows the average total overtopped water volume measured for all tests performed on Model A, considering a standard error of $\pm 0.5\ dm^3$.

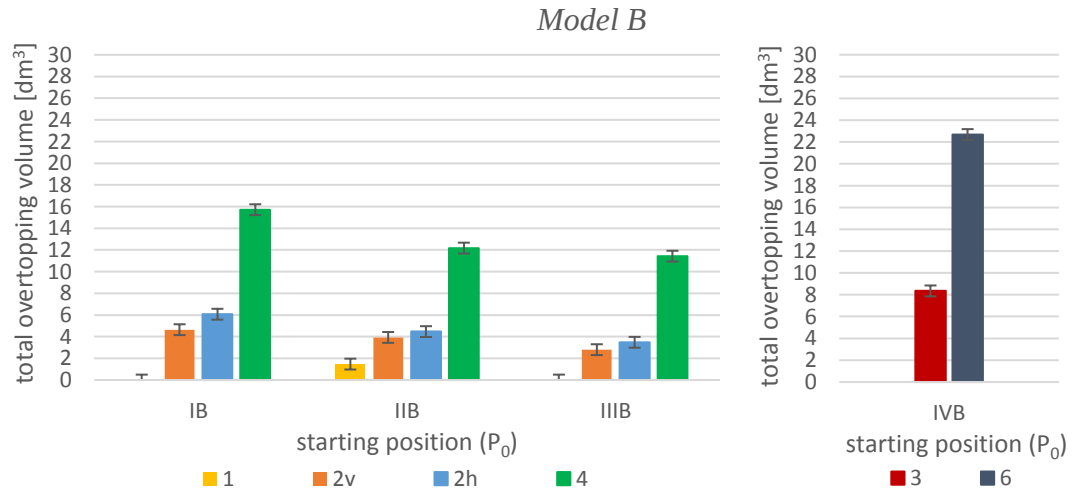

Figure 6.43: the histograms show the average total overtopped water volume measured for all tests performed on Model B, considering a standard error of $\pm 0.5\ dm^3$.

Diagrams in figures 6.44, 6.45 and 6.46 show the percentages of the total overtopping volume that cross one of the four segments on the dam top before being rerouted in pipes and then in the corresponding bucket; the water volumes collected in buckets 4 and 5 are both associated to the fourth dam top segment.

Analysing the histograms of each model, it is clear that the slide shape influences the dam overtopping modalities. In fact, the experiments with a slide composed by two columns of blocks (trials 2h, 4 and 6) show most dangerous overflows at dam extremities; instead, the cases identified by a higher shape ratio l_S/b_S (trials 2v and 3), are characterised by a quantity of overtopping water which decreases moving from channel 14 to 12, associated to segments 1 and 4 respectively (see figures 3.6 and 3.7). The tests with one block slide show an outgoing water volume differently redistributed along the dam width. Based on histograms information, it can therefore be concluded that in cases of wider slides both dam extremities are at risk; whereas, in cases of slides with a higher shape ratio the greatest danger affects the left dam side (i.e. on the side opposite to the slide ramp), corresponding to channel 14. This behaviour is specified by percentage values that recur almost equal in all the trials performed (see Appendix D "Influence of slide shape on dam overtopping modality in all the trials performed").

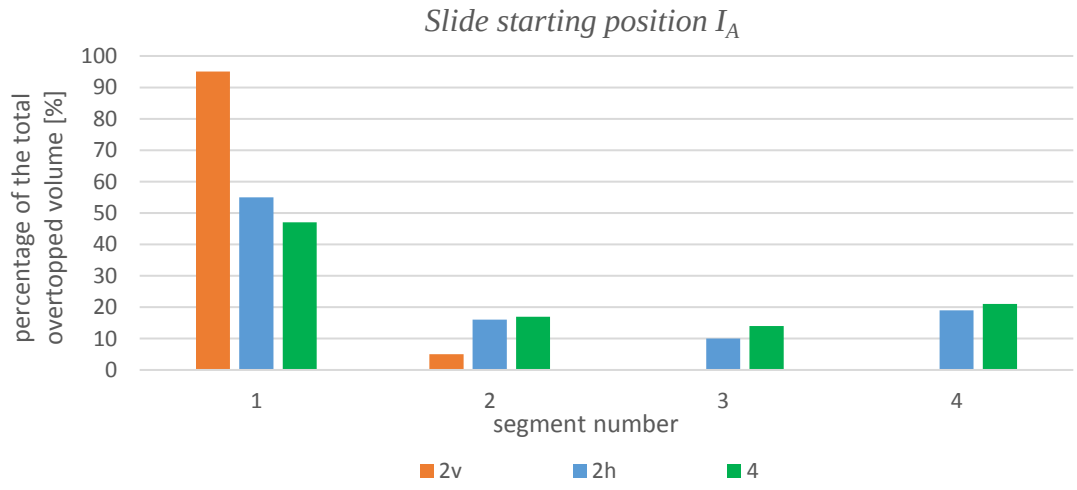

Figure 6.44: the diagram illustrates the percentages of the total overtopped volume measured in different buckets. Each of them is connected to one of the four specific segments of the channel where overtopped water from the dam is funnelled; trials considered are 2v.I_A, 2h.I_A and 4.I_A.

Figure 6.45: the diagram illustrates the percentages of the total overtopped volume measured in different buckets. Each of them is connected to one of the four specific segments of the channel where overtopped water from the dam is funnelled; trials considered are 1.II_B, 2v.II_B, 2h.II_B and 4.II_B.

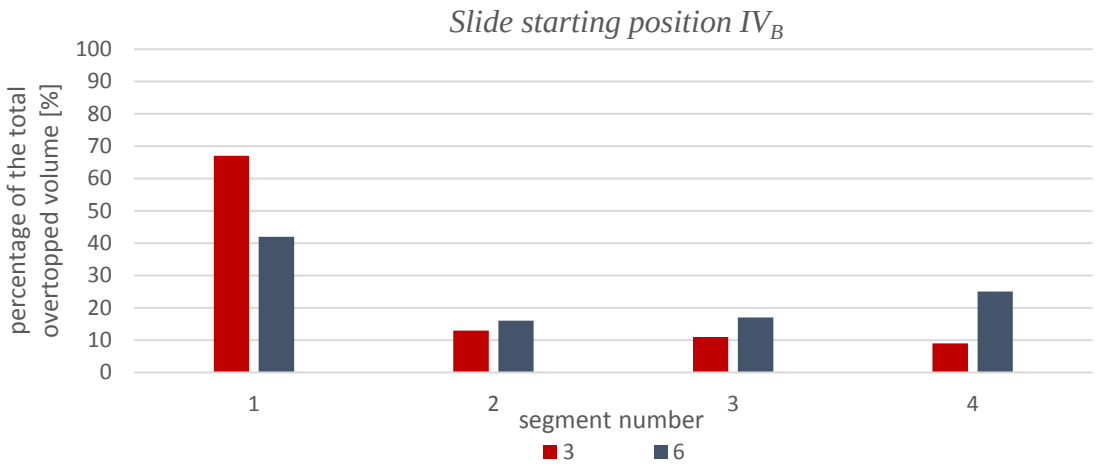

Figure 6.46: the diagram illustrates the percentages of the total overtopped volume measured in different buckets. Each of them is connected to one of the four specific segments of the channel where overtopped water from the dam is funnelled; trials considered are 3.IV_B and 6.IV_B.

The diagrams in figure 6.47 clearly explain slide impact velocity influence on overtopped water volume, even if this last increases mainly with slide volume. Cases 2v and 2h, characterized by the same slide volume and very different slide impact velocities, involve similar, but not identical, quantities of outgoing water. However, the highest values of overtopped water are always due to bigger slide volumes.

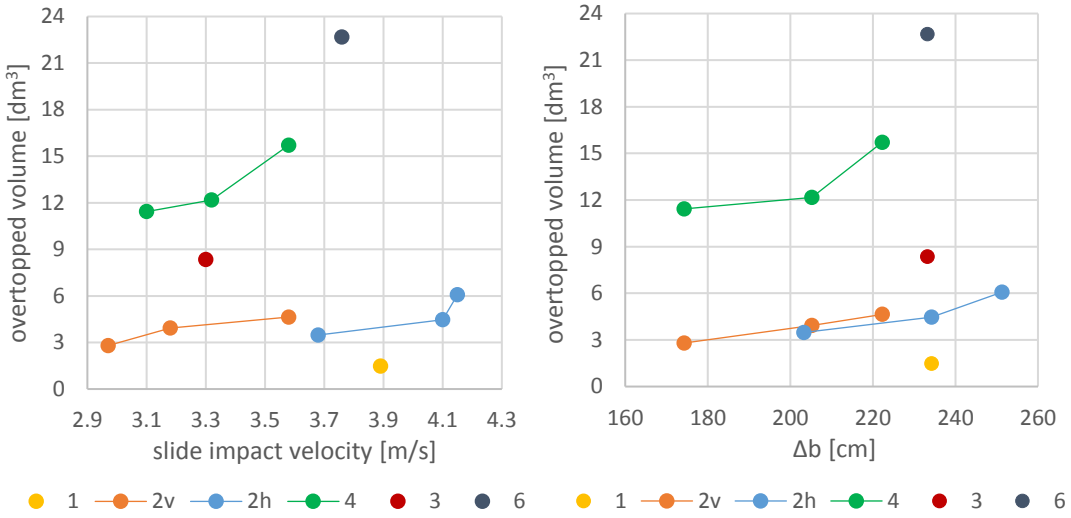

Figure 6.47: the diagrams show the influence of slide impact velocity and distance between slide centre of gravity and water level (Δb) on overtopped water volume. All trials performed on Model B are reporting, considering a constant freeboard of 2.4 cm.

The existent relation between slide volume and overtopped water quantity is explicitly shown in figure 6.48. Another important information which can be inferred from diagrams reported below is that a higher freeboard, associated to a lower water level in the basin, involves smaller overtopping volumes.

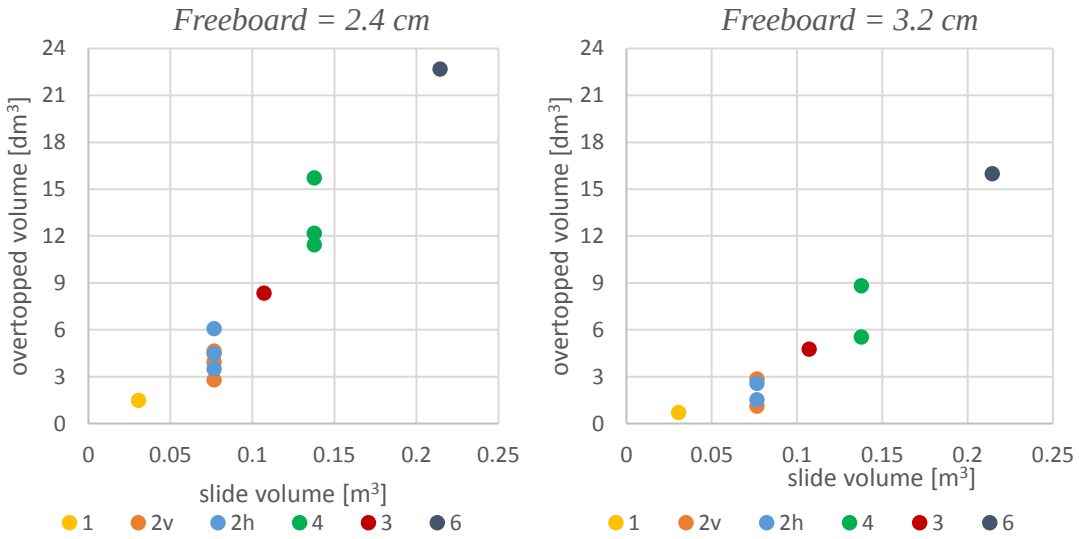

Figure 6.48: the diagrams show the influence of slide volume on overtopped water volume. All trials performed on Model B are reported, considering both freeboards investigated (2.4 cm and 3.2 cm).

Accordingly, it can be concluded that slide volume and freeboard are the two parameters which mostly condition the water overflow. Slide impact velocity influence, that is directly connected to slide shape, is minor but not negligible.

6.5 Dimensional analysis

The herein studied phenomenon is influenced by many different governing parameters, which are characteristics of the slide, the basin and the dam. To better analyse the effect of each parameter on the outputs, it is necessary to simplify the physical problem by applying a dimensional analysis. The *Buckingham's π-theorem* allows to reduce the number of relevant variables, providing a method for a general relation between the output and its influencing parameters. As this is a system defined only by mechanical quantities, three independent quantities are chosen to determine dimensionless groups Π_i which represent the parameters unit respect to the set of the three reference independent quantities. The main output considered is the overtopped water volume.

6.5.1 Evaluation of the impulse product parameter

A previous dimensional analysis, carried out to investigate subaerial generated impulse waves in a prismatic wave channel, has resulted in the definition of the impulse product parameter P (*Heller and Hager, 2010*). This dimensionless parameter is applied in empirical equations to estimate maximum wave height, maximum wave amplitude, wave period and wave height and amplitude decay. These equations were validated with 223 trials conducted on a 2D model, based on Froude similitude and granular slide material.

Heller and Hager defined several governing parameters affecting the general output (X) of the model:

$$X = f(h, W_s, b_s, s, d_g, \alpha, V_s, \rho_s, \rho_w, g, \mu, \sigma, x, t) \qquad \textit{Equation 6.3}$$

Where:

- h [m] is the stillwater depth in the slide impact zone;
- W_s [m^3] is the slide volume;
- b_s [m] is the slide width;
- s [m] is the slide thickness;
- d_g [m] is the slide grain diameter;
- α [°] is the slide impact angle;
- V_s [m s^{-1}] is the slide impact velocity;
- ρ_s [kg m^{-3}] is the bulk slide density;
- ρ_w [kg m^{-3}] is the water density;

- g [m s^{-2}] is the gravitational acceleration;
- μ [kg m^{-1} s^{-1}] is the viscosity;
- σ [kg m^{-1} s^{-2}] is the compressibility;
- x [m] is the distance from the point of impact;
- t [s] is the elapsed time.

The set of the three reference independent quantities chosen in Heller and Hager's study is composed by h, V_s and ρ_w. It is assumed that viscosity and compressibility have not a relevant influence on the outputs. Therefore, the seven governing dimensionless parameters identified are:

- Relative slide mass $M = \frac{m_s}{(\rho_w b_s h^2)}$;
- Relative slide thickness $S = \frac{s}{h}$;
- Relative grain diameter $D_g = \frac{d_g}{h}$;
- Slide impact angle α;
- Slide Froude number $Fr = \frac{V_s}{(gh)^{1/2}}$;
- Relative streamwise distance $X = \frac{x}{h}$;
- Relative time $T_r = t\left(\frac{g}{h}\right)^{1/2}$.

Where the slide mass m_s [kg] is the product of the slide volume (W_s) and the bulk slide density (ρ_s).

Consequently, the overtopping water volume W_W, which is considered the main model output, can be defined in dimensionless terms as:

$$\frac{W_w}{h^3} = f(1, M, S, D_g, \alpha, 1, 1, Fr, X, T_r) \qquad \textit{Equation 6.4}$$

In the evaluation of P, D_g is excluded because it was found to have a negligible effect on all impulse wave features in the data analysis. The parameters X and T_r were also not included in P because they are relevant only for wave propagation.

The impulse product parameter is related to the streamwise slide momentum flux component (*Zweifel et. al, 2006*) and is defined as:

$$P = FrS^{1/2}M^{1/4}\{\cos[(6/7)\alpha]\}^{1/2} \qquad \textit{Equation 6.5}$$

P consists only of basic slide parameters and water properties and may therefore be estimated prior to slide impact. It has an important role in both 2D and 3D calculation (*Heller et al.,2009*). In the present analysis, the impulse product parameter P is evaluated for all the trials performed.

Considering that the slide volume is an important affecting parameter, a further set of three reference independent quantities is investigated: W_s, V_s and ρ_w. Therefore, on the basis of the same assumptions of Heller and Hager, a new dimensionless parameter P^* can be obtained:

$$P^* = \left(\frac{V_s}{\sqrt{g W_s^{\frac{1}{3}}}}\right)\left(\frac{S}{W_s^{\frac{1}{3}}}\right)^{1/2}\left(\frac{\rho_s W_s^{\frac{2}{3}}}{\rho_w h b_s}\right)^{1/4}\{\cos[(6/7)\alpha]\}^{1/2} \qquad \textit{Equation 6.6}$$

The diagrams 6.49 and 6.50 illustrate the relation between P and W_w/h^3 (found using h, V_s and ρ_w as reference quantities) and between P^* and W_w/W_s (found using W_s, V_s and ρ_w as reference quantities) respectively. Analysing the diagrams on the semi-logarithmic scale, it is possible to notice a scattering of values of around one order of magnitude in both cases (see Appendix E "Diagrams P - W_w/h^3 and P^* - W_w/W_s on the semi-logarithmic scale"). In diagram 6.49 the points corresponding to trials conducted on Model A and Model B are completely separated because of the difference in slide impact angle and still water depth values. The same figure shows a growing trend in W_w/h^3 according to P: this behaviour is mainly due to the influence of slide volume on the impulse product parameter, as it can be observed in equation 6.5. In fact, the values located in the right upper quarter of the graph are related to the biggest slide volumes. In figure 6.50 it is impossible to recognize a trend but only a cloud of points is visible: the effect of slide volume is cancelled, since W_s is included in the set of three reference independent quantities, therefore residual effects of other parameters are plotted. Hence, both diagrams do not provide significant further information about the influence of parameters on the phenomenon analysed.

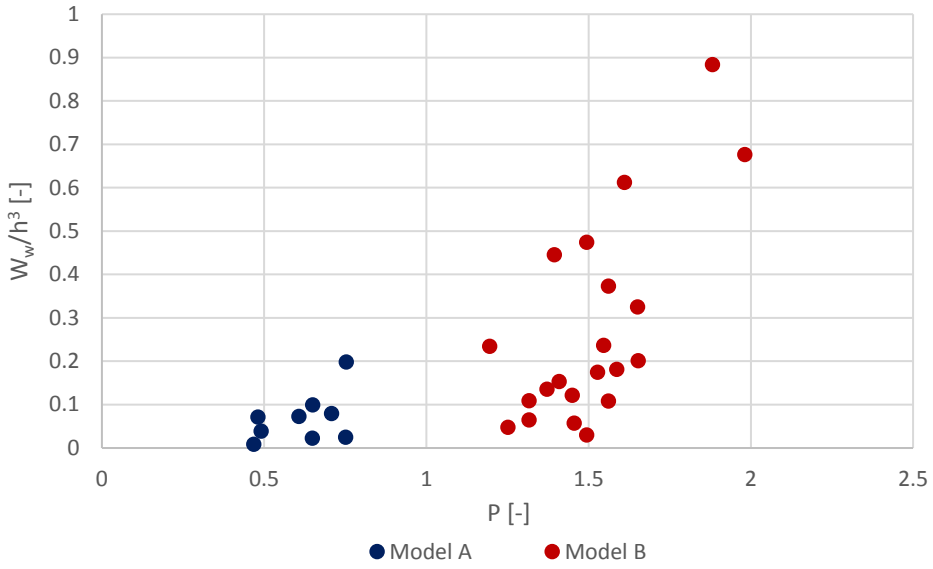

Figure 6.49: the diagram illustrates the relation between the impulse product parameter P and the dimensionless ratio W_w/h^3; the set of three reference independent quantities used is h, V_s and ρ_w.

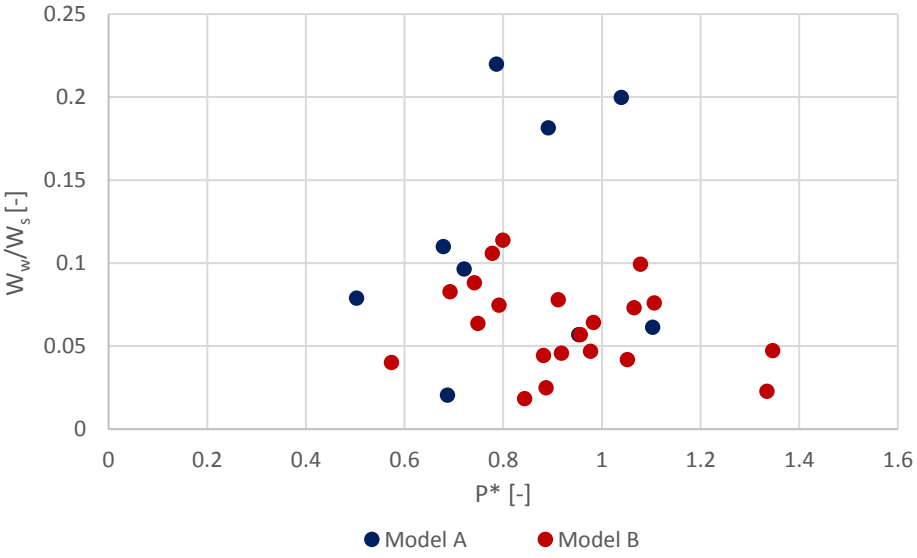

Figure 6.50: the diagram illustrates the relation between the dimensionless parameter P^* and the dimensionless ratio W_w/W_s; the set of three reference independent quantities used is W_s, V_s and ρ_w.

6.5.2 Dimensional analysis conducted on the studied physical model

The present study case is slightly different from the one investigated by Heller and Hager. The parameters that govern the main output W_w (the overtopped water volume) and therefore the propagation of landslide generated impulse waves and the process of dam overtopping, are listed in the equation 6.7.

$$W_w = f(h, f, W_s, b_s, l_s, \alpha,\ L_b, B_b, V_s, \rho_s, \rho_w, g, \mu, \sigma) \qquad \textit{Equation 6.7}$$

Where:

- h [m] is the stillwater depth in the slide impact zone;
- f [m] is the dam freeboard;
- W_s [m^3] is the slide volume;
- b_s [m] is the slide width;
- l_s [m] is the slide length;
- α [°] is the slide impact angle;
- L_b [m] is the length of the trapezoidal basin;
- B_b [m] is the width of the trapezoidal basin measured at the dam elevation;
- V_s [m s^{-1}] is the slide impact velocity;
- ρ_s [kg m^{-3}] is the bulk slide density;
- ρ_w [kg m^{-3}] is the water density;
- g [m s^{-2}] is the gravitational acceleration;
- μ [kg m^{-1} s^{-1}] is the viscosity;
- σ [kg m^{-1} s^{-2}] is the compressibility.

It is assumed that viscosity and compressibility have not a relevant influence on the outputs. In the 130 experiments conducted, the effects of the governing parameters α, L_b and B_b cannot be recognized: they are related to the model geometry and have different constant values in Model A and Model B. Moreover, the effect of ρ_s is not investigated in the present study case because, in all trials performed, the slide is made up by rigid blocks characterized by the same density.

The choice of primary dimensions is not unique but it is preferable to select the ones that for sure affect the dependent variable. For this reason, the chosen set of three reference independent quantities is composed by W_s, V_s and ρ_w. Neglecting those parameters that do not influence the main output in the present study case, equation 6.7 can be rewritten in terms of dimensionless values as:

$$\frac{W_w}{W_s} = f\left(\frac{h}{W_s^{\frac{1}{3}}}, \frac{f}{W_s^{\frac{1}{3}}}, 1, \frac{b_s}{W_s^{\frac{1}{3}}}, \frac{l_s}{W_s^{\frac{1}{3}}}, 1, 1, \frac{g{W_s}^{1/3}}{{V_s}^2}\right) \qquad \textit{Equation 6.8}$$

In Appendix F ("Results of the dimensional analysis which considers a set of three reference independent quantities composed by h, V_s and ρ_w") results obtained considering h, V_s and ρ_w as independent quantities are additionally reported to demonstrate the predominant influence of slide volume on the output.

Figures 6.51 and 6.52 show the relation between the dimensionless parameter $\frac{V_s^2}{gW_s^{1/3}}$ and the dimensionless output $\frac{W_w}{W_s}$, according to the variation of slide width and slide length, considering Model B and Model A respectively. The influence of slide width is visible looking at series 2v and 4, instead, the influence of slide length can be observed focusing on series 2h and 4. In both cases, the effects of slide dimensions on the main output are not significant: the variation of these parameters involves only smaller fluctuations in the normalised overtopped water volume.

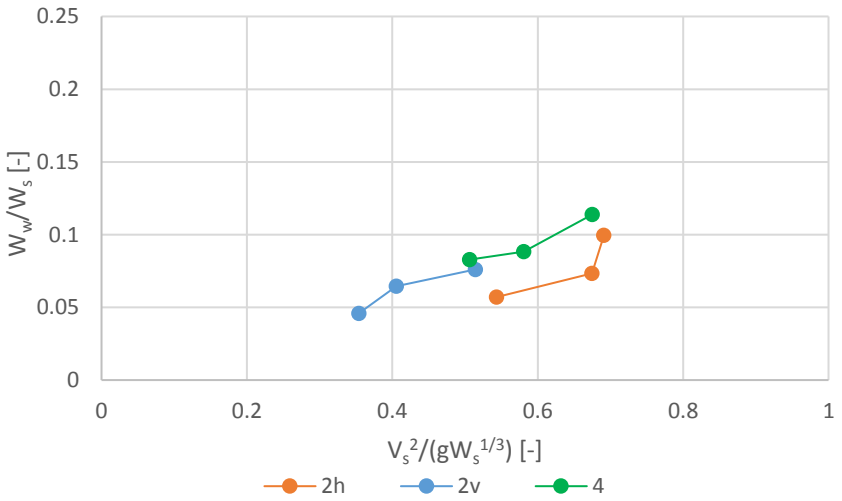

Figure 6.51: the diagram illustrates the influence of the dimensionless parameter $V_s^2/(gW_s^{1/3})$ on the dimensionless output W_w/W_s depending on slide width (2v and 4) and on slide length (2h and 4). Trials considered are conducted on Model B with the same dam freeboard (f=2.4 cm) and different slide starting positions on the ramp (I_B, II_B and III_B).

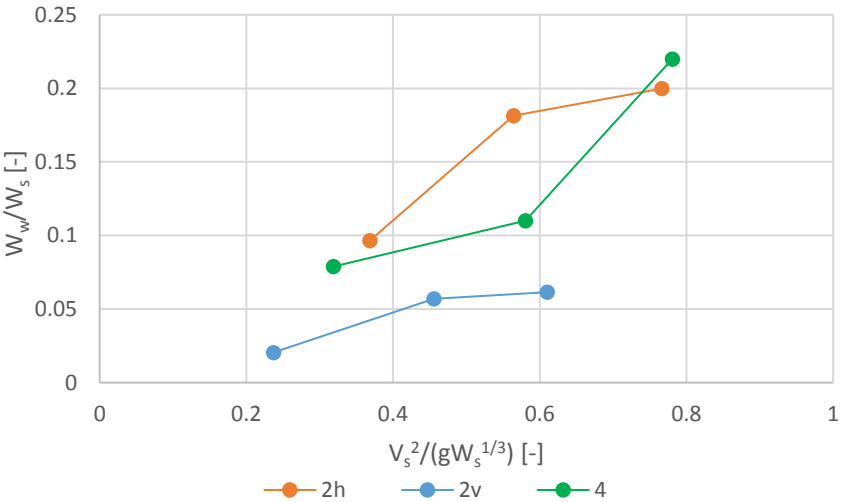

Figure 6.52: the diagram illustrates the influence of the dimensionless parameter $V_s^2/(gW_s^{1/3})$ on the dimensionless output W_w/W_s depending on slide width (2v and 4) and on slide length (2h and 4). Trials considered are conducted on Model A with the same dam freeboard (f=2.4 cm) and different slide starting positions on the ramp (I_A, II_A and III_A).

Figure 6.53 illustrates the relation between the dimensionless parameter $\frac{{V_s}^2}{g{W_s}^{1/3}}$ and the dimensionless output $\frac{W_w}{W_s}$, according to the dam freeboard variation in Model B. It is clear that the overtopped water volume is affected more significantly by the freeboard than by the slide dimensions. The cloud of points related to the lowest dam freeboard is always placed above the one associated to the highest dam freeboard.

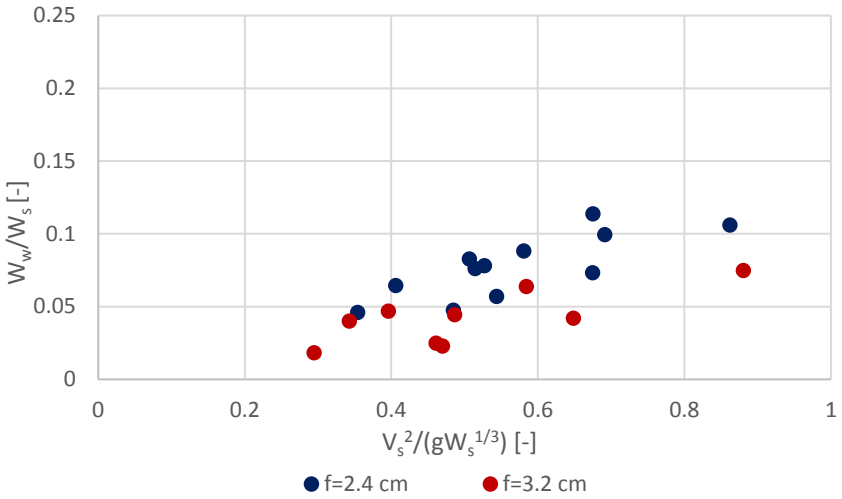

Figure 6.53: the diagram illustrates the influence of the dimensionless parameter $V_s^2/(gW_s^{1/3})$ on the dimensionless output W_w/W_s depending on dam freeboard (f=2.4 cm and f=3.2 cm). Trials considered are conducted on Model B with different slide volumes (1,2h,2v,4,3,6 blocks arrangements) at different starting positions on the ramp (I_B, II_B III_B and IV_B).

7. Conclusions and recommendations

The landslide generated waves in artificial reservoirs represent a hazardous phenomenon which may occur in many regions of the world and which can have disastrous consequences on the surrounding environment and on population. One of the best way to study this physical process is through laboratory simulations that could help in the prediction of the event characteristics.

This research focused on the assessment of the main parameters governing the phenomenon, firstly by observing the wave generation and propagation in the basin and secondly by analysing the gathered data. The experiments have been conducted by modifying the slide volume, its shape, its velocity and the dam freeboard. The influence of these parameters on the overtopping water volume (main output of the physical model), on the generated wave height and on the run-up height have thus been investigated. The analysis has been conducted on two models (Model A and Model B) that differ in location and impact angle of the slide as well as in still water depth in the slide impact zone. In Model A the slide is located on the left side of the basin, whereas, in Model B it is aligned with the right basin side and is closer to the dam.

The wave propagation in the trapezoidal basin and the consequent wave run-up at the dam crest were simulated using a Matlab code from the collected data, for a qualitative evaluation of the phenomena. The outgoing discharge at dam top segments was estimated using a formula calibrated to correspond to the overtopping volume collected and measured in the buckets. In this way, the relationship between the run-up height signal and the cumulative water volume has been studied.

Basing on these analyses, a comparison between the propagation and overtopping patterns of Model A and Model B has been performed, identifying potential model effects.

The data analysis on Model A indicated that the slide falling generates a one-dimensional wave extended throughout the basin width, with a slightly higher

amplitude in the right basin side. Besides, the wave that mostly causes dam overtopping occurs just a few seconds after the incident one. It arises both from the interference between various generated waves and from the model structural effects. The last being due to a protuberance in the basin side and to a step in the basin bottom. The wave propagation analysis in Model B was found to be more complex as in addition to the incident wave, several minor waves were generated by ongoing reflections in the basin. The incident wave, due to its greatest amplitude, is the one that generates the highest wave run-up on the entire throughout dam width, though a slightly higher run-up has been observed on the left basin side.

The influence of the slide volume, the slide impact velocity and the slide shape on wave height and run-up height was investigated. In both models, the slide volume proved to have significant effects on the generated wave amplitude and on the run-up height. A minor influence due to the slide impact velocity was also detected. In general, as these two parameters increase, the overtopping phenomenon duration is longer and the peaks of run-up height are greater. Instead, the slide shape influence on the wave propagation and the wave run-up is not clearly visible.

Observing the quantities of outgoing water through histograms, it can be concluded that the overtopped water volume is bigger in Model A than in Model B. A comparison of the results should consider that Model A has a higher still water depth in the slide impact zone, fewer reflections in the basin involving lower wave energy dissipation, as well as structural effects potentially increasing the wave height. Moreover, considering both Model A and Model B, the total overtopped volume distribution along the dam crest is influenced by the slide shape. Taking into account the water collected in the buckets from each defined segment of the dam, it has been observed that when slides are wider than longer, the greatest risk of overtopping occurs at both dam extremities, whereas, if not, the biggest outflows take place on the left dam side.

To determine the influence of the different phenomenon governing parameters on the overtopped water volume, a dimensional analysis has been applied. It reveals that the impulse product parameter (P) as defined by Heller and Hager (*Heller and Hager, 2010*) does not apply directly for consideration of overtopping volume. Therefore, a new dimensionless parameter (P^*) has been defined, using a set of three reference

independent quantities that includes slide volume. Thus, the effect of this parameter is removed leaving only residual effects of other parameters. However, P^* does not consider the effect of freeboard and does not make clear the minor influence of other parameters on the output. This indicates that there is a need for performing a new dimensional analysis, basing on the studied physical model. Observing the relations between the dimensionless overtopping output and the dimensionless groups, which are related to the governing variables, the influence of each governing parameter on the output is well discernible. As stated by this last dimensional analysis, the slide volume clearly plays the most important role. In fact, an increase in the slide volume results in a growth of the overtopping water volume regardless of the values of the other governing parameters. In addition, the slide impact velocity, which in turn is affected by the slide dimensions, proves to have a relevant effect on the overtopping water volume. The total overtopped water volume is less affected by slide length and width, instead, the dam freeboard shows to be particularly relevant in outflows generation.

We suggest future experiments to be carried out with a different slide ramp structure thus allowing to study the effects of a wider range of slide impact velocity values. We also recommend to deploy a different dam design, as the Chevron dam used in the present research showed many structural defects which had to be accounted for in the analysis. Furthermore, for wider application possibilities of a dimensional analysis, it is suggestible to investigate the consequences of the variation of the slide impact angle, the basin length and the basin width on the overtopped water volume.

Appendix A

Calibration procedure applied to obtain overtopping volume measurements

The overtopped water, collected in buckets, is measured using an ultrasonic sensor. This instrument returns the distance between the bucket top, where the sensor itself is manually placed, and the water level inside the bucket in millimetres.

To obtain a water volume, it is necessary to estimate a calibration factor. With this purpose, the same measuring procedure has been repeated many times: at first the empty bucket measure is registered, then 1 l of water is poured in the bucket and the resulting measurement is read on the sensor display. The bucket is progressively refilled with 1 l of water for eight times, without emptying, and the related water height measure is observed. The bucket filling is done using a graduated cylinder accurate to millimetres. This entire procedure has been repeated four times in order to obtain results with a good repeatability, as it is shown in the diagram below.

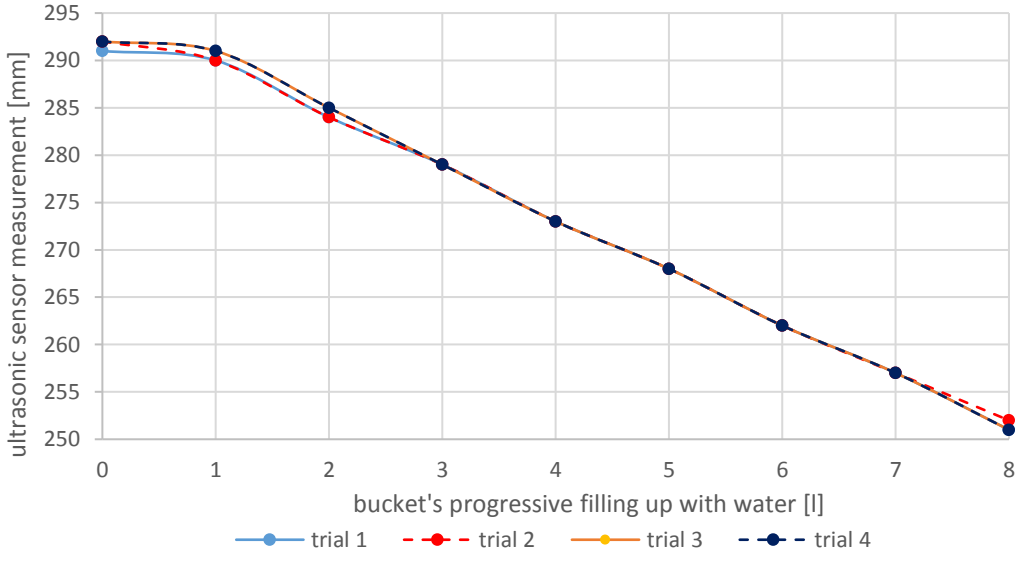

Figure A.1: the diagram shows experimental curves, related to four different trials, obtained by applying eight times the same procedure of bucket progressive refilling with 1 l of water.

Considering Figure A.1, it is clear that the highest uncertainty which affects curves corresponds to their upper part, when the bucket is totally empty and when it contains only 1 l of water. Instead, the remainder part of the curve fits well enough in the four cases studied. To solve this problem, that is due to the irregular shape of the buckets bottom, it is opportune to refill the buckets with 1 l of water before each test.

To estimate the calibration factor, the linear trend line of each curve is plotted and the associated equation is also shown.

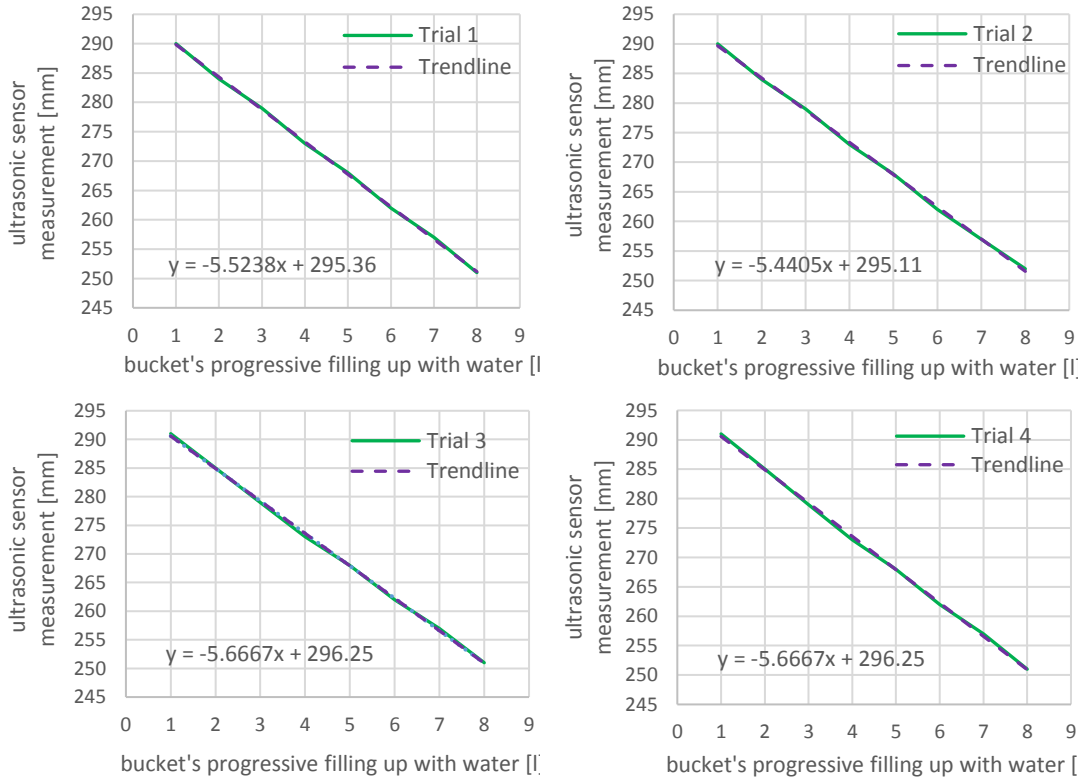

Figure A.2: the curves show the ultrasonic sensor measure during the progressive water refilling of buckets, with their associated trend lines, considering the four trials performed. The upper part of curves is excluded because it is opportune that each bucket is already filled with 1 l of water before each test.

The absolute slope of the trend line is an indicator of the water height variation caused by the progressive buckets filling.

Table A.1: trend line equation of curves illustrated in figure A.2, obtained in each trial performed.

	Polynomial trendline equation	
Trial	$\boldsymbol{y = ax + b}$	$\boldsymbol{\lvert a \rvert}$
1	$y = -5.5238x + 295.36$	5.52
2	$y = -5.4405x + 295.11$	5.44
3	$y = -5.6667x + 296.25$	5.67
4	$y = -5.6667x + 296.25$	5.67
Average		**5.57**

Considering an average value of the curves absolute slope ($|a|$), a constant calibration factor of $\frac{1\ l}{5.6\ mm}$ is chosen.

Appendix B

Slide velocity signal processing

Slide velocity raw signals are found processing slide instantaneous position signals; these diagrams show very high oscillations in values. For this reason, each of them has been subjected to a power spectral density analysis, performed in Matlab. All the obtained spectra reveal the presence of a big peak related to a 50 Hz frequency; this is obviously due to electrical interferences. The application of a low-pass filter is essential for cleaning slide velocity signals before performing data analysis. A filter has been designed using the Matlab function *'fdesign.lowpass'*, considering a passband frequency of 43 Hz and a stopband frequency equal to 48 Hz. These two frequencies have been chosen after a sensitivity analysis of parameters considered in the Matlab function. Therefore, these two frequency values define the best attenuation band whereas wave periods related to frequencies higher than 48 Hz are completely delated. After filtering application, great oscillations of raw signals are smoothed and the 50 Hz frequency peak is no longer visible in the spectra.

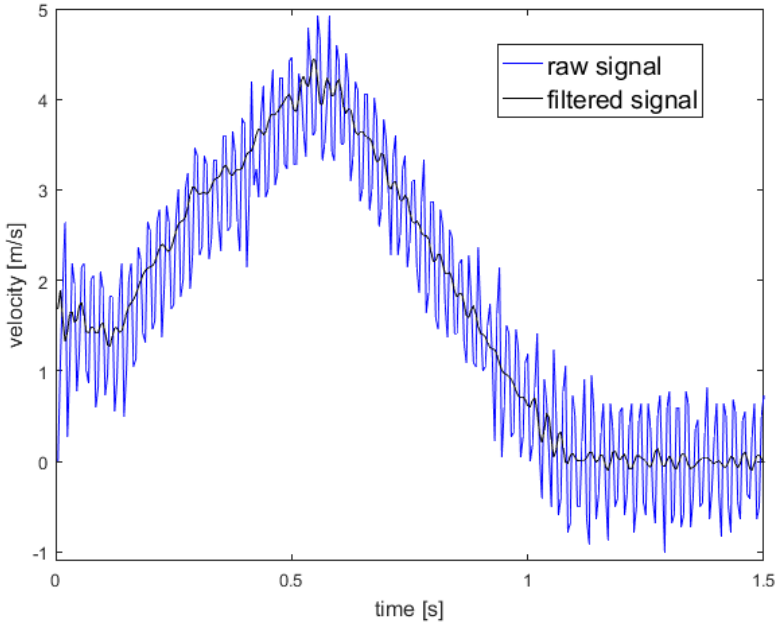

Figure B.1: overlapping of raw and filtered slide velocity signals, considering trial 2h.I_B.

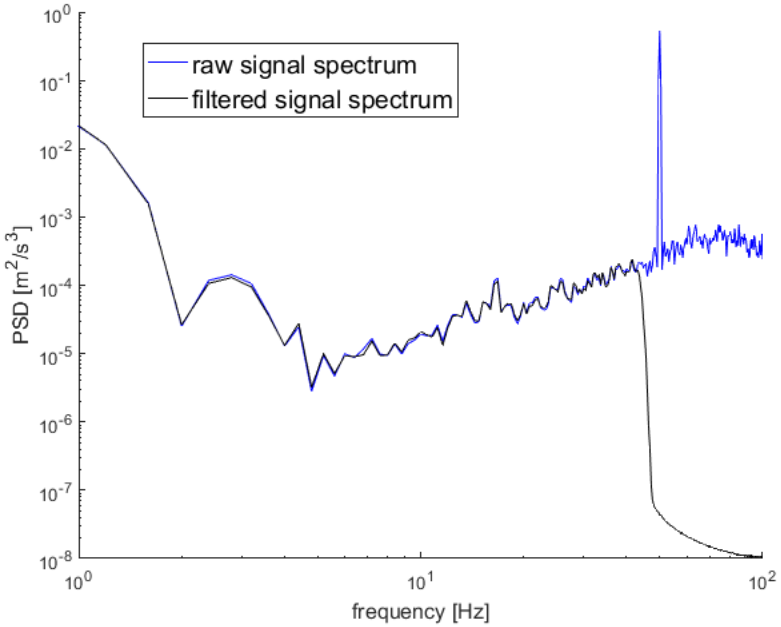

Figure B.2: overlapping of raw and filtered slide velocity spectra, considering trial 2h.I$_B$.

To extrapolate an accurate velocity curve peak value, the shape of curve part related to higher velocity is isolated and simulated using a third or fourth order polynomial function. Slide impact velocity values are evaluated applying the polynomial function which better reproduces the velocity curve tendency in the peak zone. The uncertainty which may affect this method is evaluated in Chapter 5.

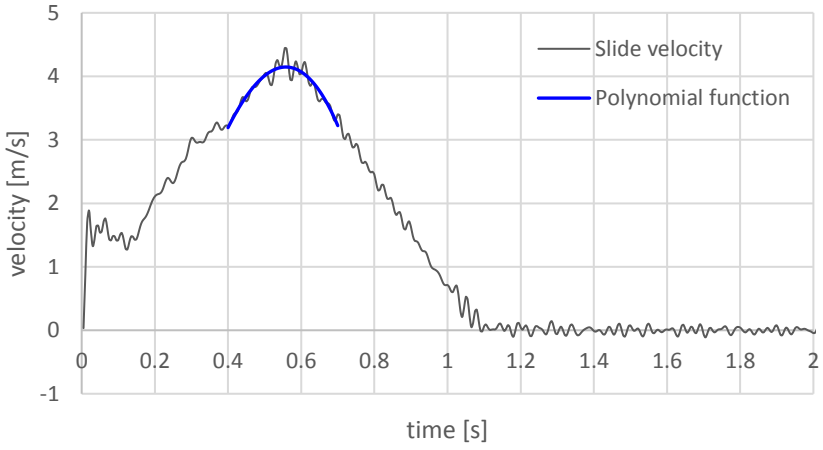

Figure B.3: example of polynomial function application ($v = -25.282t^3 + 0.1033t^2 + 23.504t - 4.6083$) on filtered slide velocity signal of trial 2h.I$_B$.

Appendix C

Video screenshots regarding wave propagation consistencies in trials with different slide arrangements

To demonstrate that all slide arrangements have the same effects on wave propagation in the basin, some video screenshots obtained by implementing the Matlab code are shown below. They are related to all slide blocks arrangements of both Model A and Model B, considering the first and the second starting position on the ramp respectively. The instants considered are the same discussed in chapter 6, since they correspond to main waves characterizing the wave propagation phenomenon.

Model A

4.I_A

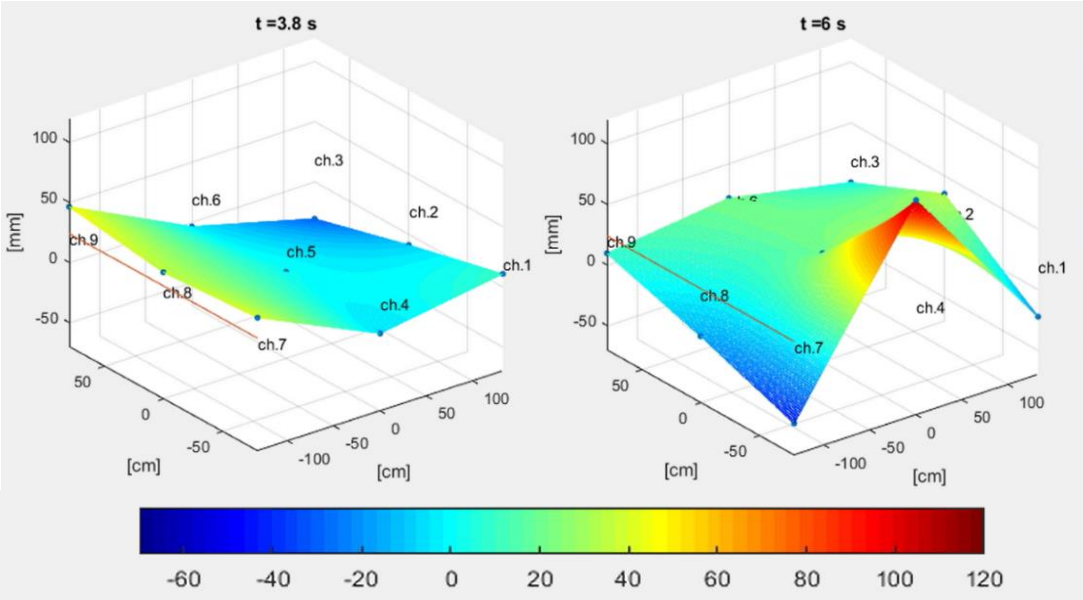

Figure C.1: main wave propagation video screenshots for trial 4.I_A at time 3.8 and 6 seconds illustrating the incident wave propagation in the basin on the left and the main reflected wave on the right.

$2h.I_A$

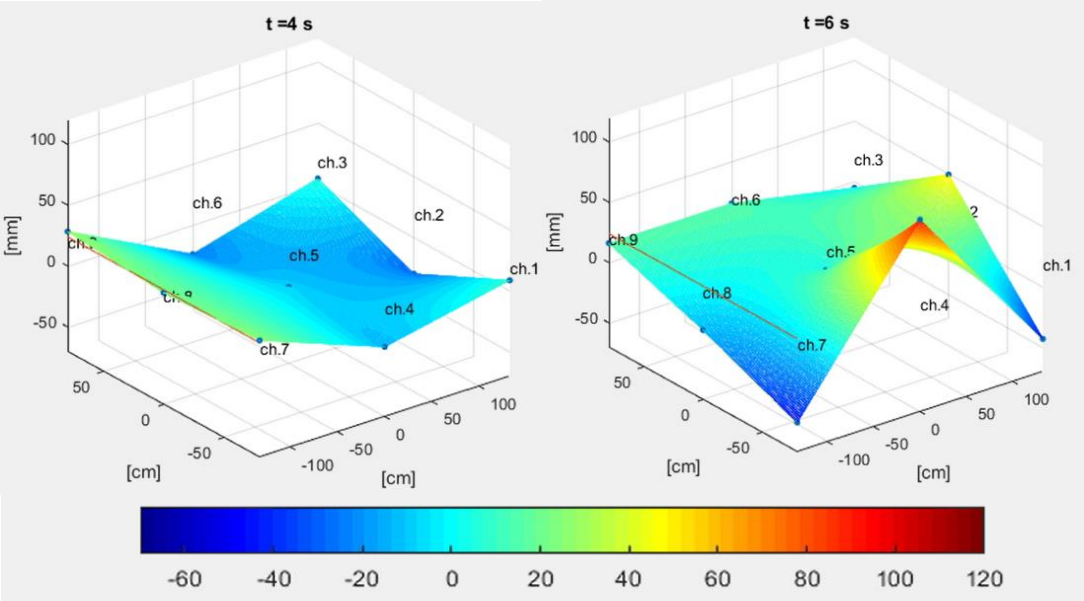

Figure C.2: main wave propagation video screenshots for trial 2h.I_A at time 4 and 6 seconds illustrating the incident wave propagation in the basin on the left and the main reflected wave on the right.

$2v.I_A$

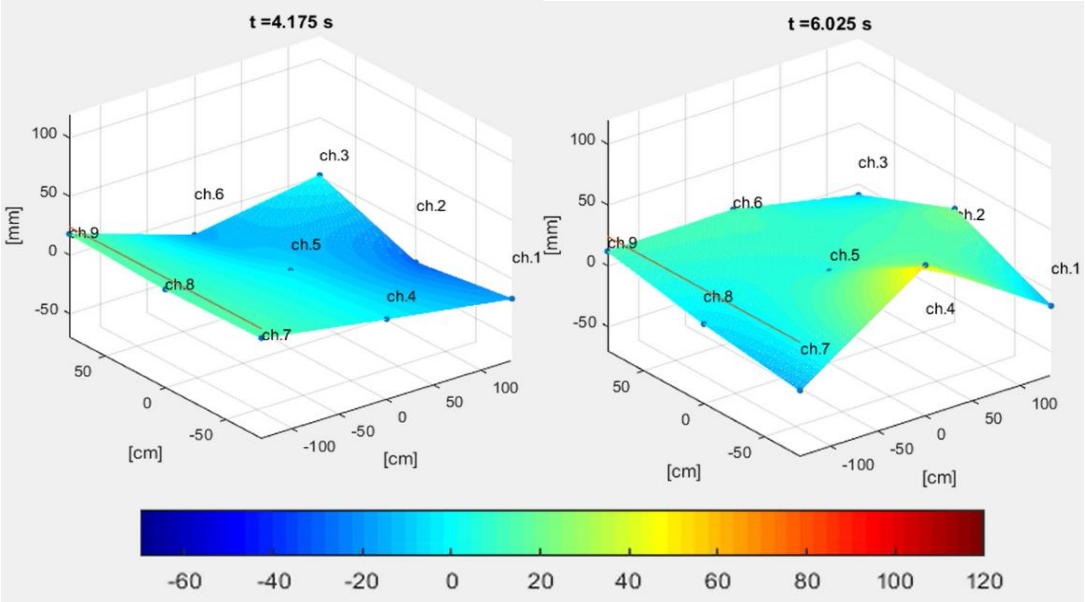

Figure C.3: main wave propagation video screenshots for trial 2v.I_A at time 4.175 and 6.025 seconds illustrating the incident wave propagation in the basin on the left and the main reflected wave on the right.

Model B

$4.II_B$

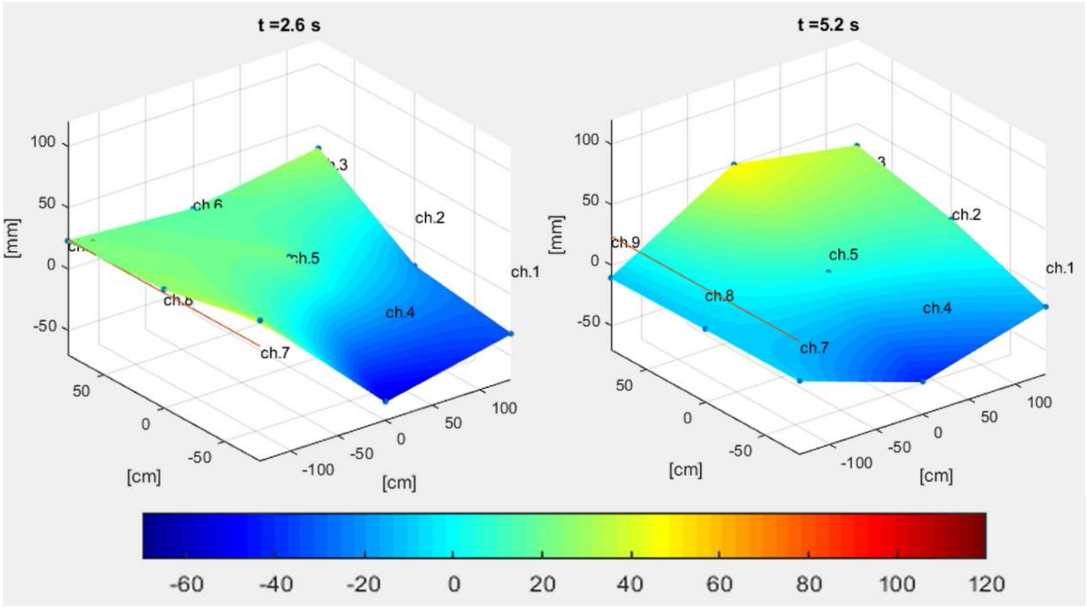

Figure C.4: main wave propagation video screenshots for trial $4.II_B$ at time 2.6 and 5.2 seconds illustrating incident wave propagation in the basin on the left and main reflected wave on the right.

$2h.II_B$

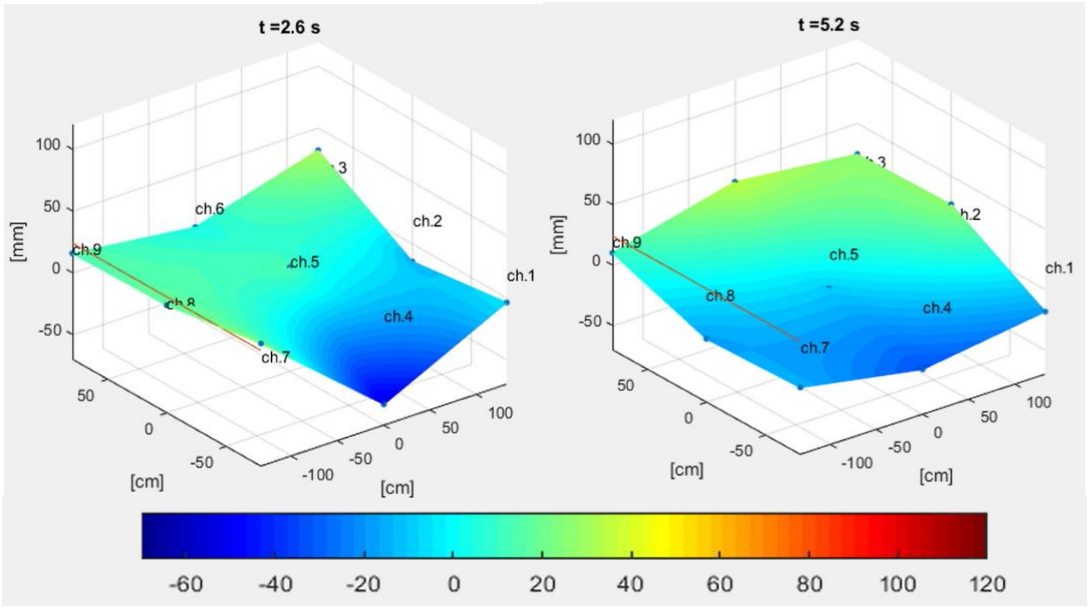

Figure C.5: main wave propagation video screenshots for trial $2h.II_B$ at time 2.6 and 5.2 seconds illustrating incident wave propagation in the basin on the left and main reflected wave on the right.

1.II_B

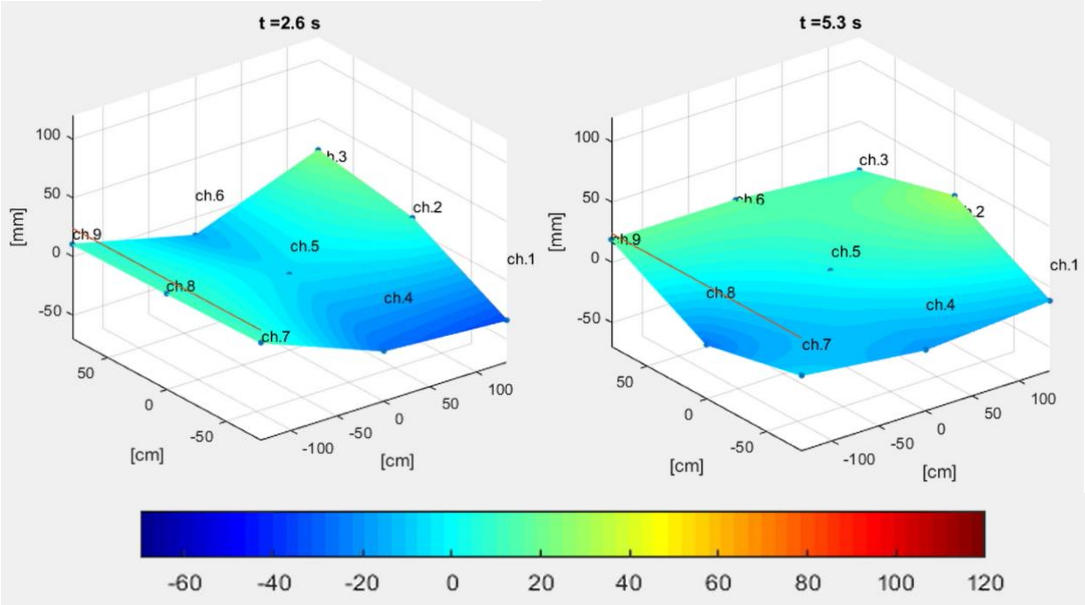

Figure C.6: main wave propagation video screenshots for trial 1.II_B at time 2.6 and 5.3 seconds illustrating incident wave propagation in the basin on the left and main reflected wave on the right.

2v.II_B

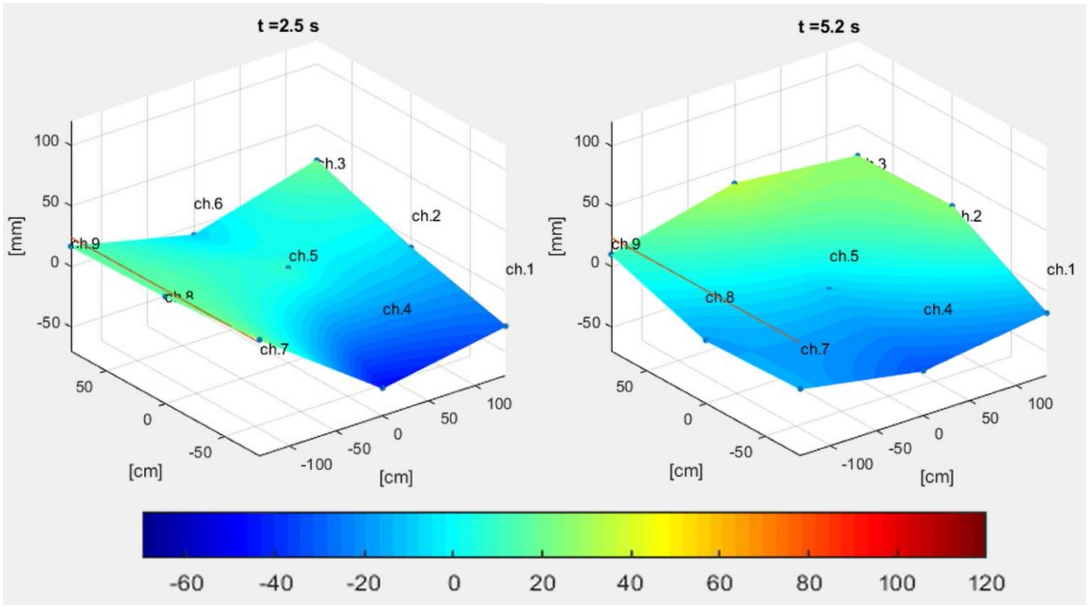

Figure C.7: main wave propagation video screenshots for trial 2v.II_B at time 2.5 and 5.2 seconds illustrating incident wave propagation in the basin on the left and main reflected wave on the right.

3.IV_B

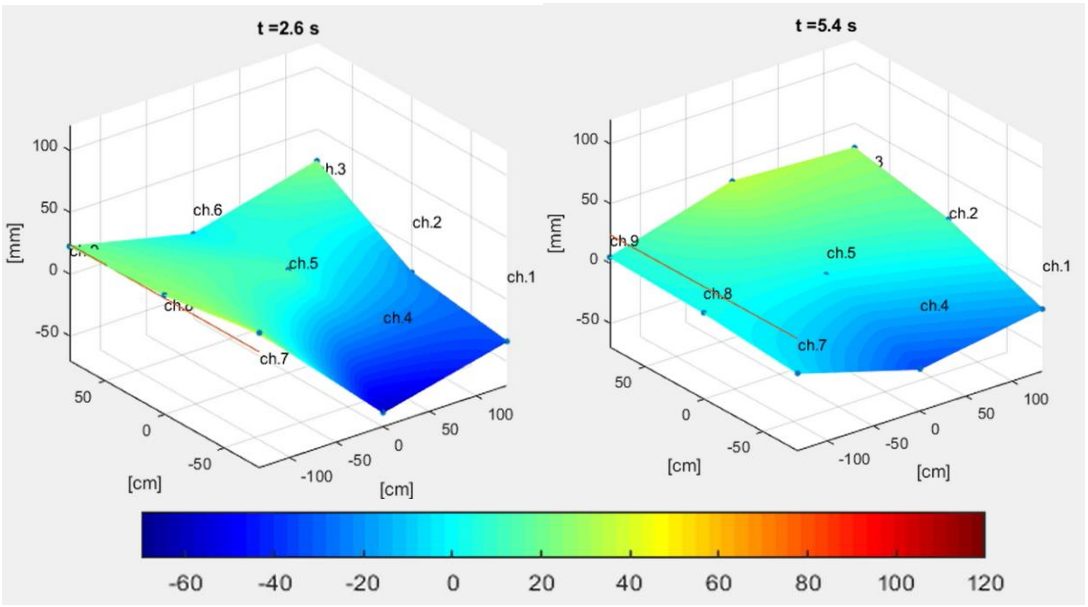

Figure C.8: main wave propagation video screenshots for trial 3.IV_B at time 2.6 and 5.4 seconds illustrating incident wave propagation in the basin on the left and main reflected wave on the right.

6.IV_B

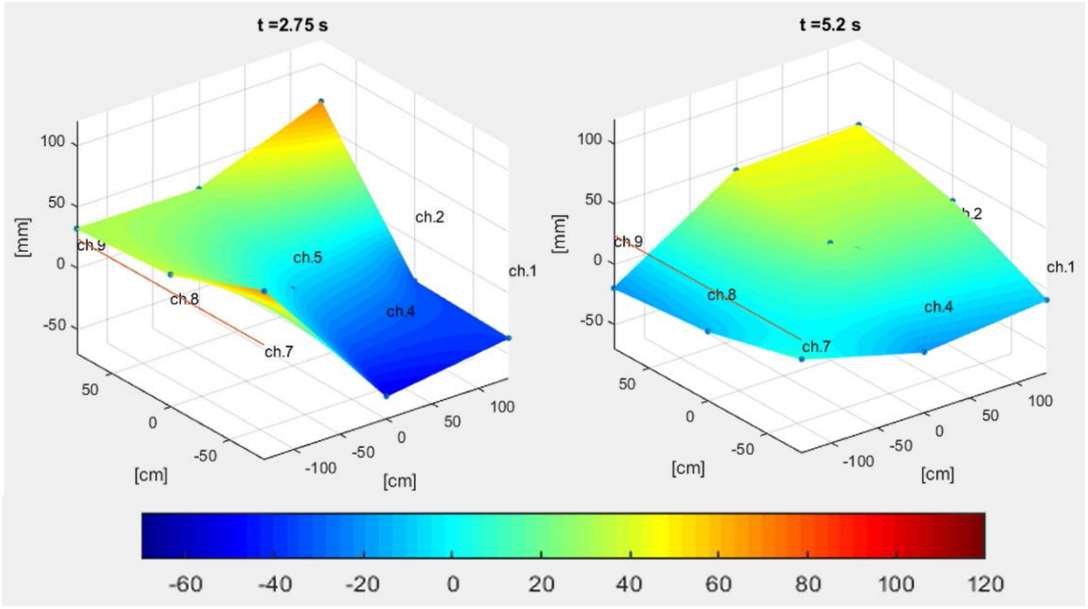

Figure C.9: main wave propagation video screenshots for trial 6.IV_B at time 2.75 and 5.2 seconds illustrating incident wave propagation in the basin on the left and main reflected wave on the right.

Appendix D

Influence of slide shape on dam overtopping modality in all the trials performed

The distribution of overtopping water volumes along the dam width is almost the same for all trials performed. In fact, considering constant slide volumes in different starting positions on the ramp, the percentages that describe the amount of water collected in each bucket do not change much. The diagrams below are reported as a confirmation of this statement; they illustrate the percentages of the total overtopped volume that cross one of the four segments on the dam top before being rerouted in pipes and then in the corresponding bucket. All trials carried out with a freeboard of 2.4 cm and 3.2 cm are considered.

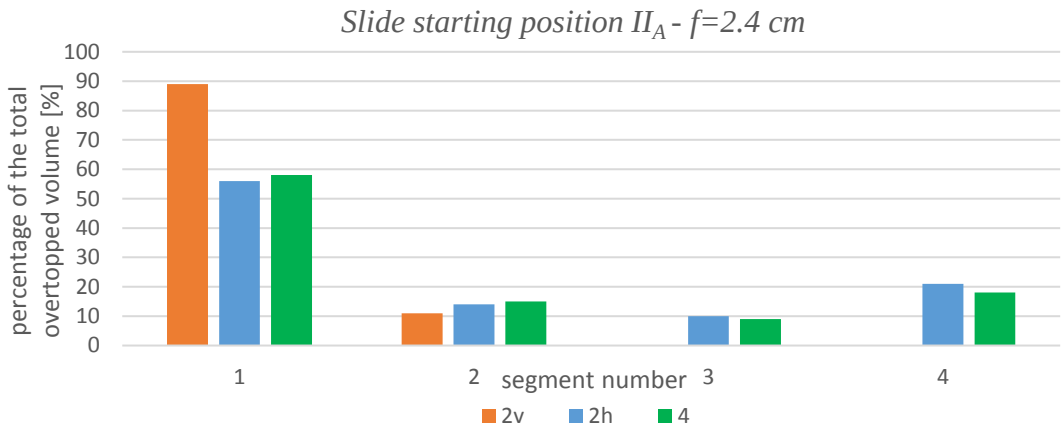

Figure D.1: the diagram illustrates the percentages of the total overtopped volume measured in different buckets. Each of them is connected to one of the four specific segments of the channel where overtopped water from the dam is funnelled; trials considered are 2v.II_A, 2h.II_A and 4.II_A.

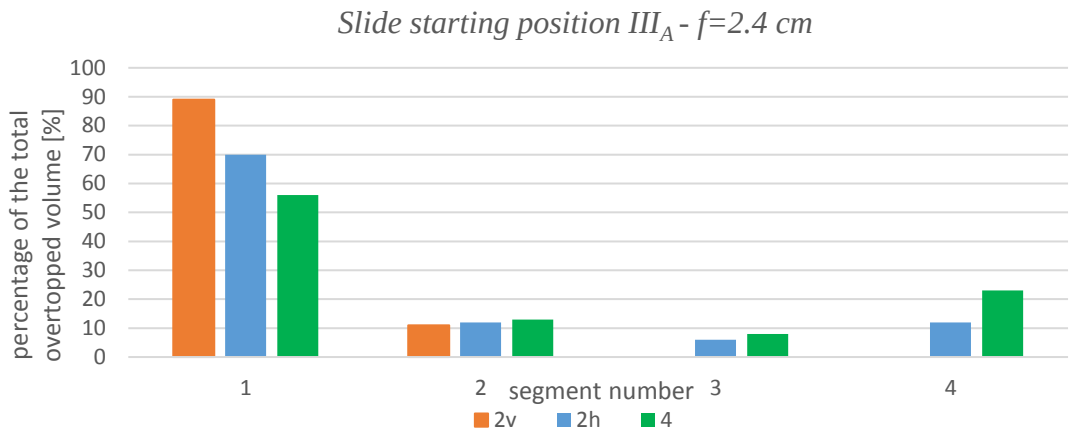

Figure D.2: the diagram illustrates the percentages of the total overtopped volume measured in different buckets. Each of them is connected to one of the four specific segments of the channel where overtopped water from the dam is funnelled; trials considered are 2v.III_A, 2h.III_A and 4.III_A.

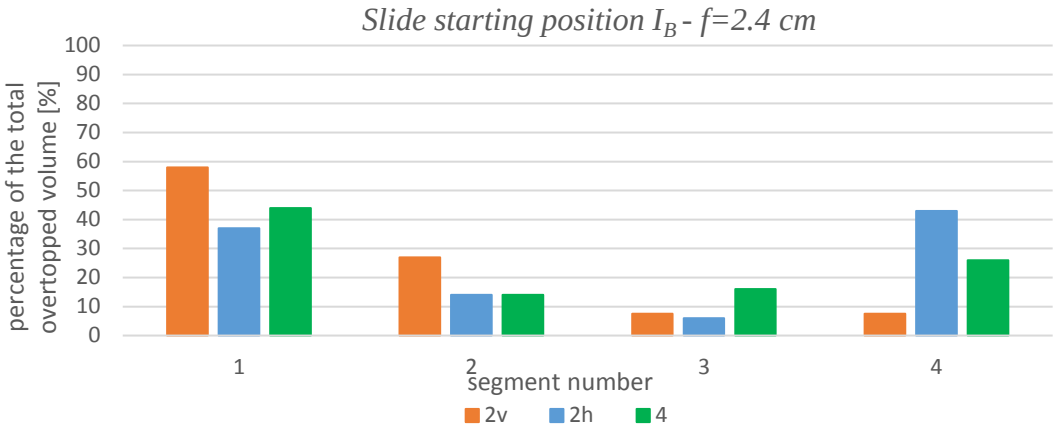

Figure D.3: the diagram illustrates the percentages of the total overtopped volume measured in different buckets. Each of them is connected to one of the four specific segments of the channel where overtopped water from the dam is funnelled; trials considered are 2v.I_B, 2h.I_B and 4.I_B.

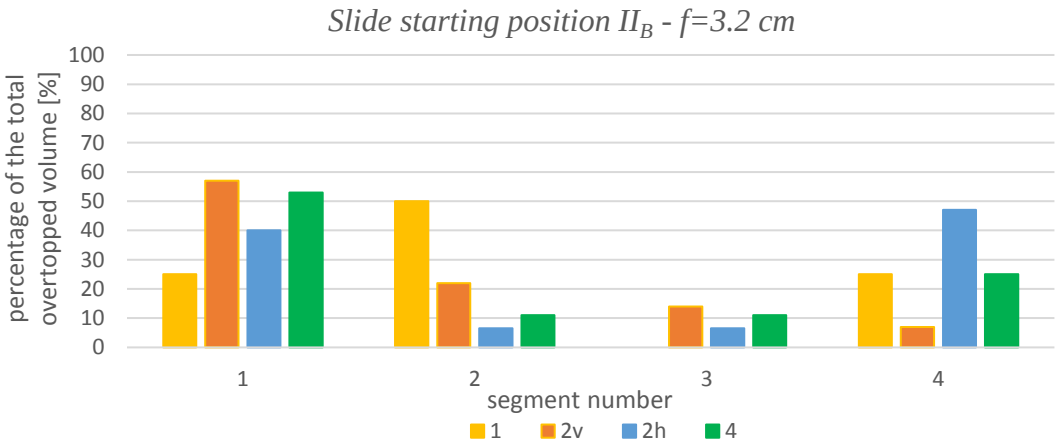

Figure D.4: the diagram illustrates the percentages of the total overtopped volume measured in different buckets. Each of them is connected to one of the four specific segments of the channel where overtopped water from the dam is funnelled; trials considered are 1.II_{B_6}, 2v.II_{B_6}, 2h.II_{B_6} and 4.II_{B_6}.

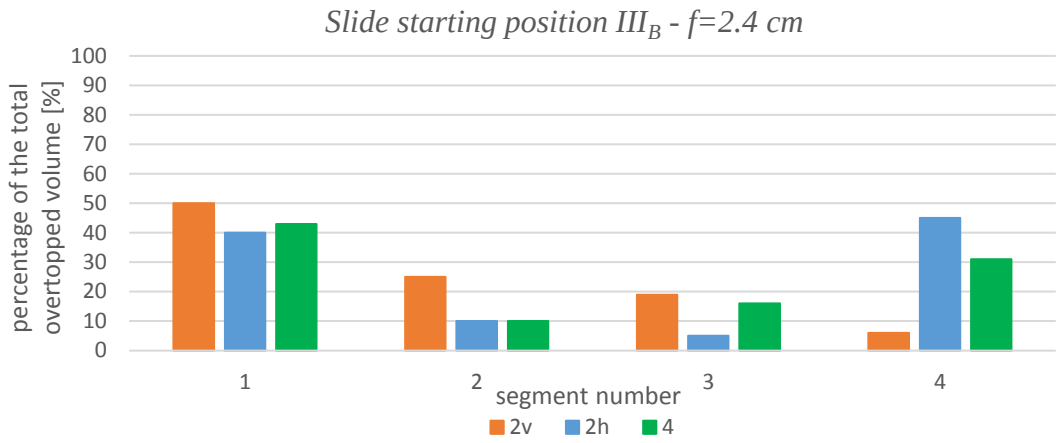

Figure D.5: the diagram illustrates the percentages of the total overtopped volume measured in different buckets. Each of them is connected to one of the four specific segments of the channel where overtopped water from the dam is funnelled; trials considered are 1.III_B, 2v.III_B, 2h.III_B and 4.III_B.

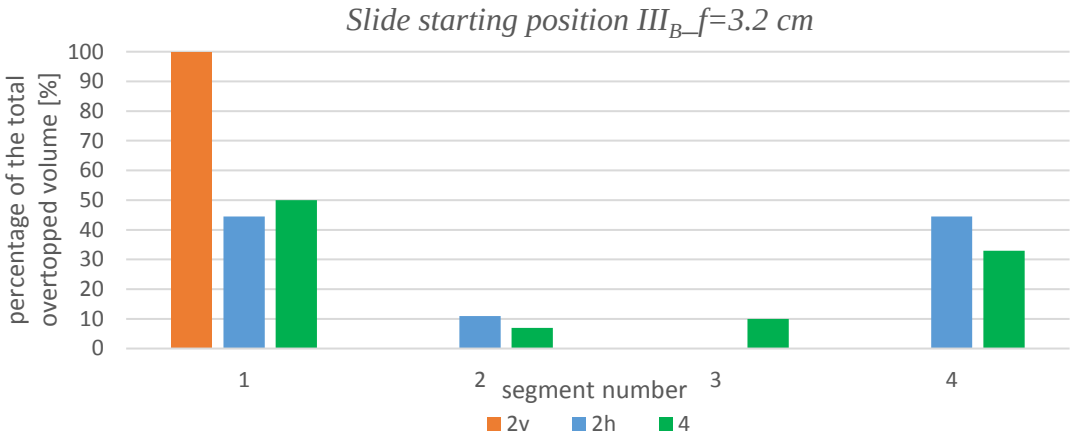

Figure D.6: the diagram illustrates the percentages of the total overtopped volume measured in different buckets. Each of them is connected to one of the four specific segments of the channel where overtopped water from the dam is funnelled; trials considered are 1.III_{B_6}, 2v.III_{B_6}, 2h.III_{B_6} and 4.III_{B_6}.

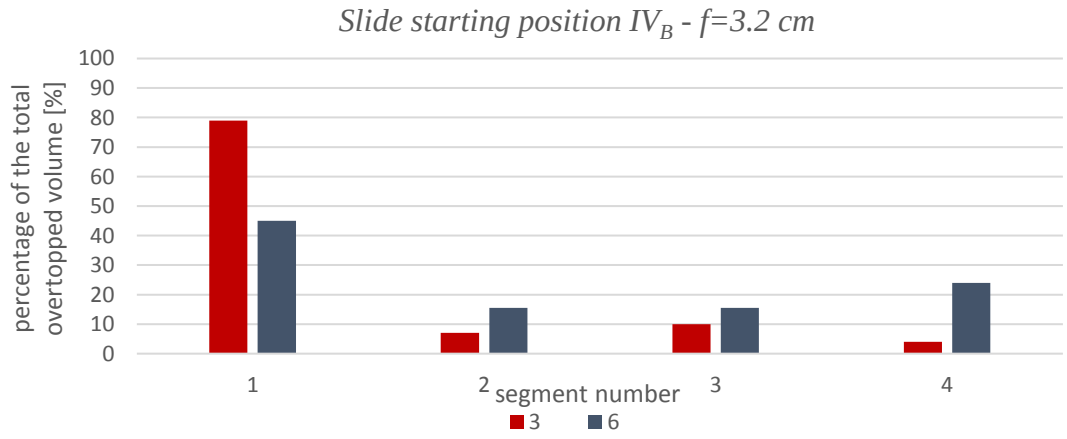

Figure D.7: the diagram illustrates the percentages of the total overtopped volume measured in different buckets. Each of them is connected to one of the four specific segments of the channel where overtopped water from the dam is funnelled; trials considered are 3.IV_{B_6} and 6.IV_{B_6}.

Appendix E

Diagrams P-W_w/h^3 and P^*-W_w/W_s on the semi-logarithmic scale

Here below are the two diagrams P - W_w/h^3 and P^* - W_w/W_s on the semi-logarithmic scale. They clearly show that the values scattering is around one order of magnitude in both cases.

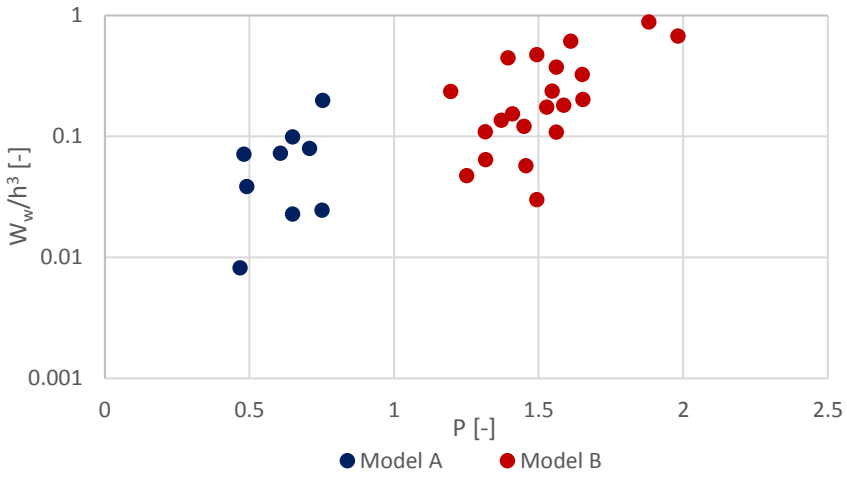

Figure E.1: the diagram illustrates the relation between the impulse product parameter P and the dimensionless ratio W_w/h^3 on a semi-logarithmic scale; the set of three reference independent quantities used is h, V_s and ρ_w.

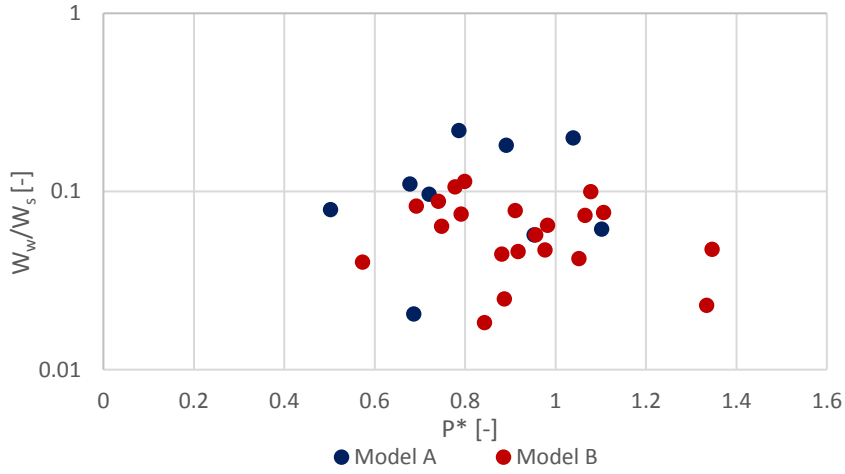

Figure E.2: the diagram illustrates the relation between the dimensionless parameter P^* and the dimensionless ratio W_w/W_s on a semi-logarithmic scale; the set of three reference independent quantities used is W_s, V_s and ρ_w.

Appendix F

Results of the dimensional analysis which considers a set of three reference independent quantities composed by h, V_s and ρ_w

Considering h, V_s and ρ_w as primary quantities (the same chosen by Heller and Hager for the evaluation of P), the dimensionless main output W_w (overtopping water volume) of the model can be defined as:

$$\frac{W_w}{h^3} = f\left(1, \frac{f}{h}, \frac{W_s}{h^3}, \frac{b_s}{h}, \frac{l_s}{h}, 1, 1, \frac{gh}{{V_s}^2}\right) \qquad \textit{Equation F.1}$$

Figures F.1, F.2 and F.3 show the relation between the dimensionless parameter $\frac{W_s}{h^3}$ and the dimensionless output $\frac{W_w}{h^3}$, according to the variation of slide width, slide length and dam freeboard respectively. The trends that can be observed in the three diagrams below confirm that the slide volume is the predominant governing parameter of the phenomenon. For this reason, effects due to other governing parameters are not discernible.

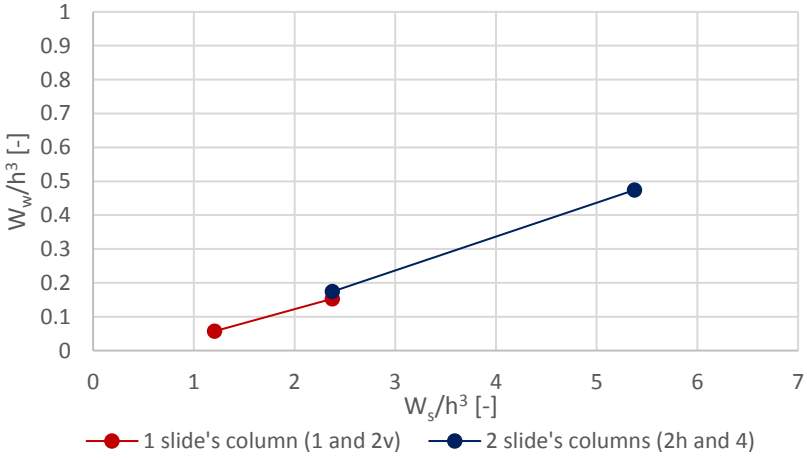

Figure F.1: the diagram illustrates the influence of the dimensionless parameter W_s/h^3 on the dimensionless output W_w/h^3 depending on slide width ("1 slide's column" is associated to 1 and 2v blocks arrangements; "2 slide's columns" is associated to 2h and 4 blocks arrangements). Trials considered are conducted on Model B with the same dam freeboard (f=2.4 cm) and slide at second starting positions on the ramp (II_B).

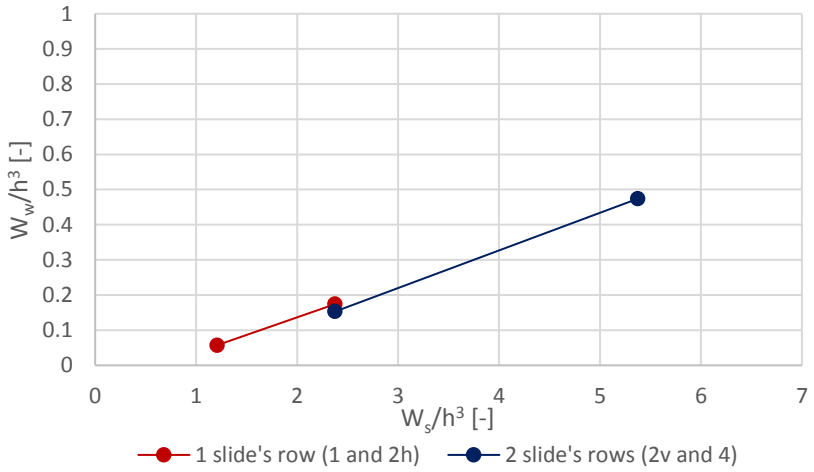

Figure F.2: the diagram illustrates the influence of the dimensionless parameter W_s/h^3 on the dimensionless output W_w/h^3 depending on slide length ("1 slide's row" is associated to 1 and 2h blocks arrangements; "2 slide's rows" is associated to 2v and 4 blocks arrangements). Trials considered are conducted on Model B with the same dam freeboard (f=2.4 cm) and slide at second starting positions on the ramp (II_B).

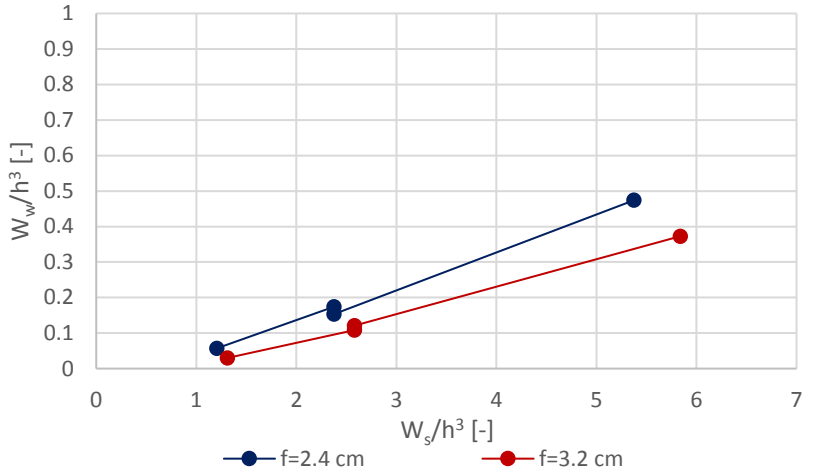

Figure F.3: the diagrams illustrates the influence of the dimensionless parameter W_s/h^3 on the dimensionless output W_w/h^3 depending on the dam freeboard (f=2.4 cm and f=3.2 cm). Trials considered are conducted on Model B with slide at second starting position on the ramp (II_B) and different slide volumes (1,2h,2v,4,3,6 blocks arrangements).

Figures F.4, F.5 show the relation between the dimensionless parameter $\frac{V_s^2}{gh}$ and the dimensionless output $\frac{W_w}{h^3}$, according to the variation of slide width and slide length, considering Model B and Model A respectively. The strong influence of slide volume is evident: in cases with distinct slide volumes, even if the values of dimensionless slide impact velocity are similar, the normalised output differs substantially.

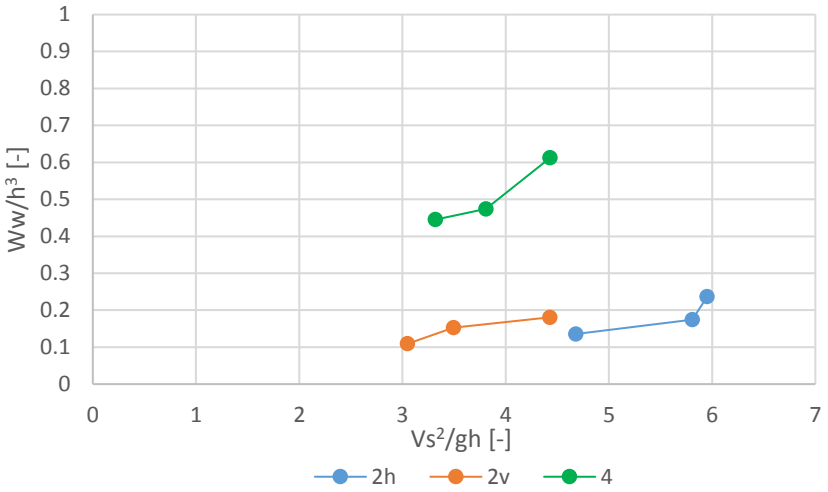

Figure F.4: the diagram illustrates the influence of the dimensionless parameter $V_s^2/(gh)$ on the dimensionless output W_w/h^3 depending on slide width (2v and 4) and on slide length (2h and 4). Trials considered are conducted on Model B with the same dam freeboard (f=2.4 cm) and different slide starting positions on the ramp (I_B, II_B and III_B).

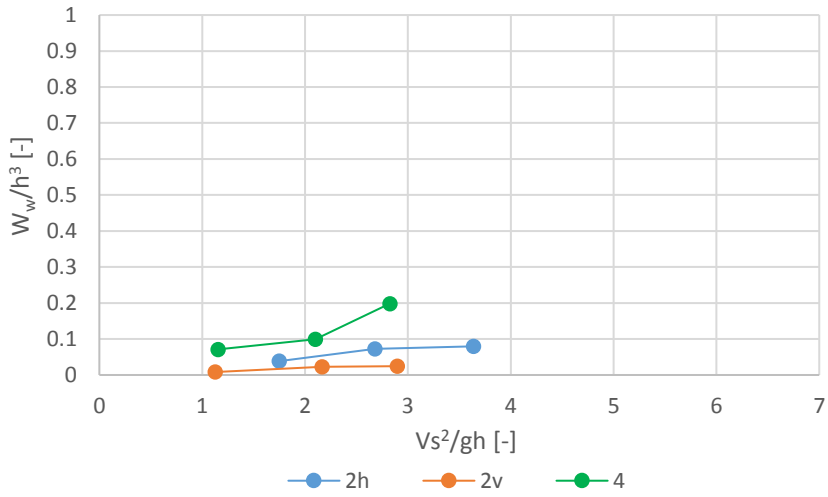

Figure F.5: the diagram illustrates the influence of the dimensionless parameter $V_s^2/(gh)$ on the dimensionless output W_w/h^3 depending on slide width (2v and 4) and on slide length (2h and 4). Trials considered are conducted on Model A with the same dam freeboard (f=2.4 cm) and different slide starting positions on the ramp (I_A, II_A and III_A).

Figure F.6 shows the relation between the dimensionless parameter $\frac{V_s^2}{gh}$ and the dimensionless output $\frac{W_w}{h^3}$, according to the dam freeboard variation in Model B. It is noted that the dam freeboard influences the output but the points disposition depends mainly on the slide volume: values related to trials with a higher slide volume are in the upper part of the graph.

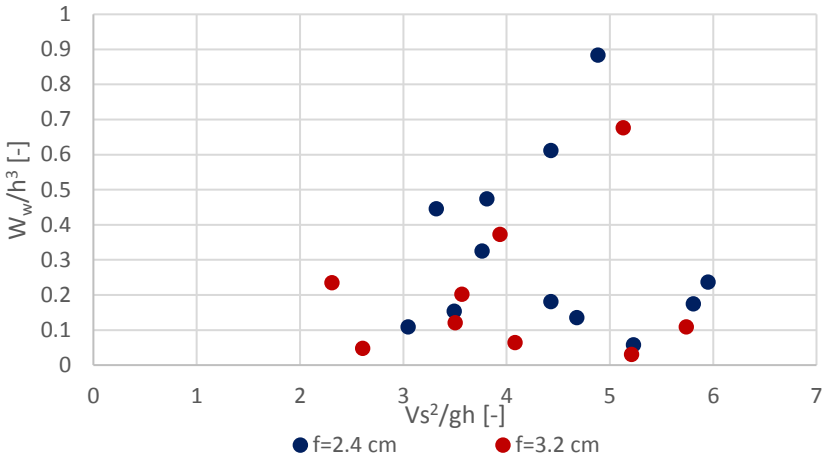

Figure F.6: the diagram illustrates the influence of the dimensionless parameter $V_s^2/(gh)$ on the dimensionless output W_w/h^3 depending on dam freeboard (f=2.4 cm and f=3.2 cm). Trials considered are conducted on Model B with different slide volumes (1,2h,2v,4,3,6 blocks arrangements) at different starting positions on the ramp (I_B, II_B III_B and IV_B).

References

[1] Akgün, A., **(**2011) "Assessment of possible damaged areas due to landslide induced waves at a constructed reservoir using empirical approaches: Kurtun (North Turkey) Dam reservoir area", Karadeniz Technical University, Geological Engineering Department, Trabzon, Turkey

[2] Ataie-Ashtiani, B., Malek Mohammadi, S., (2007) "Near field amplitude of subaerial landslide generated waves in dam reservoirs", *Dam Engineering*, 18(4): 190-222

[3] Ataie-Ashtiani, B., Nik-Khah A., (2008) "Impulsive waves caused by subaerial landslides*",* Springer Science+Business Media B.V.

[4] Bolzoni, B., (2015) "Physical model study on impacts of landslide generated wave action on embankment dams", Master Thesis, Hydropower and Hydraulic Engineering, Norwegian University of Science and Technology (NTNU), Trondheim

[5] Braathen, A., Blikra, L. H., Berg S.S., Karlsen, F., (2004) "Rock-slope failures in Norway; type, geometry, deformation mechanisms and stability", *Norwegian Journal of Geology,* Trondheim, 84: 67-88

[6] Cruden, D. M., Varnes, D. J., (1996) "Landslide Types and Processes", Special Report, Transportation Research Board, National Academy of Sciences, 247: 36-75

[7] De las Llanderas Ramírez, M. J, (2016) "Studies on impacts of landslide generated wave action on embankment dams", bachelor project work, Hydropower and Hydraulic Engineering, Specialization Project, Norwegian University of Science and Technology (NTNU), Trondheim

[8] Di Risio, M., Sammarco, P., (2008) "Analytical Modeling of Landslide-Generated Waves", *Journal of waterway, port, coastal, and ocean engineering*, 134(1): 53-60

[9] Falappi, S., Gallati, M., (2007) "SPH simulation of water waves generated by granular landslides", Proc. 32nd Congress of IAHR Venice, 933: 1-10

[10] Fernandes de Carvalho, R., Antunes do Carmo, J. S., (2007) "Landslides into reservoirs and their impacts on banks", Springer Science+Business Media B.V.

[11] Fritz, H. M., Liu, P. C., (2001) "An application of wavelet transform analysis to landslide-generated impulse waves", *Ocean wave measurement and analysis*, 1477-1486

[12] Fritz, H. M., Hager, W. H., Minor, H., (2001) "Lituya Bay case: Rockslide impact and wave run-up", *Science of Tsunami Hazards*, 19(1)

[13] Fritz, H. M., Hager W. H., Minor, H. E., (2004) "Near Field Characteristics of Landslide Generated Impulse Waves", *Journal of waterway, port, coastal, and ocean engineering*, 130(6): 287-302

[14] Fritz, H. M., Mohammed, F., Yoo, J, (2009) "Lituya Bay Landslide Impact Generated Mega-Tsunami 50th Anniversary", School of Civil and Environmental Engineering, Georgia Institute of Technology, 210 Technology Circle, Savannah, U.S.A.

[15] G. Sigtryggsdottir, F., Snæbjornsson, J. T., Grande, L., Sigbjornsson, R., (2015) "Methodology for geohazard assessment for hydropower projects", Springer Science+Business Media Dordrecht, *Natural Hazards,* 79: 1299–1331

[16] G. Sigtryggsdóttir, F., Snæbjörnsson, J. T., Grande. L., Sigbjörnsson R., (2016) "Interrelations in multi-source geohazard monitoring for safety management of infrastructure systems", *Structure and Infrastructure Engineering*, 12 (3): 327–355

[17] Gisler, G., Weaver, R., Mader, C., (2003) "Two-and three-dimensional simulations of asteroid ocean impacts", Los Alamos National Laboratory, Los Alamos, NM, USA, *Science of Tsunami Hazards*, 21(2): 119
[18] Gisler, G., (2008) "Tsunami Simulations", Physics of Geological Processes, University of Oslo, 0316 Oslo, Norway, *The Annual Review of Fluid Mechanics* 40: 71–90
[19] Gómez Núñez, J., Berezowsky, V. M., (2007) "Estimation of the water waves generated by the landslide in the Grijalva river, Mexico" Universidad Nacional Autónoma de México Instituto de Ingeniería - Ciudad Universitaria, D.F, México, *Italian Journal of Engineering Geology and Environment - Book Series (6)*
[20] Hanson, G., Temple, D., (2007) "The National Dam Safety Program", Final Report on Coordination and Cooperation with the European Union on Embankment Failure Analysis FEMA 602, USDA-ARS-HERU
[21] Harbitz, C. B., Glimsdal, S., Løvholt, F., Kveldsvik, V., Pedersena, G. K., Jensen, A., (2014) "Rockslide tsunamis in complex fjords: From an unstable rock slope at Åkerneset to tsunami risk in western Norway", *Coastal Engineering*, 88: 101–122
[22] Heller, V., (2007) "Landslide generated impulse waves: Prediction of near field characteristics", Dissertation ETH N°. 17531, Swiss Federal Institute of Technology Zurich (ETH), Zurich
[23] Heller, V., Hager, W. H., Minor, H.-E., (2009) "Landslide generated impulse waves in reservoirs: Basic and computation", Mitteilungen 211, Swiss Federal Institute of Technology Zurich (ETH), Zurich
[24] Heller, V., Hager, W. H., (2010) "Impulse Product Parameter in Landslide Generated Impulse Waves", *Journal of waterway, port, coastal, and ocean engineering*, 136(3): 145-155
[25] Heller, V., (2011) "Scale effects in physical hydraulic engineering models", *Journal of Hydraulic Research*, 49(3): 293–306
[26] Huang, M.-C., (2004) "Wave parameters and functions in wavelet analysis with filtering", *Ocean Engineering*, 31: 111–125; 813–831
[27] Huber, A., (1980) "Schwallwellen in Seen als Folge von Felsstürzen", VAW-Mitteilung 180, Vischer, D., Swiss Federal Institute of Technology Zurich (ETH), Zurich
[28] International Commission on Large Dams (ICOLD – CIGB), (1987) "Dam safety - Guidelines; Sécurité des barrages - Recommandations", Bulletin 59, Paris
[29] International Commission on Large Dams (ICOLD – CIGB), (1995) "Dam failures - statistical analysis; Raptures de barrages - analyse statistique", Bulletin 99, Paris
[30] International Commission on Large Dams (ICOLD - CIGB), (2011) "Constitution - Statuts", Paris
[31] International Commission on Large Dams - European Club (ICOLD), (2012) "Safety of existing dams", Working Group Report
[32] International Commission on Large Dams (ICOLD - CIGB), (2013) "Dam Safety Management: Operational Phase of the Dam Life Cycle", Bulletin 154, Paris
[33] International Commission on Large Dams - European Club (ICOLD), (2014) "Dam legislation", Dam Legislation Report
[34] Kamphuis, J. W., Bowering, R. J., (1970) "Impulse waves generated by landslides", *Coastal Engineering*, 35: 575-588
[35] Lee, H.S., Kwon, S.H., (2003) "Wave profile measurement bywavelet transform", *Ocean Engineering*, 30: 2313–2328
[36] Lindstrøm, E. K., Pedersen, G. K., Jensen, A., Glimsdal, S., (2014) "Experiments on slide generated waves in a 1:500 scale fjord model", *Coastal Engineering*, 92: 12–23
[37] Lynett, P., Liu, P. L.-F., (2005) "A numerical study of the run-up generated by three-dimensional landslides", *Journal of geophysical research*, 110

[38] Lorås, S., (2014) "Landslides in reservoirs and their impact on rockfill dams", Master project work, Hydropower and Hydraulic Engineering, Norwegian University of Science and Technology (NTNU), Trondheim
[39] Massel, S. R., (2001) "Wavelet analysis for processing of ocean surface wave records", *Ocean Engineering*, 28: 957–987
[40] Masson, D. G., Harbitz, C. B., Pedersen, G., Løvholt, F., (2006) "Submarine landslides: processes, triggers and hazard prediction", Philosophical transcription of the royal society
[41] Mortensen, R., (2016) "Landslide generated waves in reservoirs embankment dam overtopping", Master Thesis, Hydropower and Hydraulic Engineering, Norwegian University of Science and Technology (NTNU), Trondheim
[42] Najafi-Jilani, A., Ataie-Ashtiani, B., (2012) "Laboratory investigation of wave run-up caused by landslides in dam reservoirs", *Quarterly Journal of Engineering Geology and Hydrogeology*, 45: 89 –98
[43] Novak, P.,Moffat, A.I.B.,Nalluri, C., Narayanan, R., (2007) "Hydraulic Structures", IV edition, Taylor & Francis
[44] Panizzo, A., Bellotti, G., De Girolamo, P., (2002) "Application of wavelet transform analysis to landslide generated waves", *Coastal Engineering* 44, 321– 338
[45] Panizzo, A., De Girolamo, P., (2005) "Forecasting impulse waves generated by subaerial landslides", *Journal of geophysical research*, 110
[46] Panizzo, A., De Girolamo, P., Di Risio, M., Maistri, A., Petaccia, A., (2005) "Great landslide events in Italian artificial reservoirs", *Natural Hazards and Earth System Sciences*, 5: 733–740
[47] Petley, D. N., (2010) "Landslide disaster mitigation in the Three Gorges Reservoir, China", *Mountain Research and Development*, 30(2):184-185
[48] Popescu, M.E. (1996). "From Landslide Causes to Landslide Remediation", Special Lecture, Proc. 7th Int. Symp. on Landslides, Trondheim, 1:75-96
[49] Sælevik, G., Jensen, A., Pedersen, G. K., (2009) "Experimental investigation of impact generated tsunami; related to a potential rock slide, Western Norway", *Coastal Engineering*, 56: 897–906
[50] Schmocker, L., Hager, W.H., (2009) "Dike breaching due to overtopping", 33rd International Association of Hydraulic Engineering & Research Congress (IAHR): Water Engineering for a Sustainable Environment, 3896-3903
[51] Semenza, E., Ghirotti, M., (2000) "History of the 1963 Vaiont slide: the importance of geological factors", Bulletin of *Engineering Geology* and the *Environment*, Springer-Verlag, 59: 87–97
[52] Slingerland, R. L., Voight, B., (1979) "Occurrences, properties and predictive models of landslide-generated impulse waves", *Developments in Geotechnical Engineering* 14B, Rockslides and Avalanches 2: 317-397
[53] Semenza, E., (2002) "La storia del Vajont raccontata dal geologo che ha scoperto la frana", Tecomproject, Ferrara
[54] Van Nieuwkoop, J.C.C., (2007) "Experimental and numerical modelling of tsunami waves generated by landslides", Msc Thesis, Delft University of Technology (TU Delft), Delft
[55] Viroulet, S., Cébron, D., Kimmoun, O., Kharif, C., (2013) "Shallow water waves generated by subaerial solid landslides", *Geophysical Journal International*, 193: 747–762
[56] Walder, J. S., Watts, P., Sorensen, O. E., Janssen, K., (2003) "Tsunamis generated by subaerial mass flows", *Journal of Geophysical Research*, 108(B5), 2236
[57] Zweifel, A., Hager, W. H., Mino, H.-E., (2006) "Plane Impulse Waves in Reservoirs", *Journal of waterway, port, coastal, and ocean engineering*, 132(5): 358-368

[58] Zweifel, A., (2004) “Impulswellen: Effekte der Rutschdichte und der Wassertiefe”, Dissertation 15596, Swiss Federal Institute of Technology Zurich (ETH), Zurich
[59] Zweifel, A., Zuccalà. D., Gatti, D., (2007) “Comparison between Computed and Experimentally Generated Impulse Waves”, *Journal of hydraulic engineering*, 133(2): 208-216